GEOLOGY OF THE SATURNIAN MOON, TITAN

"Constraining the surface composition and geological history of the main types of terrains found in the equatorial belt of Titan"

JEREMY BROSSIER

A thesis submitted in partial fulfilment of the requirements for
the degree of Doctor of Natural Sciences
(Dr. rer. nat.)

Department of Earth Sciences
Freie Universität Berlin
Berlin, Germany

2018

Supervisor: Prof. Dr. Ralf Jaumann
Freie Universität Berlin
Institute of Geological Sciences
Planetary Sciences and Remote Sensing
as well as
Deutsches Zentrum für Luft- und Raumfahrt aus Berlin (DLR)
Institute of Planetary Research
Planetary Geology group

2nd examiner: Prof. Dr. Anne Bernhardt
Freie Universität Berlin
Institute of Geological Sciences
Tectonics and Sedimentary Systems

Date of defense July 12th, 2018

Statutory Declaration

I hereby declare that the present work was developed and written completely by myself, and have not used sources or means without declaration in the text. Any thoughts from others or literal quotations are clearly marked. This thesis was not used in the same or in a similar version to achieve an academic grading elsewhere.

Jérémy Brossier

Berlin, on March 23, 2018

ABSTRACT

In thirteen years, infrared observations from the Visual and Infrared Mapping Spectrometer (VIMS) onboard the Cassini orbiter have provided significant hints about the spectral and geological diversity on Titan's surface, the largest moon of Saturn. The analysis of the infrared signature of spectral units enables constraining the surface composition, which is essential to understand the possible interactions between Titan's interior, surface and atmosphere and to constrain the hydrocarbon cycle existing on the moon. Here, a selection of areas are investigated in the equatorial regions of the moon, imaged by Cassini's remote sensing instruments, which exhibit an apparent transition from the VIMS IR-bright to the IR-blue and IR-brown units. These spectral units are named as such owing to their appearance in false-color composites at infrared wavelengths (red: 1.57/1.27 µm, green: 2.01/1.27 µm, and blue: 1.27/1.08 µm). By applying an updated radiative transfer model, the surface albedo was extracted for each of the infrared units identified in these regions. Surface albedo was then compared with synthetic spectra of binary mixtures of the two most expected components of Titan's surface, namely water ice and laboratory tholins. Water ice is supposed to primarily form Titan's substratum, while the tholins are analogous to the aerosols photochemically produced in the atmosphere. This compositional analysis allows to reconnect the derived surface composition and grain size information to the geomorphology retrieved from RADAR's SAR swaths. Hence, IR-bright units are interpreted as hills and plains coated by organic material and incised by fluvial networks. The erosion products are transported downstream to areas where IR-blue units are seen near the IR-bright units. These areas, enriched in water ice, are most likely outwash plains hosting icy and organic debris from fluvial erosion. Farther away from the IR-bright units, the IR-brown units are dominantly made of organics with varied grain sizes ranging from dust- to sand-sized particles that form the dunes fields. The transition areas therefore exhibit trends in terms of water ice content and grain size supported by geomorphological observations.

ACKNOWLEDGMENTS

First of all, I gratefully thank the work done by Cassini/VIMS team that made the spectral analysis possible. I also thank the Cassini/RADAR team for providing the RADAR SAR database used in my investigation. This project has been carried out at the DLR Institute of Planetary Research, and was also partly supported by the Institut Universitaire de France during my few stays in Paris.

Thus, I would like to thank my supervisor, Prof. Ralf Jaumann, who gave me the opportunity to accomplish this work, here in Berlin, and supported me for the participation in numerous international conferences and meetings. I am grateful to Katrin Stephan, my co-supervisor, who guided me for the processing of Cassini's data which was a quite harsh adventure at the beginning. Many thanks dedicated to Assoc. Prof. Sébastien Rodriguez, my "remote" supervisor, who helped me during all this period through a fruitful collaboration, joined by Thomas Cornet, Antoine Lucas and Luca Maltagliati, forming the Parisian crew. *Merci beaucoup!*

I would like to acknowledge Prof. Anne Bernhardt with a Vielen Danke, who kindly agreed to examine this dissertation.

Finally, last but not least, huge thanks to Solmaz for all the help you gave me during my stay in this jungle called DLR. Further gratitude goes for my co-officer, Mickael (aka Mika) with whom I shared the French office (building 103, room 320). May the force be with you during your quest for extraterrestrial life. Last thanks are reserved to all my DLR colleagues, notably Christian, Robert, Nasia, Maxime, Hugo, Gigio, Yaqui, ... and the coffee machine!

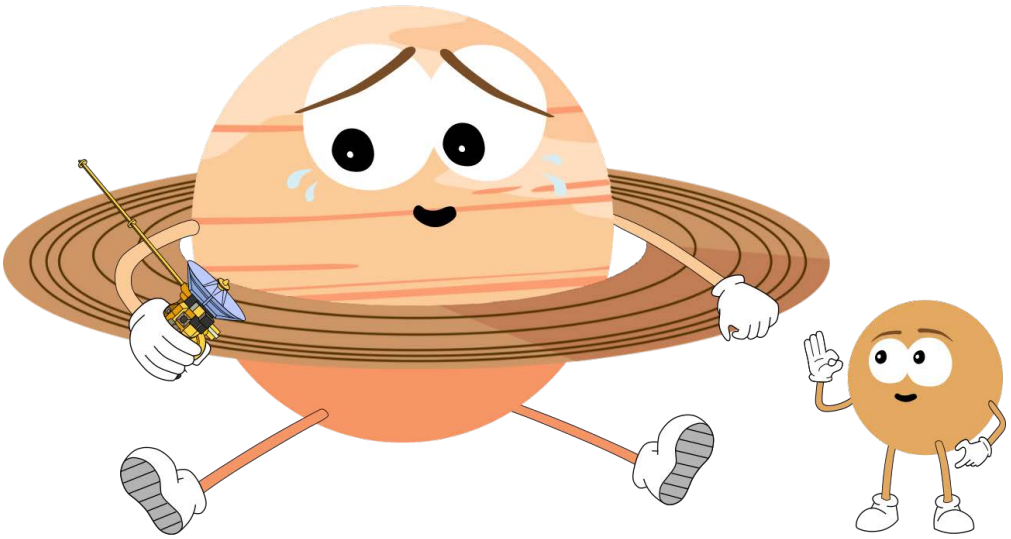

We'll miss you, Cassini

Contents

List of Figures

List of Tables

List of Abbreviations

BIDR	Basic Image Data Records
DISR	Descent Imager Spectral Radiometer
IAU	International Astronomical Union
IR	Infrared
ISIS3	Integrated Software for Imagers and Spectrometers vers. 3
ISS	Imaging Science Subsystem
JPL	Jet Propulsor Laboratory
LUT	Look-Up Table
MAD	Mean Absolute Difference
NASA	National Aeronautics and Space Administration
PCA	Principal Component Analysis
PDS	Planetary Data System
RADAR	Radio Detection and Ranging
RoIs	Regions of Interest
SAR	Synthetic Aperture Radar
USGS	United States Geological Survey
VIMS	Visual and Infrared Mapping Spectrometer
WGPSN	Working Group for Planetary System Nomenclature

Chapter 1

INTRODUCTION

1.1 CASSINI-HUYGENS & TITAN

Titan was first discovered in the XVIIth century by the Dutch astronomer Christiaan Huygens when he was looking for the Saturnian rings with a self-made telescope. The moon was then considered as the largest of the Saturnian moons and the second of our Solar System (Figure 1.1), with a radius of about 2,575 km (*Lindal et al.*, 1983). Titan is smaller than Ganymede (2,634 km) and larger than Earth's Moon (1,737 km) or even Mercury (2,440 km). Surprisingly, Titan is the only satellite that possesses a thick atmosphere, which was first probed by the Pioneer and Voyager spacecrafts in the 1980s. Titan's atmosphere is mainly composed of dinitrogen (N_2, 95 - 98.4%) and methane (CH_4, 1.6 - 5%), and shows a very complex and active photochemistry (*Hanel et al.*, 1981; *Tyler et al.*, 1981). Ultraviolet sunlight breaks up methane molecules and subsequent reactions build up complex hydrocarbons gases including ethane (C_2H_6), acetylene (C_2H_2), propane (C_3H_8), benzene (C_6H_6) (*Danielson et al.*, 1973; *Gillett et al.*, 1973; *Gillett*, 1975), and brownish solid organic particles (aerosols) (*Sagan*, 1971; *Khare and Sagan*, 1973). Moreover, the temperature and pressure conditions[1] predicted on Titan's surface are close to the point of stability of methane and ethane (*Flasar*, 1983; *Lunine et al.*, 1983). Thus, methane and ethane are stable in liquid state and might behave like water on Earth, as it forms clouds, rain and rivers, and hence describing a hydrocarbon cycle on Titan similar to the terrestrial water cycle. Besides the gases in Titan's atmosphere, aerosols form haze layers that are opaque at optical wavelengths, and conceal the entire surface of the moon. Such haze layers act like the urban photochemical smog in big cities on Earth. Titan's aerosols are spectrally similar to the sticky brownish molecules produced in laboratory by *Sagan and Khare* (1979), and referred as tholins from the Greek '*tholos*' for muddy. Titan's surface being entirely hidden by its dense and hazy methane-laden atmosphere, direct investigation of the surface geology is only possible using

[1] On Titan's surface, T = 93.7 K (-180°C) and P = 146.7 kPa (1.45 bar)

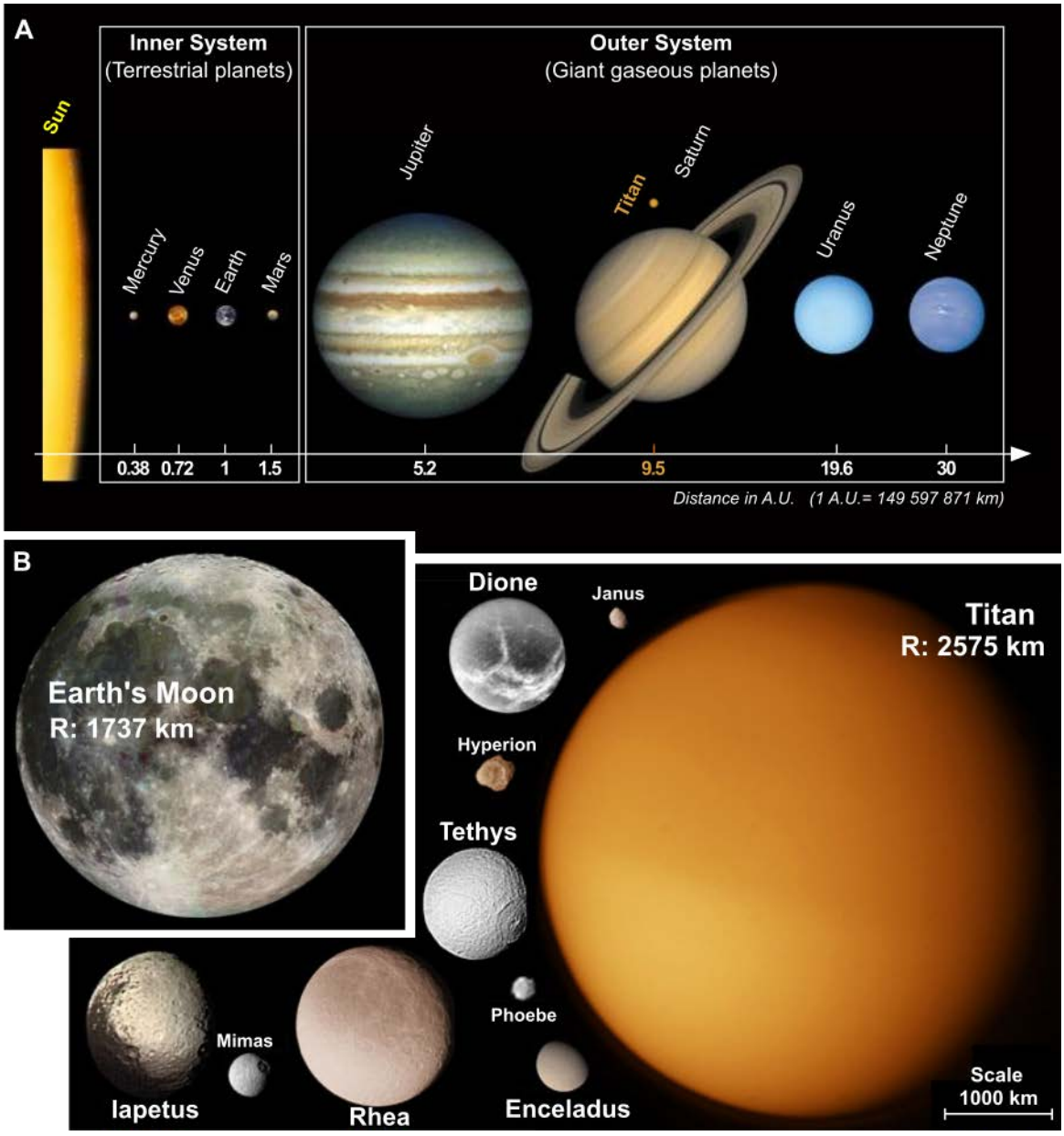

Figure 1.1 – (A) Titan in the Outer Solar System. (B) Size-comparison of the Saturnian satellites, with the Earth's Moon. Titan is significantly the largest moon of Saturn with a radius about 2,575 km, and its surface is hidden by a thick organic-rich atmosphere (dinitrogen and hydrocarbons). Titan's picture was taken by the Voyager 1 during its flyby in 1980. Credits: NASA/JPL-Caltech/Space Science Institute.

radar, and spectroscopic imaging at a few narrow wavelength intervals in the infrared, where the methane absorption is weak. These wavelength intervals are called atmospheric windows and allow us to inspect the surface of the moon (*Griffith et al.*, 1991; *Lemmon et al.*, 1993).

On Titan, methane plays the role that water does on Earth, as it controls a wide variety of atmospheric and surface processes that shape the moon's surface. Nonetheless, owing the short lifetime of methane (10-30 Myr, *Atreya*, 2010), Titan must have large stores of

methane that feed the gas into the atmosphere through several possible mechanisms, such as cryovolcanism (*Tobie et al.*, 2006; *Lopes et al.*, 2007a, 2013); methane evaporation from open liquid bodies (*Mitri et al.*, 2007); and exchange with methane hydrates (clathrates) trapped within Titan's crust (*Choukroun and Sotin*, 2012). Titan's atmosphere, surface and interior seem therefore interconnected and, in order to understand the origin and evolution of this moon, it is crucial to study its surface geology as it can provide pertinent insights into the nature of these exchanges. Thus, to constrain the geological evolution of Titan, it is important to determine its surface morphology and composition that may indicate specific surficial activity on the moon.

Through a joint endeavor of National Aeronautics and Space Administration (NASA[2]), European Space Agency (ESA[3]) and Italian Space Agency (*Agenzia Spaziale Italiana*, ASI[4]), the Cassini orbiter was launched in October 1997 along with the Huygens probe to successfully reach the Saturnian system in July 2004. Since then and until September 2017, the Cassini orbiter has gathered a large amount of data about Titan. Hence, the Cassini-Huygens mission allowed a real revolution in the exploration of the moon, particularly through the superposition of data acquired by the remote sensing instruments onboard the orbiter:

- RAdio Detection And Ranging instrument (RADAR, *Elachi et al.*, 2004)
- Visual and Infrared Mapping Spectrometer (VIMS, *Brown et al.*, 2004)
- Imaging Science Subsystem camera (ISS, *Porco et al.*, 2004)

Thus, these three instruments established the perfect combination to lead the first comprehensive investigations of Titan's surface geology. The surface albedo reflecting compositional properties of the surface is obtained by analyzing the infrared data collected by the VIMS and ISS instruments. In the meantime, the surface morphology is retrieved by the integration of Synthetic Aperture Radar (SAR) data from the RADAR instrument. SAR data permit the identification of many geomorphologic units on the moon based on variation in surface roughness (brightness in SAR swaths) at global scale (*Lopes et al.*, 2010, 2016) and regional scale (*Birch et al.*, 2016a; *Malaska et al.*, 2016a). Here, the term "geomorphologic units" means surface terrains with distinct geological characteristics, and often referred as landscapes in this dissertation. Thus, albedo differences and similarities among the diverse landscapes on Titan give insights on the geologic processes affecting the surface of the moon. Although being an icy moon, Titan has - in many aspects - a complex, dynamic and Earth-like surface. Understanding the interplay of geologic processes on Titan is important for modeling the interactions between its interior, surface and atmosphere, and climate evolution.

[2]NASA website: https://www.nasa.gov/
[3]ESA website: https://www.esa.int
[4]ASI website: https://www.asi.it

While flying by Titan, the Cassini orbiter rapidly showed evidence of several linear and dendritic fluvial networks crossing the moon's surface (*Jaumann et al.*, 2008; *Langhans et al.*, 2012). These fluvial features were first seen by Huygens' imager, during its descent through the atmosphere and towards the surface in January 2005 (*Tomasko et al.*, 2005). Numerous channels are later seen through the RADAR SAR swaths, as they flow into lakes and seas (*Stofan et al.*, 2007) and are filled with liquid hydrocarbons (*Brown et al.*, 2008). Titan's lakes and channels appear to be essentially confined around the poles (*Hayes et al.*, 2008, 2011). The low latitudes are mostly occupied by linear features appearing dark in infrared and radar datasets, and are probably made of organic sand (*Soderblom et al.*, 2007a; *Rodriguez et al.*, 2014). These linear features form large dune fields and sand seas that are very similar to those seen on Earth's desertic regions (*Radebaugh et al.*, 2008; *Lorenz and Radebaugh*, 2009). Besides the polar lakes and the equatorial dunes, Titan exhibits many other landscapes that are identified through SAR swaths, including mountainous terrains, several types of plains, labyrinth terrains (similar to terrestrial karstic plateaus), impact craters, and also putative cryovolcanic edifices (*Lopes et al.*, 2010). Figure 1.2 displays a brief overview of the major landscapes found on Titan with SAR imagery at a wavelength scale of 2.18 cm. *Lopes et al.* (2016), using the SAR data acquired during the 2004-2013 period, showed that the undifferentiated plains are the most widespread terrains on Titan's surface, while the second most common terrains are the dunes. Mountainous and hummocky terrains are also widely distributed on Titan. Other surface terrains described in *Lopes et al.* (2016) show smaller coverage areas, such as labyrinth terrains, lakes and craters.

Alternatively, by using infrared data from the VIMS (λ = 0.93 - 5.12 µm) and ISS (λ = 0.93 µm) instruments, the first global maps of Titan's surface albedo were produced (*Barnes et al.*, 2007a; *Turtle et al.*, 2009). These maps depict a latitudinal zonation in Titan's spectral characteristics and a few spectral units are therefore identified and described based on their appearance in the false color composites of uncorrected VIMS bands (*Barnes et al.*, 2007a; *Soderblom et al.*, 2007a). At the low latitudes, the areas with low albedo and hence being dark in the images correspond to the dune fields and sand seas, whereas they coincide with hydrocarbon lakes and seas around the poles. Figure 1.3 shows that dark areas near the equator display two types of infrared (also noted IR) units; the IR-brown and IR-blue units, appearing as such in the false color composites. The IR-brown unit appears to be in very good agreement with the dunes seen in SAR data (*Soderblom et al.*, 2007a; *Rodriguez et al.*, 2014), while the IR-blue unit is thought to be slightly enriched in water ice material laying on surface (*Rodriguez et al.*, 2006; *Barnes et al.*, 2007b; *Jaumann et al.*, 2008, 2009; *Le Mouélic et al.*, 2008). Besides the dark polar lakes and equatorial dunes, the major part of Titan's surface appears bright in the near-infrared, and hence called the IR-bright unit. Indeed, the IR-bright unit shows a high reflectivity in all atmospheric windows, and might be consistent with a layer of organic sediments coating the moon's substratum (*Barnes et al.*, 2007a;

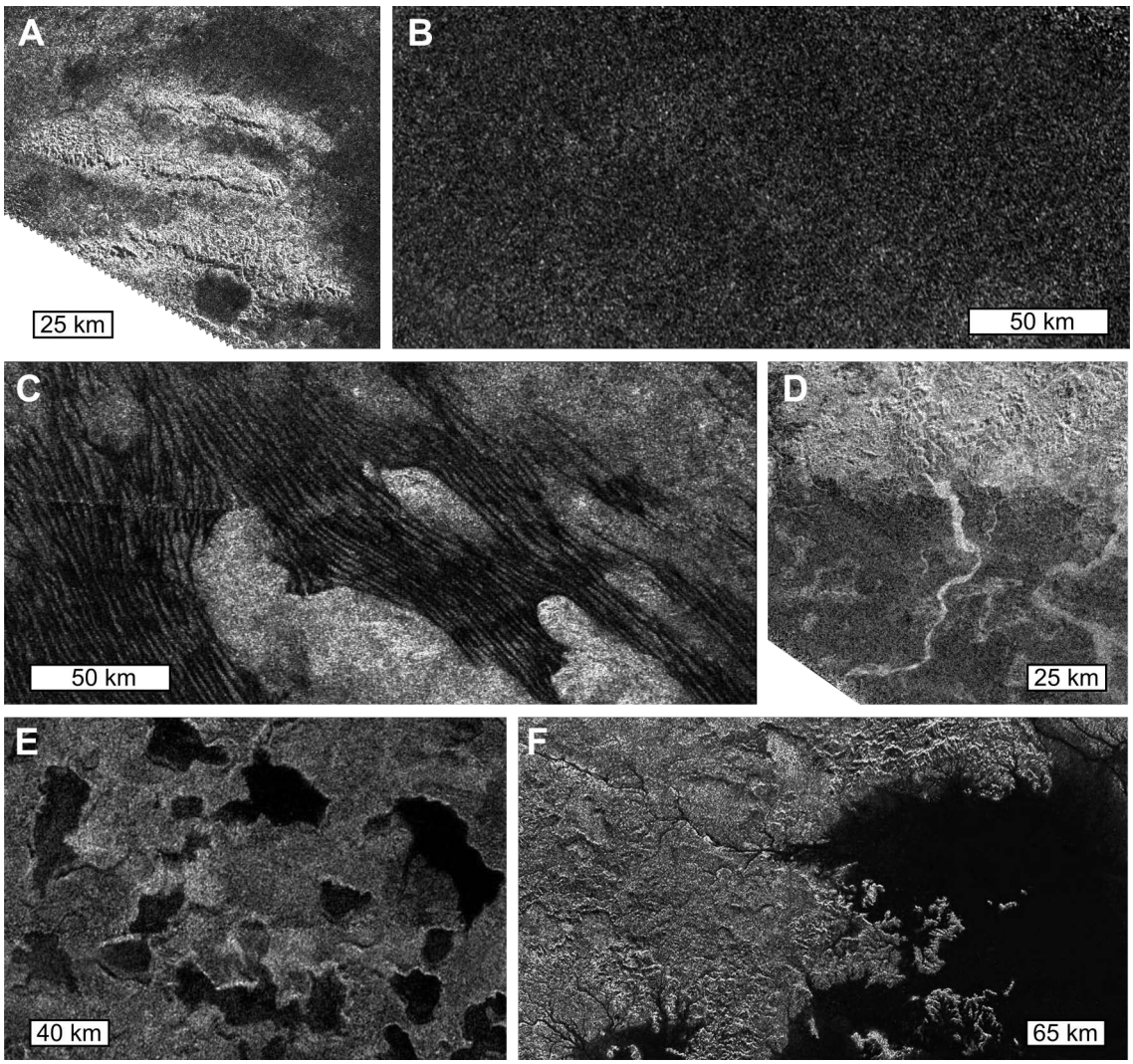

Figure 1.2 – Overview of Titan's landscapes seen through Cassini's RADAR SAR swaths (λ = 2.18 cm), including (A) mountain chains, (B) undifferentiated plains, (C) longitudinal dunes, (D) river channels, (E) small lakes, and (F) close up of the second largest sea, namely Ligeia Mare, which show islands, cays and other features evocative of terrestrial seas.

Soderblom et al., 2007a). In addition to the previous infrared units, some isolated regions near the equator are particularly very bright at longer wavelengths (above 2.7 µm), and could be ancient lakebeds filled with evaporitic deposits similar to those found at proximity to the lakes (e.g. *Barnes et al.*, 2011a; *MacKenzie et al.*, 2014).

Even though some ideas have been raised about the surface composition of Titan (e.g. *Coustenis and Bézard*, 1995a; *Griffith et al.*, 2003; *Hartung et al.*, 2006; *McCord et al.*, 2006, 2008; *Clark et al.*, 2010; *Singh et al.*, 2016), the precise chemical composition of the material composing - or coating - the surface terrains on the moon has not been clearly defined to date. In my doctoral research I used a combination of datasets collected by VIMS, ISS and RADAR in its SAR imaging mode acquired throughout the Cassini mission (2004 - 2017) and applied new updated analysis techniques to optimize the retrieved surface information. My

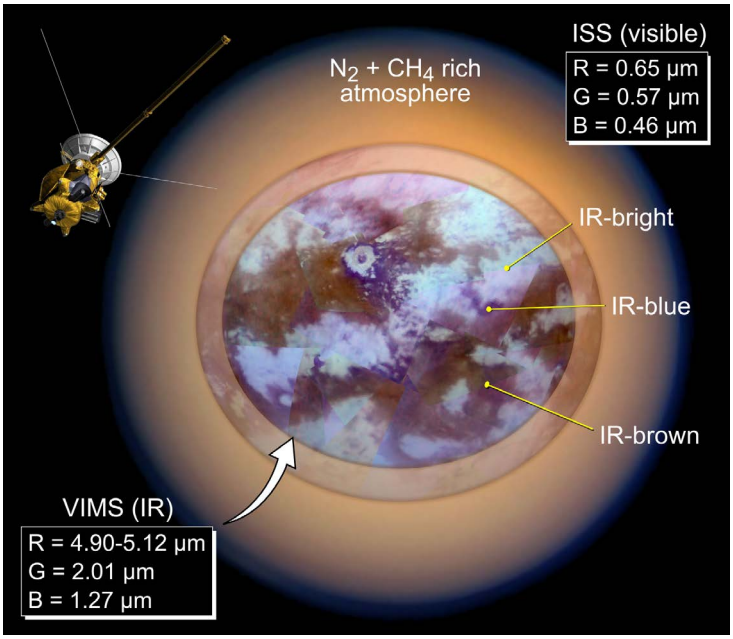

Figure 1.3 – Titan looks like a fuzzy orange ball as shown by Cassini's ISS camera. The image is false-colored to approximate what human eye might see (*Porco et al.*, 2005). However, Titan's surface is unveiled in a few wavelength intervals in the infrared, as shown in a false color composite of VIMS bands in the atmospheric windows (*Le Mouélic et al.*, 2016), in which infrared units are identified.

main objective was to constrain the geological evolution of the surface units at low-latitudes (± 40°N/S, also called equatorial belt in this dissertation). As mentioned earlier, methane plays an important role on Titan. Around the wet polar regions, methane story seems quite understood, as the gas is expected to evaporate from lakes, form clouds, precipitate out, carve valleys and flow back into lakes (*Raulin*, 2008). Nonetheless, the desert-like equatorial regions remain enigmatic about the geologic processes involved and their relations with methane's fate. Sand material composing the dunes is supposed to derive from the haze particles formed by the action of sunlight on atmospheric methane, but the mechanism to build sand from smaller haze particles is not yet understood (*Barnes et al.*, 2015).

My first approach was thus to produce an updated, global geomorphologic map of Titan's surface in order to identify the major landscapes present on the moon. This aimed to characterize the global geographic distribution of many landscapes, particularly for the dunes and lakes that are thought to be the youngest surface features on Titan (*Lopes et al.*, 2010). My second approach was then to determine the compositions of the major terrains identified at low latitudes, which mainly consist of dunes, mountains and plains. This helped me to better constrain the origin, nature and evolution of these terrains and point out the surficial processes that shape the surface of the moon. I have therefore collected and processed the SAR data acquired by the RADAR instrument during the entire Cassini-Huygens mission to retrieve the morphological properties of the terrains on Titan. I have done the same with the infrared data collected by the VIMS and ISS instruments to identify and map the infrared units in the equatorial regions. The nature of the material composing these infrared units, remaining ambiguous so far, was constrained by applying an innovative radiative transfer code on VIMS data to extract surface information, and then combined with a spectral mix-

ing model to compare with surface candidates. Hence, by coupling the geomorphological and compositional analyses I was planning to constrain the nature of the material present at low-latitudes regions, and retrace the geologic processes that govern Titan's surface. Thus, by reconstructing the geological evolution of the landscapes, I was aiming to provide new insights on the possible interactions between the atmosphere, surface and perhaps interior of the moon and better understand the methane cycle occurring on Titan.

1.2 THESIS ORGANIZATION

Besides the current introduction being the first chapter, this dissertation is structured as follows. Chapter 2 presents the three remote sensing instruments onboard the Cassini orbiter and their observations acquired during the mission (2004 - 2017), and the techniques employed to analyze them. Hence, Chapter 2 is first dedicated to the description of the optical imaging instruments (ISS and VIMS), and the RADAR instrument with its SAR imaging mode used to complement my investigation, particularly for the production of an up-to-date global geomorphologic map of Titan. Then, the chapter focuses on the atmospheric contributions affecting the infrared observations and the application of techniques to compensate for them. This chapter concludes with a description of the spectral mixing model employed to complete my compositional analysis.

Then, the following chapter goes deeper into my research, as it is essentially focused on Titan's geomorphology and is supported by the geomorphologic map produced for this work using SAR data (see Chapter 3). This map is accompanied by a description and interpretation of the various landscapes identified during the Cassini-Huygens mission.

The next chapter shows how I have retrieved - or at least constrained - the surface composition of the major terrains present in the equatorial regions, in terms of composition and granulometry using VIMS data. Additionally, this last chapter discusses about possible geologic origin and evolution of the considered landscapes (see Chapter 4). The work reported in this chapter is now published at the Journal of Geophysical Research Planets (JGR Planets) (*Brossier et al.*, 2018).

The final chapter is a conclusion where I summarize the previous chapters and emphasizes my contributions in the exploration of Titan's geology (see Chapter 5). Note that supporting materials are appended at the end of this dissertation to give the reader further details about the processing of the SAR swaths (see Appendix A), and the extraction of surface albedo after applying a radiative transfer model in VIMS observations (see Appendix B).

1.3 CONTRIBUTIONS

During my doctoral research, I met many researchers from diverse institutions, as collaborators and advisors, who gave me the necessary support to reach my objectives. First of all, Prof. Ralf Jaumann [1,2] and Katrin Stephan [1] were regularly consulted during my stay in Berlin as my main advisors, and for the preparation of this thesis and the associated research article (*Brossier et al.*, 2018). Meanwhile, I have established a collaboration with Sébastien Rodriguez [3] and Luca Maltagliati [4], in Paris, where they contributed in the improvement of a radiative transfer code that we have applied on the VIMS data of my interest. This code was initially developed halfway through the Cassini mission and used by Mathieu Hirtzig [5], Athena Coustenis [6] and Anezina Solomonidou [7,8] (*Hirtzig et al.*, 2013; *Solomonidou et al.*, 2014; *Maltagliati et al.*, 2015), who were consulted before the submission of my research article. Still in Paris, Sébastien Rodriguez and Thomas Cornet [8] helped me in the development of a spectral mixing model that has been used to compare Titan's surface information with synthetic surface candidates. In Nantes, Stéphane Le Mouélic [9] advised me about the use of a semi-empirical technique that he adapted for VIMS data (*Le Mouélic et al.*, 2012) and that I have improved and used to correct for atmospheric effects and produce a new spectral map of Titan. As Co-Investigators in the VIMS team, it is through Prof. Ralf Jaumann and Prof. Christophe Sotin [7] that I accessed data from the VIMS instrument. Antoine Lucas [3] and Jani Radebaugh [10], for their part, were consulted to discuss about Titan's geology, particularly about the dune fields and their analogous in terrestrial desertic regions. Moreover, Antoine Lucas gave me access to denoised SAR swaths (*Lucas et al.*, 2014a) and topographic data derived from the SAR imaging mode (*Stiles et al.*, 2009).

Besides the external support, my own work was first dedicated to the integration of the data collected by Cassini's instruments over the course of the mission. The superposition of these data was used for the production of the most up-to-date geomorphologic and spectral maps of Titan's surface, as well as the selection of regions of interest for a more extensive compositional analysis once the VIMS observations were corrected for atmospheric effects. After inversion of the VIMS observations selected for this study with the radiative transfer model, I have extracted the surface information of the infrared units present in the regions of my interest and compared it with synthetic candidate compounds. Finally, based on the results of the combined geomorphological and compositional analyses, I have derived a series of geologic processes that could reasonably explain the distribution of surface units found in the investigated regions, which conduct to the submission of a research article at JGR Planets (*Brossier et al.*, 2018), as well as my regular participation in international conferences (*Brossier et al.*, 2015, 2016a,b, 2017a,b) and science team meetings.

Affiliations of Contributors

[1] Institute of Planetary Research, German Aerospace Center (DLR), Berlin, Germany, [2] Freie Universität Berlin, Germany, [3] IPGP, Université de Paris - Diderot, France, [4] Nature Publishing Group, London, UK, [5] Foundation "La Main à la Pâte", Montrouge, France, [6] Observatoire de Paris (LESIA), Paris - Meudon, France, [7] Jet Propulsion Laboratory, California Institute of Technology, Pasadena, CA, USA, [8] ESA European Space Astronomy Center (ESAC), Villanueva de la Cañada, Madrid, Spain, [9] LPG-Nantes, Université de Nantes, France, [10] Brigham Young University, Provo, UT, USA

Chapter 2

DATA & METHODS

2.1 CASSINI'S EYES

During many close encounters with Titan, the Cassini orbiter had the opportunity to learn about the geology occurring on the moon through its remote sensing instruments covering the visible to infrared (optical) and microwave ranges. The optical imaging data were collected by the ISS (*Porco et al.*, 2004) and VIMS (*Brown et al.*, 2004) instruments, while the microwave imaging data were acquired by the RADAR instrument in its SAR imaging mode (*Elachi et al.*, 2004). These three instruments greatly contributed in the investigation of Titan during the thirteen years of Cassini-Huygens mission (2004 - 2017). Data obtained by the RADAR instrument were mainly used to probe the surface of Titan, as RADAR's microwave radiation easily penetrates the atmosphere and interacts with the surface. However, infrared observations derived from the ISS and VIMS instruments were utilized to identify surface features and extract surface information, although they were not initially designed for imaging the surface of the hazy moon. In this section, I introduce the main characteristics about these three instruments, constituting the eyes of the Cassini orbiter during the survey of Titan.

2.1.1 IMAGING SCIENCE SUBSYSTEM (ISS)

The Imaging Science Subsystem (ISS) instrument was a pair of multi-band cameras that acquired two-dimensional observations with a relatively high spatial resolution (2-4 km) and was therefore highly suitable to reveal surface features on Titan (*Perry et al.*, 2005; *Porco et al.*, 2005). Figure 2.1 illustrates the two separate cameras, and Table 2.1 reports their main characteristics derived from *Porco et al.*, 2004. The narrow-angle camera (NAC) was a reflecting telescope designed to obtain high-resolution images of small areas, while the wide-angle camera (WAC) was a refractor designed to provide pictures of larger areas with a different resolution. Moreover, spectral filters attached to both cameras enable the instrument to provide observations from the ultraviolet to the near-infrared range (0.20 - 1.05 µm, in

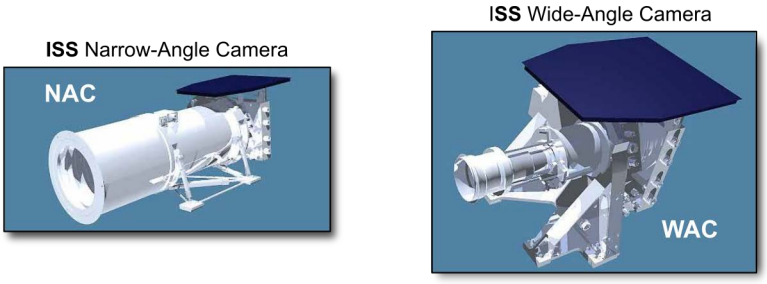

Figure 2.1 – Cutaway diagrams of the ISS cameras (*Porco et al.*, 2004).

Table 2.1 – ISS cameras characteristics (*Porco et al.*, 2004).

	Narrow - Angle Camera (NAC)	Wide - Angle Camera (WAC)
Spectral coverage	0.20 - 1.05 µm	0.38 - 1.05 µm
Number of filters	12 × 2 filters	9 × 2 filters
FOV	6.134 mrad (0.35°)	61.18 mrad (3.5°)

Note: FOV stands for field of view.

Table 2.1). As explained in *Perry et al.* (2005), despite the significant haze scattering at near-infrared wavelengths, it is possible to detect the surface of Titan through a narrow continuum band filter centered at 0.938 µm. This single filter being centered in the middle of a methane window, it was therefore mainly designed to study the surface of the moon through its dense atmosphere. Although, the detection of surface features is roughly possible with this filter, the retrieval of compositional information remains hardly feasible.

Since I was not involved in the ISS team during my research, I had no access to the calibration and processing tools and hence I did not process the ISS data. However, after their acquisition, the observations are mosaicked to produce global maps of the Titan's surface albedo at 0.938 µm. The maps are regularly produced and released by the ISS team[1]. The most recent map (Figure 2.2) is radiometrically preprocessed and geometrically projected into a simple cylindrical projection at a scale of about 4 km per pixel. The mosaic was produced in June 2015 and comprises data collected through flyby T100 (April 2014). Here, Titan flybys are tagged with the abbreviated target name 'T' and the flyby number (e.g. 'T3' refers to the third flyby of Titan), with the exception of the first two Titan flybys, namely 'Ta' and 'Tb'. Actual resolution varies greatly across the map, with the best coverage along the equator near the center of the map at 180°W. The lowest resolution coverage can be seen in the northern mid-latitudes. The uniform white area in the northern hemisphere indicates a gap in the imaging coverage of Titan's surface of about 3-5%. Thus, during my compositional analysis, this present mosaic was mostly used as basemap, particularly to complement the VIMS data during the mapping of the infrared units (see Chapter 4).

[1]Link to the ISS map: http://www.ciclops.org

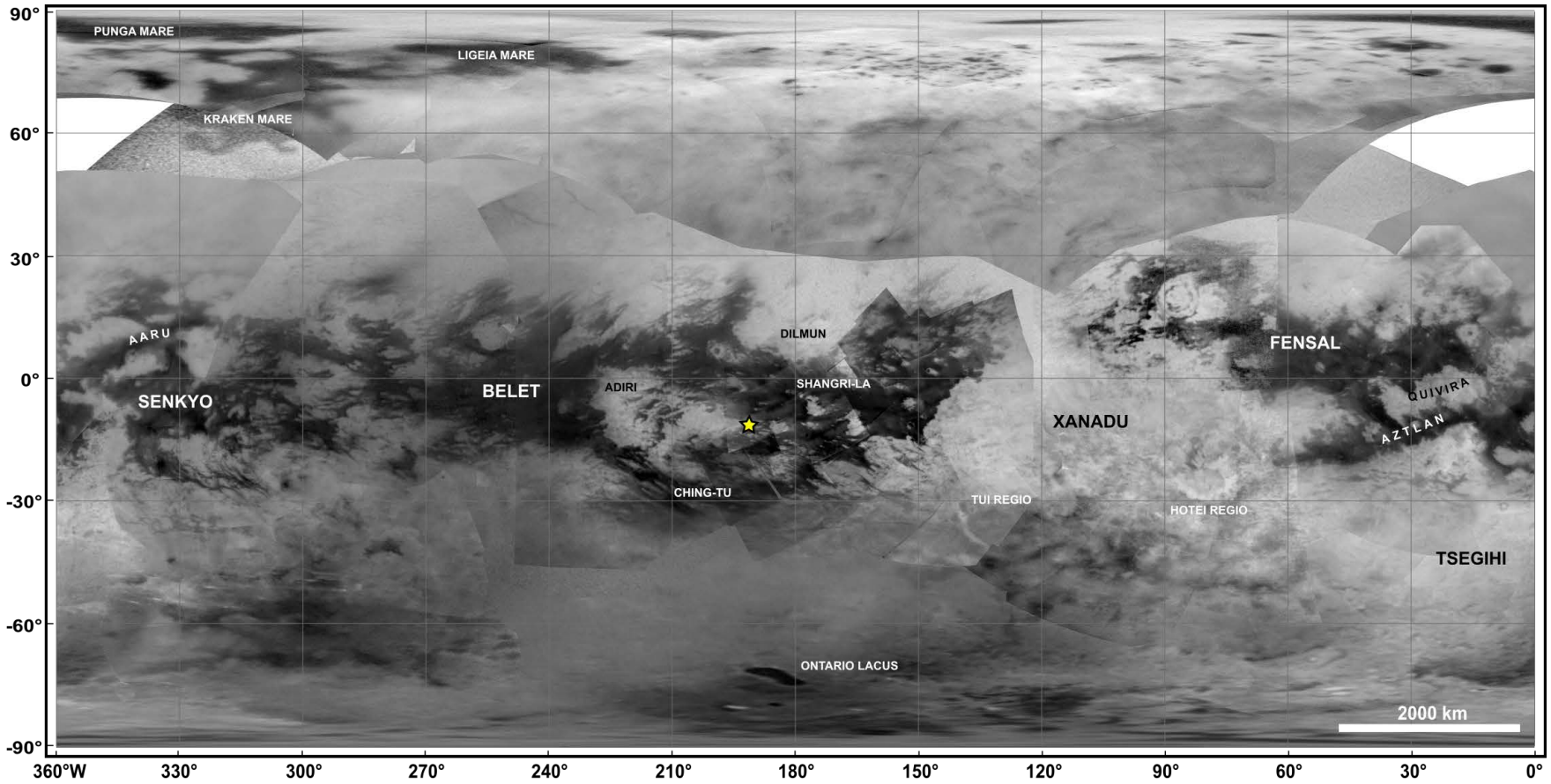

Figure 2.2 – Global mosaic of Titan's surface through ISS data (up to April 2014) displayed at 0.938 µm, allowing to evaluate the surface albedo variations. The map is shown in a simple cylindrical projection centered at 0°N and 180°W, with a scale of about 4 km/pixel. The yellow star indicates the location of the Huygens landing site. Credit: NASA/JPL-Caltech/Space Science Institute (PIA19658).

Table 2.2 – VIMS-VIS and -IR sensors characteristics (*Brown et al.*, 2004).

	VIMS - VIS	VIMS - IR
Spectral coverage	0.35 - 1.05 µm	0.85 - 5.12 µm
Spectral sampling	7.3 nm/spectral (96 bands) (1 × 5 sum)	16.6 nm/spectral (256 bands)
Observation mode	Push-broom	Whisk-broom
IFOV	0.167 × 0.167 mrad	0.25 × 0.5 mrad
Effective IFOV	0.5 × 0.5 mrad (3 × 3 sum)	0.5 × 0.5 mrad (1 × 2 sum)
Total IFOV	64 × 64 pixels (32 × 32 pixel mrad)	64 × 64 pixels (32 × 32 pixel mrad)
Swath width	576 IFOVs (3 × 3 × 64)	128 IFOVs (2 × 64)

Note: IFOV stands for instantaneous field of view.

2.1.2 VISUAL AND IR MAPPING SPECTROMETER (VIMS)

The Visual and Infrared Mapping Spectrometer (VIMS) was a pair of imaging spectrometers dedicated to probe Titan in the visible and infrared ranges (*Brown et al.*, 2004). When looking through atmospheric windows at infrared wavelengths, VIMS enabled the identification of surface features. Each imaging spectrometer obtained two-dimensional image that can be displayed as a grayscale map representing the surface, exactly as ISS at 0.938 µm. Every pixel of the image contains spectral information, which is added as a third dimension of values to the two-dimensional spatial image, generating a three-dimensional data cube, often referred as observation cube (Figure 2.3). VIMS covered a broad spectral range as it measured the radiance factor (also noted I/F) from 0.35 to 5.12 µm (*Brown et al.*, 2004). The radiance factor is defined as the radiance reflected off the surface, where I is the observed intensity and πF is the incident solar flux. The two separate imaging spectrometers, namely the VIMS-VIS and VIMS-IR sensors (Figure 2.3C), had distinct spectral range, spectral and spatial resolution and operation modes, as reported in Table 2.2 (*Brown et al.*, 2004). As described in *Jaumann et al.* (2006), the VIMS-VIS sensor was collecting the reflected visible light of the target in 96 spectral channels between 0.35 and 1.05 µm, with a spectral resolution going from 1.46 to 7.3 nm. The visible sensor used a two-dimensional detector to provide a two-dimensional spatial coverage in a push-broom mode in which the surface was imaged line by line. As the spacecraft flew forward, the cube was generated one line at a time, with all of the pixels in a line being measured simultaneously. As for the VIMS-IR sensor, it includes 256 spectral channels in the infrared range (0.85 - 5.12 µm) with a spectral resolution of 16.6 nm (*Jaumann et al.*, 2006). The infrared sensor was a one-dimensional focal plane detector operating in whisk-broom mode. Thus, it detected the entire spectrum of one single pixel per exposure and probed the surface in both spatial directions, supported by a secondary mirror moving back and forth.

VIMS data are archived and made publicly available through the NASA Planetary Data

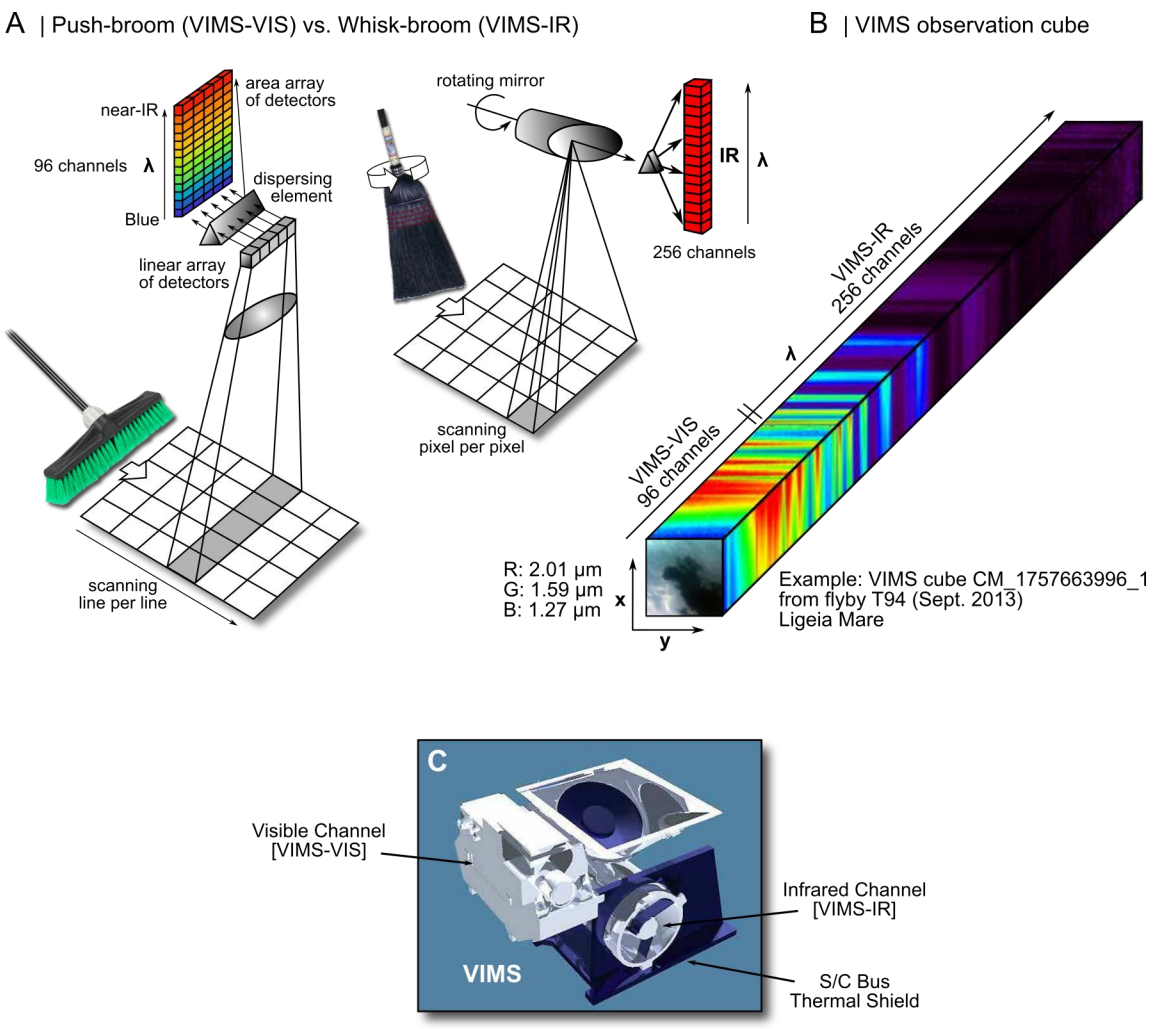

Figure 2.3 – (A) Operation modes for the VIMS sensors: push-broom (VIMS-VIS) and whisk-broom (VIMS-IR), and (B) a classical VIMS observation cube with the 352 channels (*Cornet*, 2012b, modified). (C) Cutaway diagram of the VIMS sensors (Credits: ASI/ESA/NASA).

System Imaging Node portal (PDS[2]). However, through my main supervisor Prof. Ralf Jaumann (DLR, Germany) and also my remote supervisor Sébastien Rodriguez (IPGP, France) who are both members of the VIMS team, I was able to freely integrate VIMS data and access a plethora of techniques for atmospheric corrections. Hence, the processing and correction of VIMS data introduced in Section 2.2 were mainly achieved at the DLR and also at the IPGP during my few stays in France.

2.1.3 RADAR

The RAdio Detection And Ranging (RADAR) was a multimode Ku-band (13.8 GHz, $\lambda = 2.18$ cm) radar instrument (*Elachi et al.*, 2004). RADAR's microwaves are not affected by the dense atmosphere of Titan or the solar illumination, and the instrument was therefore

[2]Link to datasets: https://pds-imaging.jpl.nasa.gov/volumes

Table 2.3 – RADAR's modes characteristics (*Elachi et al.*, 2004).

Modes	Altitude (km)	Inc. (°)	Resolution (km/pixel)			Noise (dB)	Looks	Coverage (%)
			Azimuth	Range	Vertical			
H-SAR	1 000 - 1 600	21 - 30	0.35 - 0.41	0.48 - 0.64	-	-28 to -21	2 - 3	≤ 1.1
L-SAR	1 600 - 4 000	15 - 28	0.41 - 0.72	0.48 - 2.70	-	-25 to -15	2 - 7	≤ 1.1
ALT	4 000 - 9 000	0	24 - 27	24 - 27	35 - 40	-3 to -35	16 - 36	-
SCAT	9 000 - 22 500	0 - 30	55 - 140	55 - 140	-	-4 to -36	-	20
RAD	1 000 - 100 000	0 - 80	6 - 600	6 - 600	-	-	-	40

Note: H-SAR = high resolution SAR, L-SAR = low resolution SAR, ALT = Altimetry, SCAT = scatterometry and RAD = radiometry. Altitudes are reported in km, incidence angles in degrees, resolutions in km/pixel, noises in dB and surface coverages in %.

designed to evaluate the physical properties and composition of the surface (*Elachi et al.*, 2005). Data obtained in Synthetic Aperture Radar (SAR) mode were originally used for the identification and interpretation of surface features on Titan's surface (*Elachi et al.*, 2005; *Stofan et al.*, 2006), and later for the first detailed mapping of the geomorphologic units at larger scales (*Lopes et al.*, 2010; *Moore et al.*, 2014) as shown in Chapter 3. RADAR operated in four different modes to probe the surface: the altimetry, scatterometry and radiometry modes, and the most relevant for this study, the SAR imaging mode. RADAR modes depend of the distance between the spacecraft and Titan's surface during a flyby, as reported in Figure 2.4A and Table 2.3. In active SAR imaging mode, the brightness in the images is influenced by the surface properties, such as surface slopes, dielectric properties, amount of volume scattering, and roughness at a wavelength scale of 2.18 cm (*Elachi et al.*, 2006). When the Cassini orbiter was close to Titan, the side-pointing was mainly used in SAR imaging mode while the nadir pointing (i.e. incidence angle at 0°) was mainly used in altimetry (Figure 2.4B).

2.1.3.1 SYNTHETIC APERTURE RADAR (SAR)

The SAR imaging mode enabled the mapping of Titan's surface through the shape of long thin strips, also referred as 'swaths', with resolutions varying from 350 m at closest approach distances of about 950 km above Titan to over 1 km at the maximum range for standard SAR imagery (*Elachi et al.*, 2004) (Figure 2.4A). SAR data usually have a higher resolution in the center than at the edges. The swaths acquired during the SAR imaging mode are around 120-450 km wide and about 5,000 km long regarding the spacecraft track.

SAR data used during my investigation are archived in the NASA PDS Imaging Node portal. I realized the whole geometric preprocessing of the SAR swaths within the USGS image processing environment named Integrated Software for Imagers and Spectrometers version 3 (ISIS3), which essentially consist in the conversion and projection of the swaths for their integration into a geographic information system (GIS). For further details about

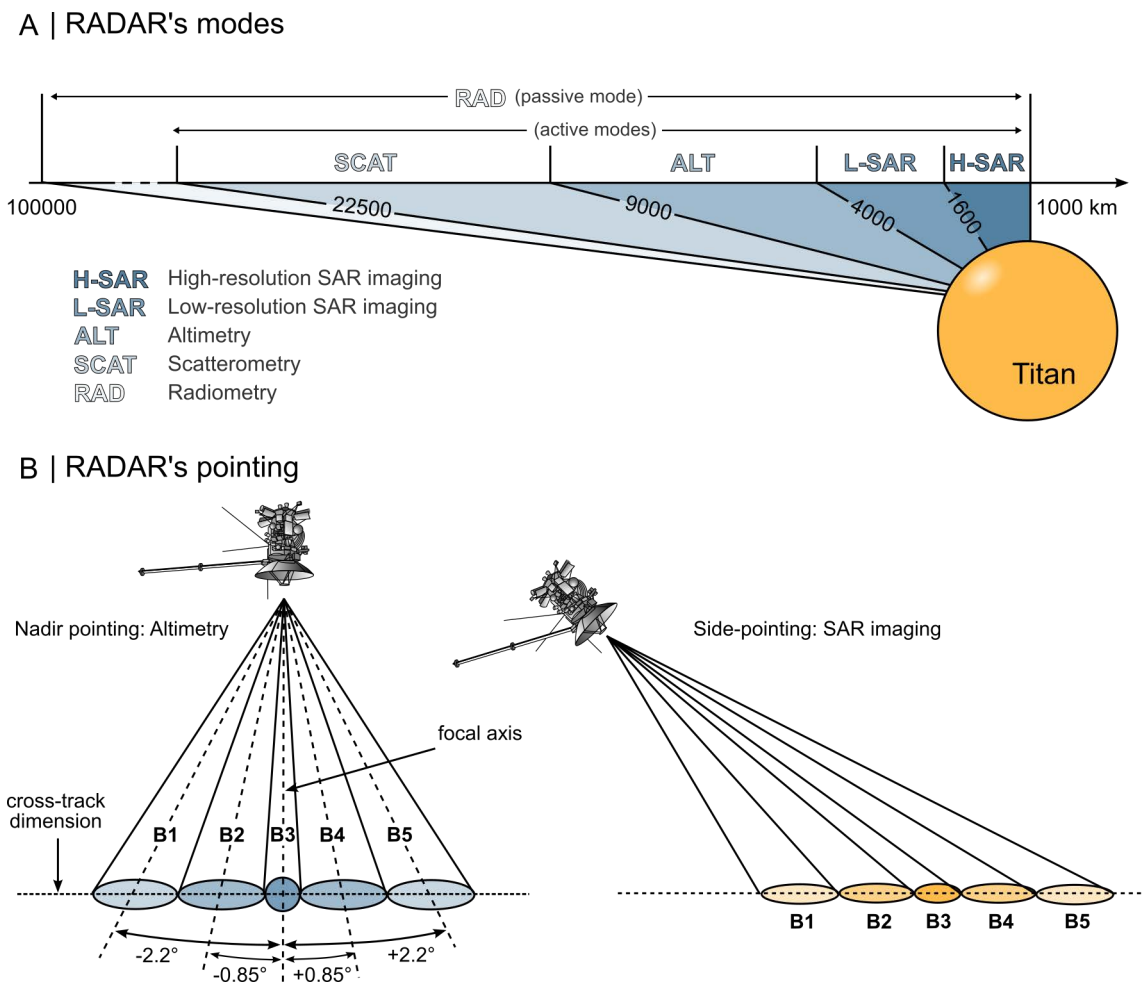

Figure 2.4 – (A) Sequence of RADAR modes on a typical Titan flyby, adapted from *Paganelli et al.* (2008). (B) RADAR's nadir pointing and side pointing used in (left) altimetry mode and (right) SAR imaging mode, respectively (*Elachi et al.*, 2004).

the processing of SAR data within ISIS3, the reader is referred to the pipeline described in Appendix A. SAR data were processed and reprojected into a simple cylindrical projection and centered at 180°W and 0°N, in order to be integrated into a GIS and then to produce an updated global mosaic (Figure 2.5). Indeed, the SAR swaths that I have integrated into this mosaic were collected from the first close Titan flyby Ta (October 2004) to the most recent and available set of swaths from flyby T120 (June 2016). The two last Titan flybys with SAR imagery were performed in July 2016 (T121) and April 2017 (T126), and the corresponding swaths are not used in this work since they are not yet calibrated and publicly released.

Through their high resolution, SAR data provide useful information in conjunction with the infrared data from both the ISS and VIMS instruments, as they offer a more global context. Since the beginning of the Cassini-Huygens mission, many regions on Titan have been investigated by superposing these datasets. To date, the SAR swaths cover about 65.7% of Titan's surface area through June 2016, which represent about 54.7 million km^2 (Figure

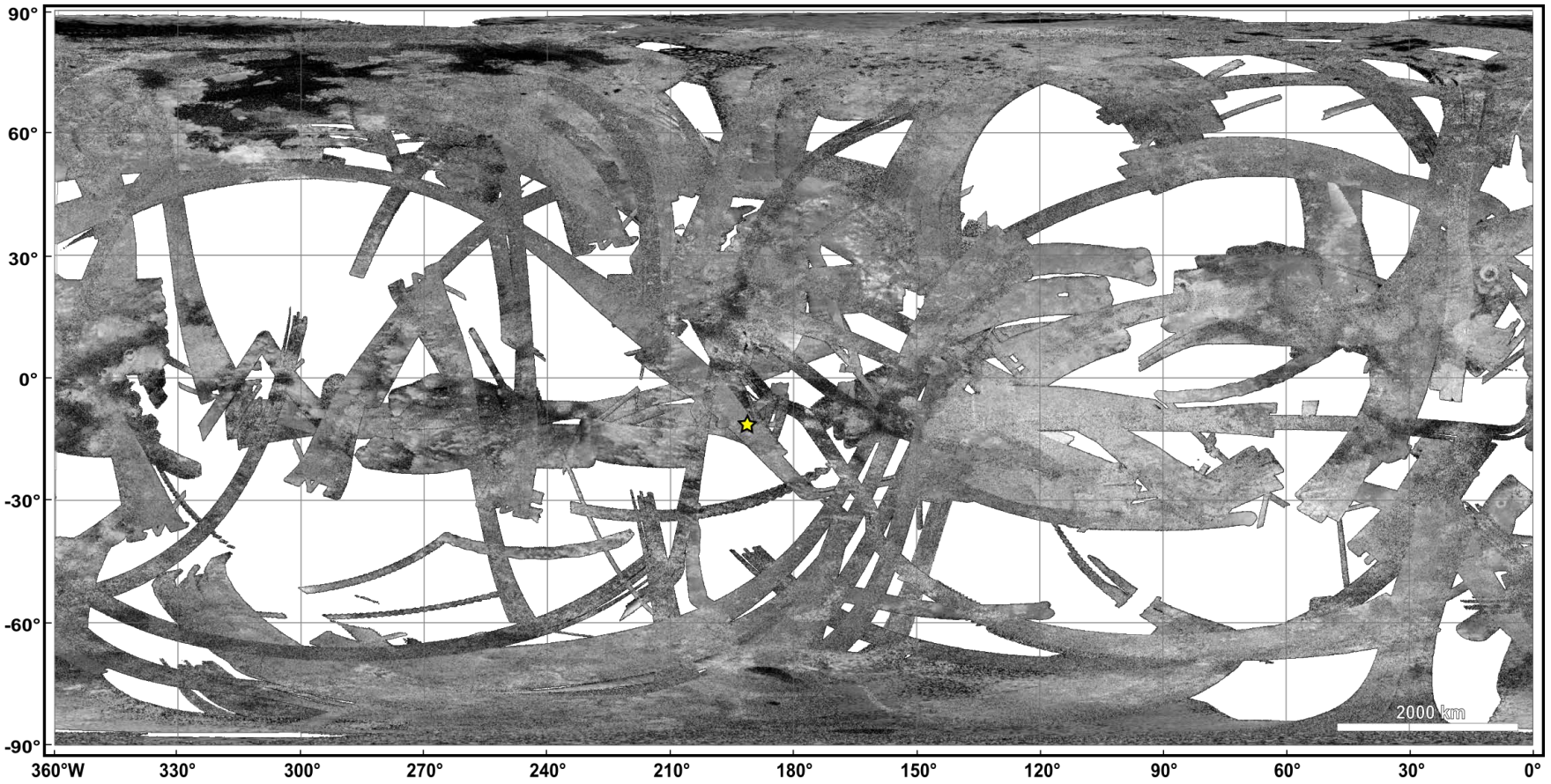

Figure 2.5 – Global map of Titan's surface through a mosaic of SAR swaths (2.18 cm-wavelength) that I have processed and integrated into the ArcGIS software package, including observations up to June 2016. The map is shown in a simple cylindrical projection centered at 0°N and 180°W, with SAR resolution varying between 350 m to over 1 km. The yellow star indicates the location of the Huygens landing site.

2.5). Since the RADAR microwave was insensitive to illumination conditions, the whole surface of the moon is imaged in quasi equal proportions: the northern polar region is then covered at about 81.3% (50-90°N), while the southern polar region is slightly less covered, at 67.5% (50-90°S). Otherwise, the equatorial belt has received relatively good coverage of about 65.6%, even with many overlapping SAR data, which represent about 35.1 million km^2 within 40° of latitudes.

Moreover, as RADAR was able to penetrate Titan's clouds and haze to provide high resolution views of the surface geology, I have produced a global map of the major geomorphologic units seen on the moon. Such map allows to illustrate the global distribution of the main landscapes, and to seek possible relations to each other in terms of setting and emplacement history. The resulting map and the description of the major landscapes are given in the following chapter (see Chapter 3).

2.2 ATMOSPHERIC CORRECTIONS

To date, many recent geologic investigations have been accomplished on the base of SAR data, as they provide pertinent information about the landscapes present on Titan's surface (e.g. *Birch et al.*, 2016a,b; *Lopes et al.*, 2016; *Malaska et al.*, 2016a). Nonetheless, such studies remain quite limited with microwave imaging, and it is therefore essential to introduce the use of infrared imaging spectroscopy in order to obtain further information about the material covering the surface of the moon. Indeed, by coupling the two - microwave and infrared imaging - datasets it would be possible to reveal the surface processes that govern Titan's surface. A few techniques were therefore developed and applied to pass through the dense atmosphere of Titan and reach its surface. Hence, these techniques allow retrieving the nature of the surface materials present on Titan and eventually their granulometry.

2.2.1 ATMOSPHERIC CONTRIBUTIONS

As demonstrated in earlier studies, imaging spectroscopy allows the identification of surface materials and the evaluation of their physical properties (e.g. composition, grain size) by analyzing their spectral signature (e.g. *Brown and Cruikshank*, 1997). Hence, it is necessary to integrate the spectral data collected by VIMS in order to constrain the compositional properties of the surface materials. Nonetheless, during my investigation, the major issue encountered when analyzing infrared observations of Titan appears to be the dense and opaque atmosphere of the moon. Indeed, Titan's atmosphere obstructs the view of the surface owing to gases absorption essentially by methane (CH_4) and to backscattering by aerosols (*Combes et al.*, 1997; *Rodriguez et al.*, 2006). Indeed, a small quantity of atmospheric methane is enough to affect Titan's spectrum, and conduct to strong molecular absorption

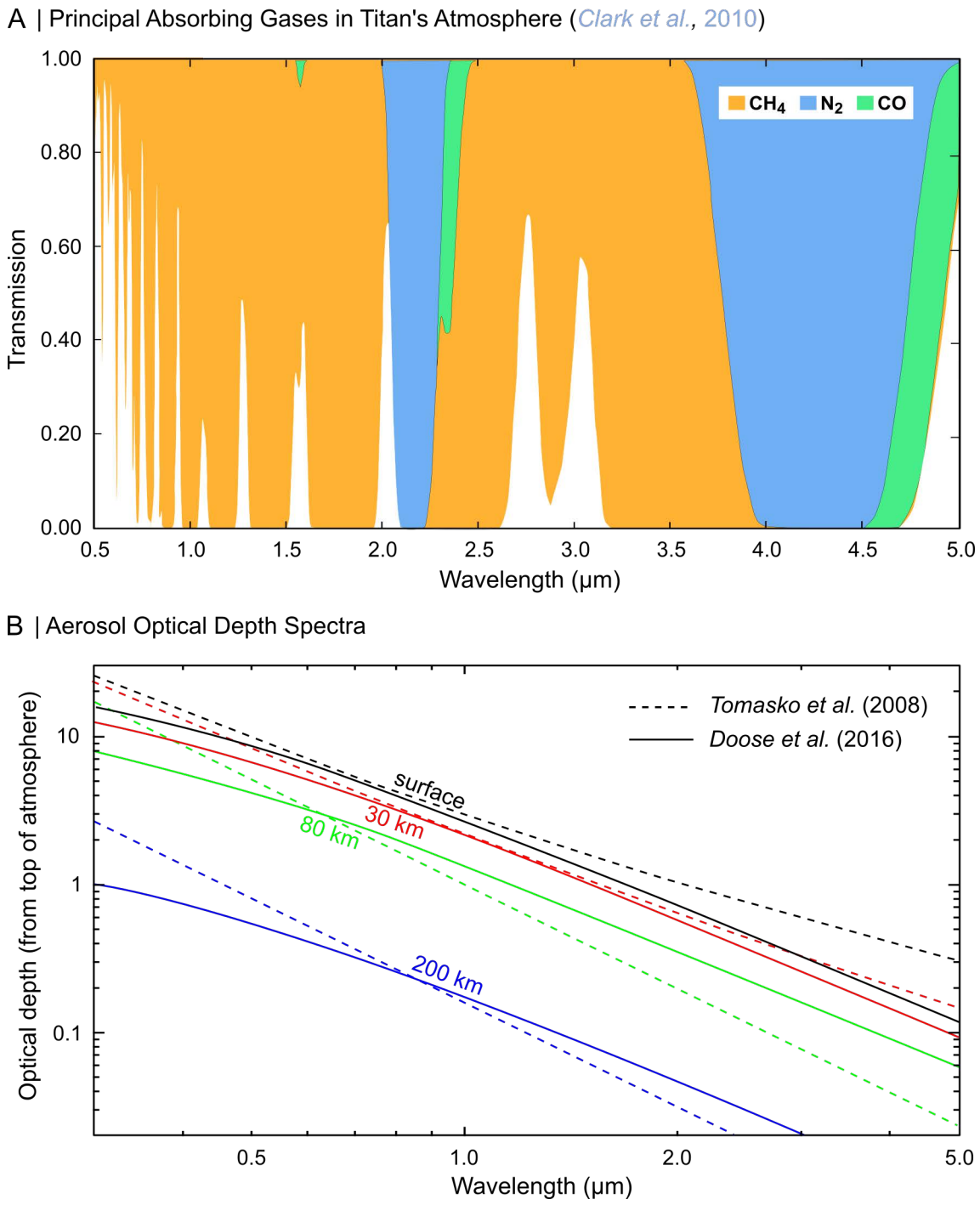

Figure 2.6 – (A) Dominant absorbing gases in Titan's atmosphere over the VIMS spectral range (*Clark et al.*, 2010). (B) Aerosol optical depth spectra at four altitudes adapted from *Tomasko et al.* (2008) and *Doose et al.* (2016) (dashed and solid curves, respectively).

preventing the direct detection of the surface (*Combes et al.*, 1997). Hopefully, there are a few narrow spectral windows in the near-infrared range where the atmospheric gases absorption is weak, and where the surface is therefore visible. These atmospheric windows are centered at 0.76, 0.83, 0.94, 1.08, 1.27, 1.57, 2.01, 2.7-2.8, and 4.90-5.12 µm (Figure 2.6A, *Clark et al.*, 2010). Due to the dominant atmospheric contributions within the spectrum and the narrow size of most of the windows, VIMS imaging spectroscopy would be rather suitably labeled as a multispectral technique instead of hyperspectral (*Jaumann et al.*, 2008).

Furthermore, a second factor strongly compromises imaging spectroscopy on Titan, which is the backscattering by atmospheric aerosols. This brightens up the image and reduces its contrast, leading to a blurring effect. *Sagan and Khare* (1979) showed that scattering aerosols account for the opaque and yellow-orange appearance of Titan in the visible. Indeed, the scattering effect increases in intensity toward the shorter wavelengths, and becomes negligible starting from 3 µm (e.g. *Rodriguez et al.*, 2006; *Doose et al.*, 2016), as shown in Figure 2.6B. Thus, this effect is expected in VIMS data, and particularly through the first atmospheric windows centered at 0.76, 0.83, 0.94, and 1.08 µm, and also through the ISS data at 0.938 µm. Finally, the magnitude of the atmospheric absorption and scattering effects can vary within one individual observation, as a function of the viewing geometries[3] (*Le Mouélic et al.*, 2010, 2012, 2016). In global mosaics of uncorrected VIMS data, many seams appear between individual observations due to the varying viewing angles between data acquired during different Titan flybys. These angles induce significant surface photometric effects and a strongly varying atmospheric contribution. Thus, in order to perform a complete geologic investigation on Titan by extending it to the near-infrared wavelengths, it is mandatory to compensate for the atmospheric contributions. Otherwise, omitting the removal or reduction of such contributions and assuming them in VIMS data is a simplification that could bias the interpretation of the data. That is why diverse techniques of correction were developed and applied on VIMS data to return surface information, such as a semi-empirical approach (*Cornet et al.*, 2012a; *Le Mouélic et al.*, 2012) and a radiative transfer model (*Hirtzig et al.*, 2013; *Solomonidou et al.*, 2014; *Maltagliati et al.*, 2015). These techniques are introduced and described in the next subsections.

2.2.2 SEMI-EMPIRICAL CORRECTION

Thus, to fulfill my objectives, it was essential to correct the infrared data for atmospheric effects. Hence, I have started to use a fast semi-empirical correction to enable the identification and mapping of the spectral infrared units on Titan. This technique consists in removing the additive contribution of the atmosphere from the center of each atmospheric window, by using the wings channels of the window as proxy. Indeed, since the surface cannot be seen

[3] viewing geometries = solar incidence (i), emergence (e) and phase/azimuth (g/ϕ) angles

through these wings, it has been assumed to be representative of the backscattering from all layers of atmospheric haze (*Le Mouélic et al.*, 2012). However, this process is not applied for the last window, since we infer that there is no haze backscattering in the 5 µm-window at the first order, as shown in Figure 2.6B (e.g. *Doose et al.*, 2016). Following the recent analysis of the Huygens' Descent Imager Spectral Radiometer (DISR) in-situ measurements, *Doose et al.* (2016) determined opacity of about 0.1 at 5 µm due to the haze particles, which is negligible. Thus, a simple co-addition of the 14 channels composing the 5 µm-window is used as a correction. For more details about this heuristic technique, the reader is referred to *Cornet et al.* (2012a) and *Le Mouélic et al.* (2012).

Additionally, the sharpness and contrast delivered by the VIMS data can be significantly improved to better depict the surface features on Titan in the infrared (*Le Mouélic et al.*, 2008). During my investigation I have modified the original processing pipeline used and described in *Le Mouélic et al.* (2008) in order to improve the imaging capacities of the observations. For doing that I used a series of common image enhancement techniques such as: (1) co-adding several spectral channels in the center of each atmospheric windows to increase the signal-to-noise ratio of the images; (2) subtracting the co-added wings channels to remove the additive atmospheric effects; (3) dividing the cosine of the incidence angle to normalize the illumination conditions; (4) oversampling the cube by a factor of 3; and finally (5) applying a bilinear interpolation to smooth the pixels. Equation 2.1 describes the first steps of this pipeline, where I_{corr}/F is the empirically corrected radiance factor in a given atmospheric window. A_1 to A_n correspond to the n channels centered in the middle of the given atmospheric window, while B_1 and B_2 are the left and right wings channels of this same window, respectively (Table 2.4). The k factor represents the ratio between the contribution of the whole atmospheric thickness and that of the atmosphere in the wings channels, reported in the last column from Table 2.4. This factor is computed as explained in *Le Mouélic et al.* (2012) to minimize the standard deviation generated by seams in a mosaic composed of multiple cubes acquired with various viewing geometries. After correction of the reflectance, a division by the cosine of the incidence angle ($cos\ i$) is applied to normalize the viewing conditions.

$$\left(\frac{\mathrm{I_{corr}}}{\mathrm{F}}\right) = \left[\frac{\left(\frac{\mathrm{I}}{\mathrm{F}}\right)_{\mathrm{A_1}} + \ldots + \left(\frac{\mathrm{I}}{\mathrm{F}}\right)_{\mathrm{A_n}}}{\mathrm{n}} - \mathrm{k}\,\frac{\left(\frac{\mathrm{I}}{\mathrm{F}}\right)_{\mathrm{B_1}} + \left(\frac{\mathrm{I}}{\mathrm{F}}\right)_{\mathrm{B_2}}}{2}\right](\cos \mathrm{i})^{-1} \tag{2.1}$$

Once VIMS data are empirically corrected and enhanced, we can combine three channels of wavelength bands within Titan's atmospheric windows to produce false-color composites of Titan's surface. By using a color scheme of three single bands, red: average over 4.90-5.12 µm, green: 2.01 µm, and blue: 1.27 µm (in Figure 2.7), it is then possible to distinguish the different spectral infrared units of Titan. However, to emphasize subtle spectral contrasts among them and hence facilitate their identification in the composites, it has been shown that

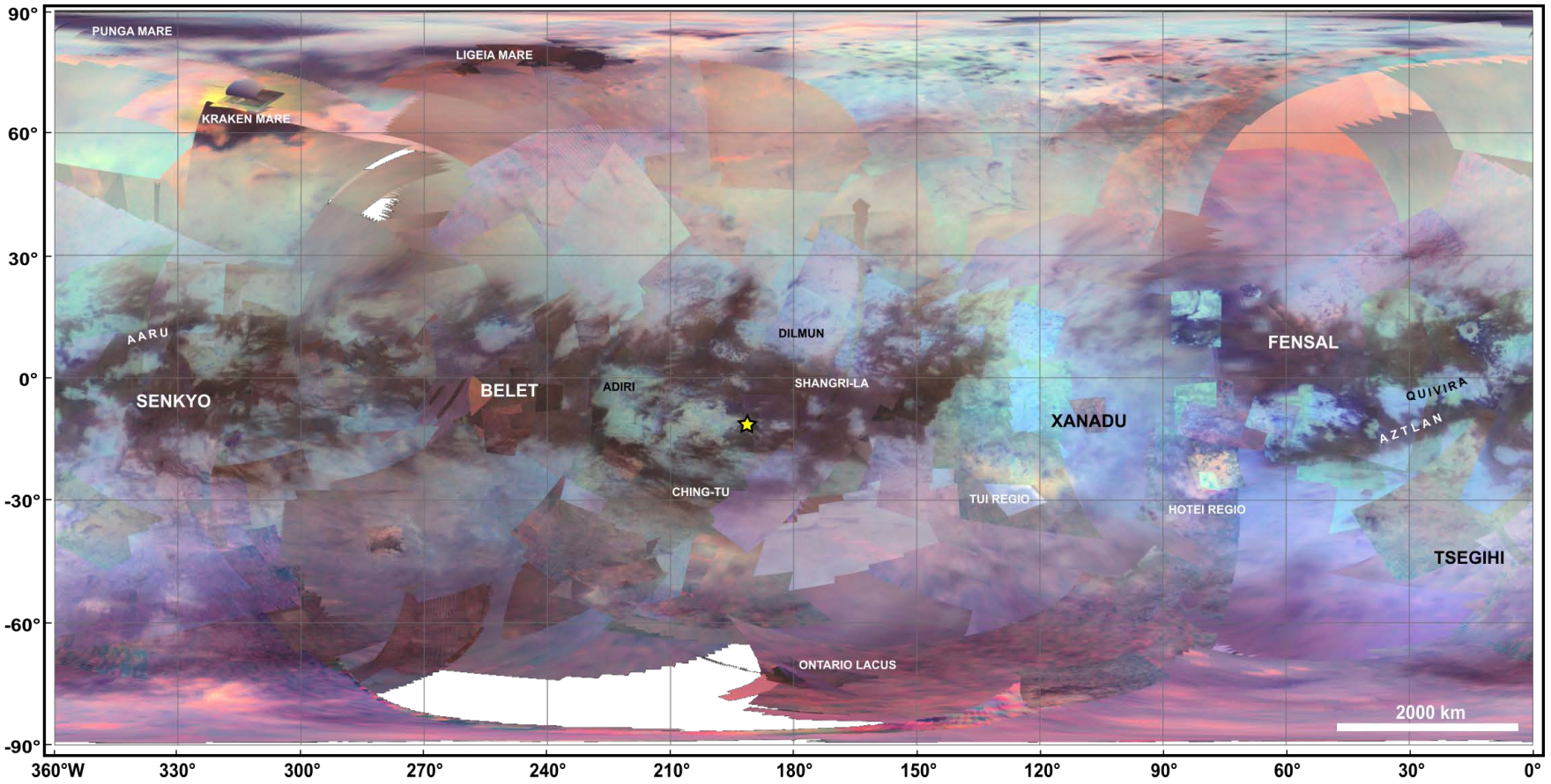

Figure 2.7 – Global map of Titan's surface derived from a mosaic of VIMS infrared data (through November 2015) displayed as a VIMS false-color composite of single bands (red: average over 4.90-5.12 µm, green: 2.01 µm, and blue: 1.27 µm). The map is shown in a simple cylindrical projection centered at 0°N and 180°W, with a scale of about 1.38 km/pixel (*Le Mouélic et al.*, 2016). The yellow star indicates the location of the Huygens landing site.

Table 2.4 – Bands used for the semi-empirical correction (see Equation 2.1).

Atm. windows	Central bands (A_1; ...;A_n)	1st wings (B_1)	2nd wings (B_2)	k factors
1.06	1.047; 1.065; 1.081	1.014	1.113	1.15
1.27	1.261; 1.278; 1.295	1.212	1.343	1.50
1.57	1.556; 1.573; 1.590	1.491	1.655	1.60
2.03	1.985; 2.001; 2.017; 2.034	1.952	2.133	1.29
2.70	2.690	2.646	-	1.14
2.80	2.781	-	2.832	1.14
5.0	4.902; 4.919; ...; 5.106; 5.122	-	-	-

Note: All values are reported in micrometers (µm), except for the k factor (no unit).

the use of band ratios is more efficient than the false-color composites of single bands only (*Le Mouélic et al.*, 2016). Hence during my investigation, I have frequently used false-color composites of band ratios, as follows; red: 1.57/1.27 µm, green: 2.01/1.27 µm, and blue: 1.27/1.08 µm (see Chapter 4). False-color composites of the aforementioned band ratios have been utilized in several studies during the Cassini-Huygens mission (*Barnes et al.*, 2007a; *Jaumann et al.*, 2008; *Le Mouélic et al.*, 2008; *Langhans et al.*, 2012; *Rodriguez et al.*, 2014), as the distinction between the two equatorial infrared dark units, the IR-blue and IR-brown units, becomes more apparent, while the IR-bright unit is still fully consistent with that from the ISS observations.

2.2.3 RADIATIVE TRANSFER MODELING

Through a close collaboration with Sébastien Rodriguez (IPGP) and his team work (Luca Maltagliati and Thomas Cornet) who are involved in the VIMS science team, I was able to retrieve the surface information from the infrared data acquired by VIMS. Thus, with their help, a comprehensive radiative transfer has been applied to the VIMS data of my interest to evaluate the atmospheric contributions (meaning gases absorption and haze scattering) and extract the surface information of the targeted areas. The model was initially developed by *Hirtzig et al.* (2013) and is based on the plane-parallel version of the Spherical Harmonics Discrete Ordinate Method solver (SHDOMPP, *Evans*, 2007). It divides Titan's atmosphere into 70 layers from 700 km altitude to the surface. Most of the inputs feeding the solver are given by in-situ measurements made by the instruments onboard the Huygens probe during its descent through the atmosphere in January 2005. The vertical profiles of the pressure (P), temperature (T), and molar mass are obtained from the Huygens Atmospheric Structure Instrument (HASI) (*Fulchignoni et al.*, 2005). The atmospheric inputs include several gases (CH_4, $^{13}CH_4$, CH_3D, N_2, CO, and C_2H_2) that produce molecular and collision-induced absorptions as well as Rayleigh scattering. Gas abundance vertical profiles were measured by the Huygens/Gas Chromatograph Mass Spectrometer (GCMS) (CH_4 from *Niemann et al.*,

2010), and the Cassini/Composite Infrared Spectrometer (CIRS) (CO from *de Kok et al.*, 2007, C_2H_2 from *Vinatier et al.*, 2010). The optical properties of the aerosols, namely the single-scattering albedo, the opacity, and the phase function are inherited from the Huygens' DISR measurements analysis in the visible and near-IR ranges (*Tomasko et al.*, 2008), and from laboratory experiments (*Khare et al.*, 1984), as well as adjustment to VIMS data (*Hirtzig et al.*, 2013) in the infrared range. However, the DISR data only provide constraint up to 1.6 µm and the aerosols properties inferred at longer wavelengths are therefore an extrapolation of the results. The radiative transfer model assumes a Lambertian surface. This particular scattering behavior of the surface has been locally reported by *Schroeder and Keller* (2008), when analyzing the Huygens' DISR data acquired during the last stages of the module descent. Interestingly, the same behavior seems to apply at broader scale on Titan, since the analysis of the surface photometry in the 5 µm window (the least affected by atmospheric effects), using a global mosaic VIMS data acquired between Ta (October 2004) and T70 (June 2010), revealed a strong correlation between the brightness of the surface at 5 µm and the Lambert cosine factor (*Le Mouélic et al.*, 2012). The reader is referred to *Hirtzig et al.* (2013) and *Solomonidou et al.* (2014) for further explanation and additional references about the radiative transfer modeling. Recently, this model has been used to extract surface and atmospheric information for several Titan surface regions (*Solomonidou et al.*, 2014, 2018), search for temporal surface and haze changes (*Solomonidou et al.*, 2016), and for comparison purposes among various geomorphologic units (*Bonnefoy et al.*, 2016; *Lopes et al.*, 2016).

Although a radiative transfer model is an effective tool to retrieve surface properties, it is generally time-consuming. We therefore do not apply this model to invert directly the VIMS data, as for classical approaches, but we compute and interpolate solutions on a reference Look-Up Table, also noted LUT (*Maltagliati et al.*, 2015). The LUT is produced using the radiative transfer model as a forward model for different values of input and output parameters: the solar incidence, emergence, and phase angles, and two output physical characteristics (haze total opacity and surface albedo). This method can simultaneously retrieve maps of relative opacity of haze with respect to the opacity at the Huygens landing site in January 2005, and surface albedo in the seven atmospheric windows, in a few minutes (for an usual 64×64 cube), in comparison to the several (tens of) days needed with a classical inversion with the full radiative transfer model. Since the model assumes a Lambertian surface, the surface albedo we retrieve is in fact a Lambert surface albedo (noted A_L), corresponding to the hemispheric reflectance of an isotropically scattering surface (*Hapke*, 2012). In order to dispense with the highly variable observation geometries and for the ease of comparison, we then convert the output Lambert surface albedo into single-scattering albedo (noted ω_0), following the *Hapke* (2012) formalism in the case of an isotropic scattering and compacted medium. Finally, the surface single-scattering albedo can be extracted from the VIMS data.

Thus, during my investigation, the inversion combined with the use of a LUT has been

applied to a selection of VIMS data. This allows me to rapidly retrieve the surface albedo of the infrared units seen on Titan and to compare it with that of synthetic mixtures of candidate compounds in order to constrain the surface composition on the moon, as described with more details in the Chapter 4 taking up my research article published at JGR Planets (*Brossier et al.*, 2018). As for the generation of synthetic mixtures, it is explained in the following section.

2.3 COMPOSITIONAL ANALYSIS

Still through my collaboration with Sébastien Rodriguez and his team, I used a spectral mixing model to generate a spectral library for linear binary mixtures of water ice and tholins (*Hapke*, 2012), for comparison purposes. We vary the grain sizes, from 50 nm to 1 mm in diameter, and the mixing ratio, from 0 to 100%, for the two components. Depending on the spatial resolution of the observations utilized for the investigation, linear (also referred as areal) or non-linear mixing can be considered (*Villa et al.*, 2011).

The choice for mixtures of only two-component endmembers seems to be the best compromise between reducing at a reasonable level the modeling complexity and the number of free parameters, and at the same time keeping the best plausible representability of major surface candidates. Using such a mixing model allows to estimate the main contributors to their infrared spectra rather than deriving a precise composition. Another interesting advantage of this method, as the infrared range is very sensitive to granulometry, is to provide also an evaluation of the grain size range for each of the components present in the mixture, which could bring valuable information on the local geology, as soon as their optical constants are known in the desired spectral range and temperatures.

To date, all observation attempts from Earth-based telescopes and Cassini's VIMS to determine Titan's surface major component(s) suggest that the surface is spectrally heterogeneous. The dominant and most plausible candidate is "dirty" water ice, implying that water ice is mixed with complex solid organics whose composition would be close to tholin-like materials, i.e. the laboratory analogues of Titan's photochemical aerosols (*Khare et al.*, 1984), settling from the atmosphere (*Griffith et al.*, 1991, 2003, 2012; *Coustenis et al.*, 1995b, 2001, 2005; *Negrao et al.*, 2006; *McCord et al.*, 2006, 2008; *Rodriguez et al.*, 2006, 2014). As for the water ice, it is thought to be present in the near-surface of Titan, since it primarily forms the first hundred kilometers of the crust (*Sohl et al.*, 1995; *Tobie et al.*, 2005, 2006; *Fortes*, 2012). A few heterogeneities, in particular among the infrared darkest units, have been suggested to be attributed to a local enrichment in droplets of liquid hydrocarbons in order to darken the surface (*Coustenis et al.*, 2005; *Hirtzig et al.*, 2005). Unfortunately, spectra recorded by the Huygens' DISR instrument do not solve the problem, even locally. Apart from a single shallow absorption feature at 1.5 µm, the evidence for pure water ice is rather

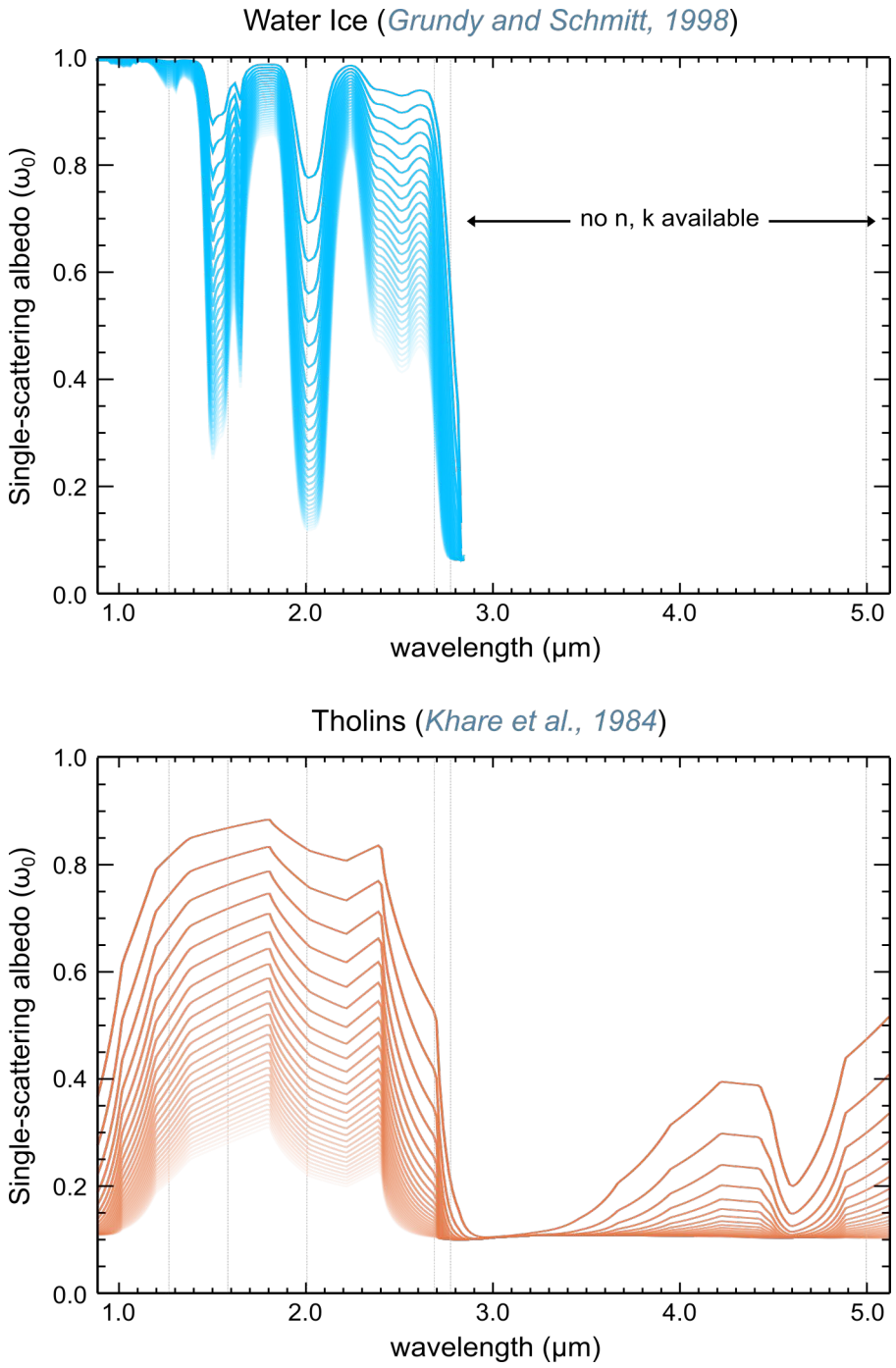

Figure 2.8 – Synthetic spectra of the two most expected compounds on Titan's surface: water ice (*Grundy and Schmitt*, 1998) and tholins (*Khare et al.*, 1984).

inconclusive, as part of the spectra recorded by Huygens is rather consistent with organic material (*Tomasko et al.*, 2005; *Schroeder and Keller*, 2008). Besides, analysis of VIMS spectra, in the infrared atmospheric windows, has completely ruled out the exposure of resolved water ice dominated materials on Titan, at least at a global scale, and has possibly identified some organics at a few places in low albedo areas (*Clark et al.*, 2010). However, *Rannou et al.* (2016) recently tested the hypothesis of the presence of a moist soil at the Huygens landing site, as locally measured by the Huygens/GCMS instrument (*Niemann et al.*, 2010), whose spectrum is successfully explained by a layer of water ice grains covered with aerosol aggregates wetted by liquid methane. Despite a better agreement between the model and the Huygens measurements, the shape of the spectrum is still not fully reproduced.

Thus, I chose to use binary linear mixtures of water ice and laboratory tholins, as shown in Figure 2.8. Synthetic spectra of the single-scattering albedo of both candidates are computed from their optical constants (n, k) inferred at 90 K (*Khare et al.*, 1984; *Grundy and Schmitt*, 1998), by using the Mie theory for grain size equivalents, or smaller than the wavelength and the equivalent slab model formalism developed by *Hapke* (2012) for larger grain sizes. The choice of tholins is both driven by the previous literature and the fact that other potential relevant candidates produced higher in the atmosphere (*Willacy et al.*, 2016; *Krasnopolsky*, 2009, 2014; *Lavvas et al.*, 2008a,b) recombine to form larger molecules at lower altitudes, potentially similar to laboratory tholins. Besides, the optical constants (n, k) of these "simpler" organics are not always available in the literature for the right state, wavelength range and temperatures. Note that optical constants of various tholins exist in the literature depending on the initial gas composition in the experiments (*Cable et al.*, 2012; *Brassé et al.*, 2015), but those determined by *Khare et al.*, 1984 allow to cover the entire VIMS wavelength range at once. The transition between both regimes is determined to occur at (nr-1).X 0.6 both for water ice and tholins, with nr the real part of the refractive index and $X = \pi D/\lambda$ the size parameter (D being the grain diameter and λ the wavelength). The (nr-1).X factor for which we switch between Mie and Hapke theories has been inferred by minimizing the absolute difference (below 0.1%) between single-scattering albedo spectra calculated from the two theories.

In order to test the surface properties retrieval method, hundred test cases are generated from a random combination of tholin/water ice mixing fractions and grain sizes for tholins and water ice, homogeneously scattered in the parameter space. From a given test spectrum we extract the single-scattering albedo in three bands centered in Titan's atmospheric windows: 1.27, 1.57 and 2.10 µm. The best corresponding spectrum in the Look-Up Table (LUT) is determined by using a mean absolute difference (MAD) criterion (imposed to be less than 5%) on these three bands. This gives us access to the grain size and mixing fraction properties of our best match. Using these grain sizes and mixing fraction, the best spectrum matching the test spectrum is also recompute and the global chi square (χ^2) is determine on the entire

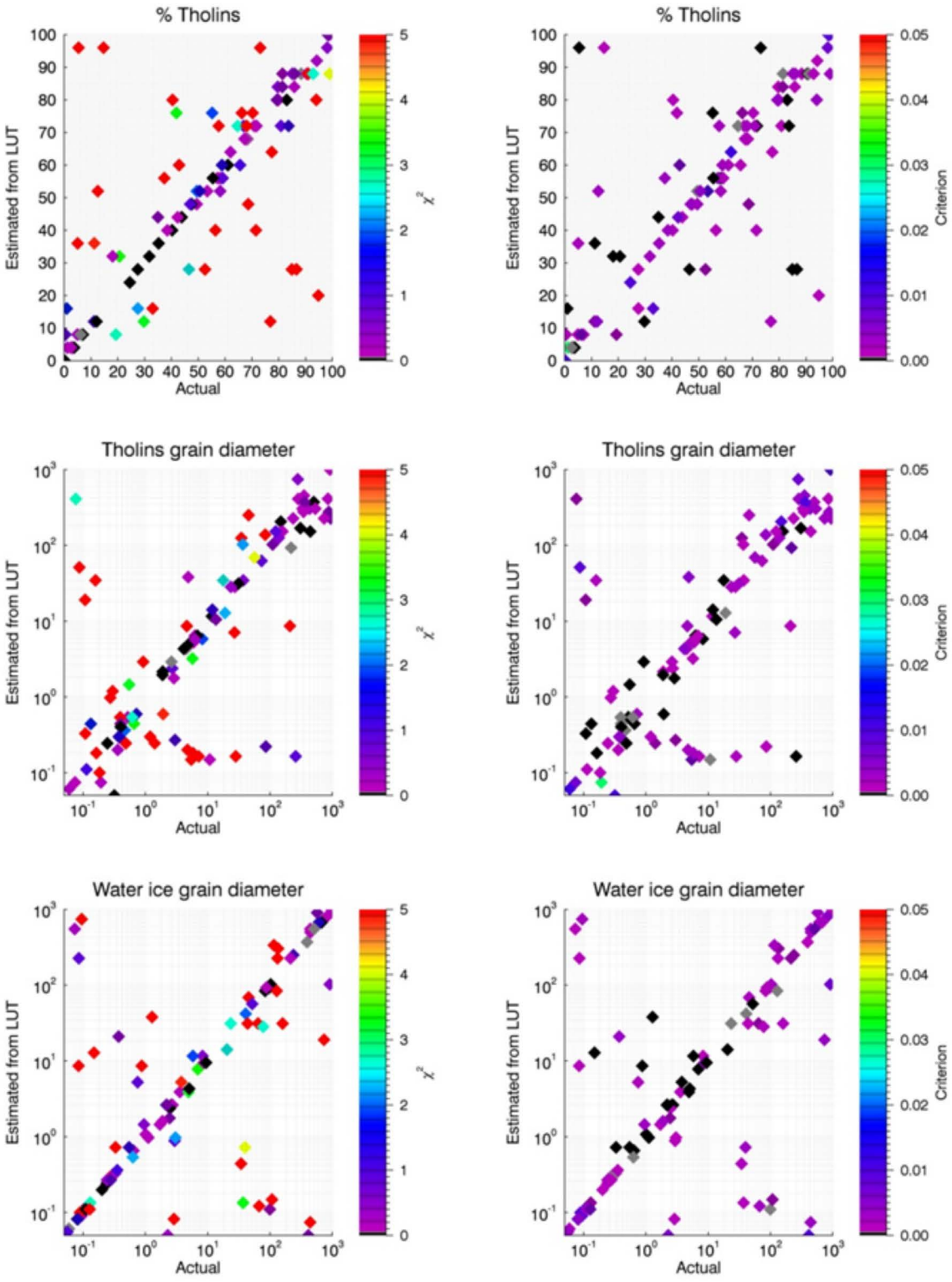

Figure 2.9 – Synthetic tests as correlation plots between the actual and estimated parameters: mixing fractions and grain sizes for water ice and tholins.

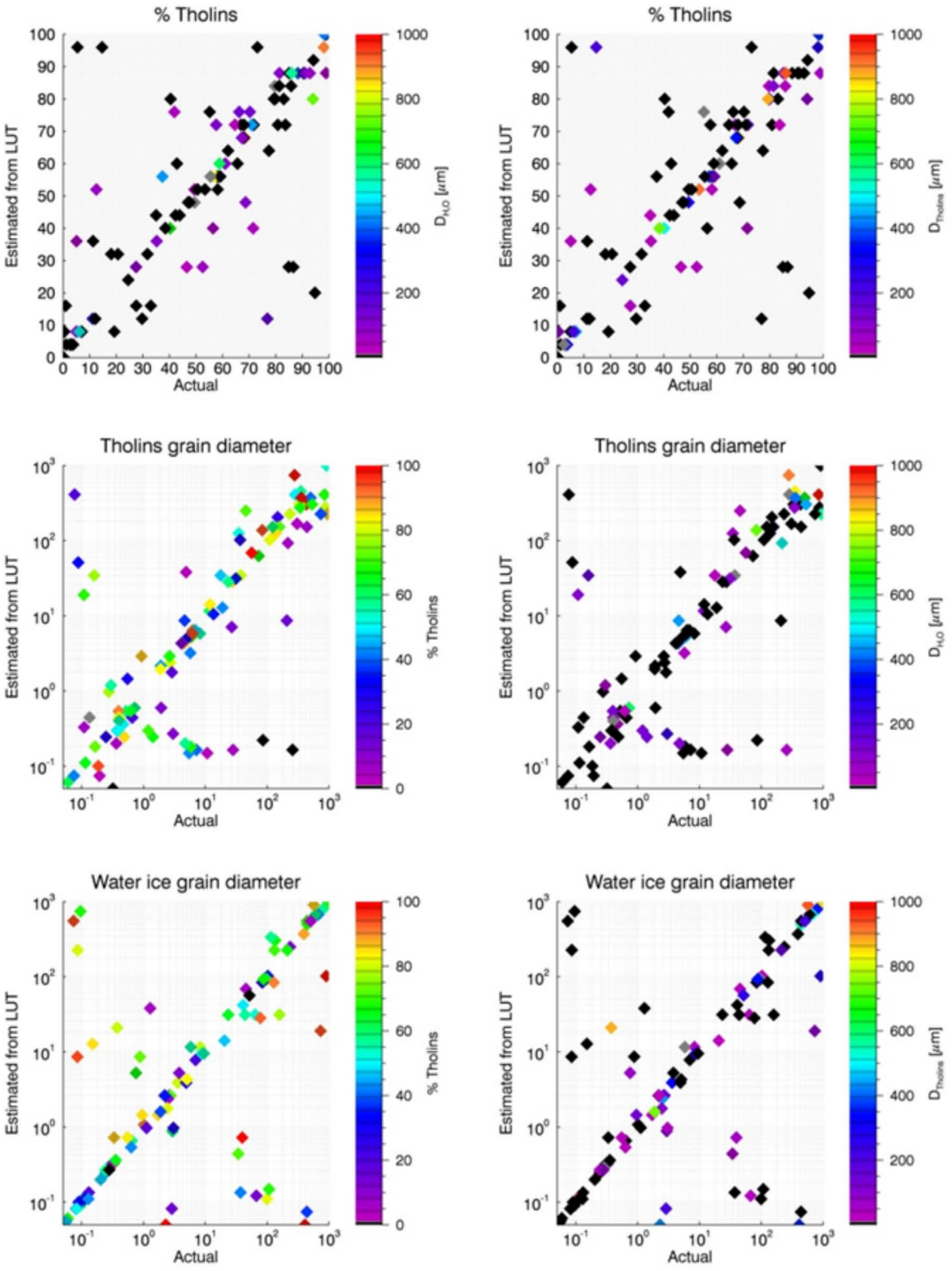

Figure 2.10 – Synthetic tests as correlation plots between the actual and estimated parameters: mixing fractions and grain sizes for water ice and tholins (*continued*).

spectral range (not only on the three bands used for the spectral adjustment).

Figures 2.9 and 2.10 show the results of these synthetic tests as correlation plots between the actual and estimated parameters, with a color coding which corresponds to the χ^2 (Figure 2.9, first column), the mean absolute deviation (Figure 2.9, second column), the values of the two other actual parameters (Figure 2.10). These figures depict some scattering of the solutions due to the small number of bands that can be used to compute our criterion, high χ^2 (> 5) but low MAD. No clear systematics is found for the outliers. However, it should be noted that a great majority of the estimated parameters are in agreement with the actual parameters:

- 58% with $\chi^2 < 1$
- 71% with $\chi^2 < 3$
- 74% with $\chi^2 < 5$

We therefore can expect to have few false positive in our VIMS pixels inversion, although general trends should remain valid.

2.4 SUMMARY

In this chapter, I described the three remote sensing instruments whose datasets were used to survey Titan's surface during the Cassini-Huygens mission. I also introduced the reader to the various techniques employed to integrate the infrared observations from VIMS in order to detect surface features and to evaluate the surface composition of the hazy moon. Before introducing these techniques, I reported the different factors that obstruct Titan's surface at optical wavelengths (gases absorption, haze scattering, and viewing geometries). Gases absorption affects several different wavelength intervals while haze scattering influences more or less the entire spectrum, with a lower magnitude at longer wavelengths. The viewing geometries, for their part, can greatly increase the effect of the two previous factors.

I thus introduced the techniques developed to mitigate these contributions affecting the infrared observations, and particularly VIMS data. I started by presenting the heuristic technique used to correct VIMS data, which was developed by *Cornet et al.* (2012a) and *Le Mouélic et al.* (2012) at LPGNantes. I used this method to enhance the VIMS imaging capacities and to accurately identify the spectral infrared units on Titan's surface. However, this technique was not initially designed to extract the surface information. I have therefore established a collaboration with Sébastien Rodriguez at the IPGP in order to apply an updated radiative transfer code on a number of pre-selected VIMS observations (*Hirtzig et al.*, 2013; *Solomonidou et al.*, 2014; *Maltagliati et al.*, 2015). Based on this cooperation, I was able to extract the surface albedo of the spectral units identified using the empirical

technique. Finally, I concluded this present chapter by discussing about the spectral mixing model employed to complement my compositional analysis, as I intended to compare the surface albedo on Titan with synthetic mixtures of surface candidate compounds. Moreover, I explained our choice of mixtures of only the two most expected components of Titan's surface, meaning the water ice and tholins. Indeed, water ice is thought to mainly form Titan's crust (*Tobie et al.*, 2005), while tholins are photochemically produced in Titan's atmosphere and are supposed to settle on its surface (*Tomasko et al.*, 2008). The results obtained by combining the aforementioned techniques are given and discussed in Chapter 4, taking up the paper published in JGR Planets (*Brossier et al.*, 2018).

Besides the infrared data that required to be corrected for atmospheric contributions, SAR data do not need such treatment, and can be directly utilized after a short processing (projection and conversion to format compatible with GIS). SAR swaths can thus be integrated into a GIS in order to produce an updated global mosaic of Titan's surface at a wavelength of 2.18 cm (Figure 2.5). The mosaic is later used to identify and map the major geomorphologic units present on Titan. The geomorphologic map (Figure 3.1) and the description of the various units are given in the following chapter (see Chapter 3).

Chapter 3

TITAN'S GEOMORPHOLOGY

3.1 GEOMORPHOLOGIC MAPPING

Since RADAR can easily penetrate clouds and organic haze layers without being affected by their effects, the processing of the SAR data does not required any correction. Hence, once SAR swaths were processed and reprojected into a simple cylindrical projection, they were integrated into a Geographic Information System (GIS) software package to evaluate the geology on Titan's surface. Thus, I have mapped the major geomorphologic units present on the moon. Figure 3.1 shows the global distribution of these units. The mapping of the geomorphologic units was mostly based on their structural and topographic differences seen in SAR data, and it was carried out by identifying the units in shapefiles using a GIS. Thus, the shapefiles can be used at any time for further investigations, such as comparison with infrared data in the next chapter (see Chapter 4). I have mainly used a scale of 1:2,000,000 for general mapping, otherwise small scale features were mapped at a scale of about 1:750,000, particularly for the dunes and small lakes.

The geomorphologic units are described in this chapter through an assessment organized with respect to previous studies, such as the initial work described in *Lopes et al.* (2010) and then the detailed mapping of mid-latitudes by *Malaska et al.* (2016a) and of the polar regions by *Birch et al.* (2016a). The units are therefore subdivided into several geological classes, beginning with the cryovolcanic candidates, then mountainous and hummocky terrains, impact craters, plains, dunes, fluvial networks, and ending with the hydrocarbon lakes and seas. Cryovolcanic candidates and fluvial rivers are not included in the map (Figure 3.1), although the mapping of the fluvial networks by *Burr et al.* (2013) can be integrated as shapefiles into a GIS.

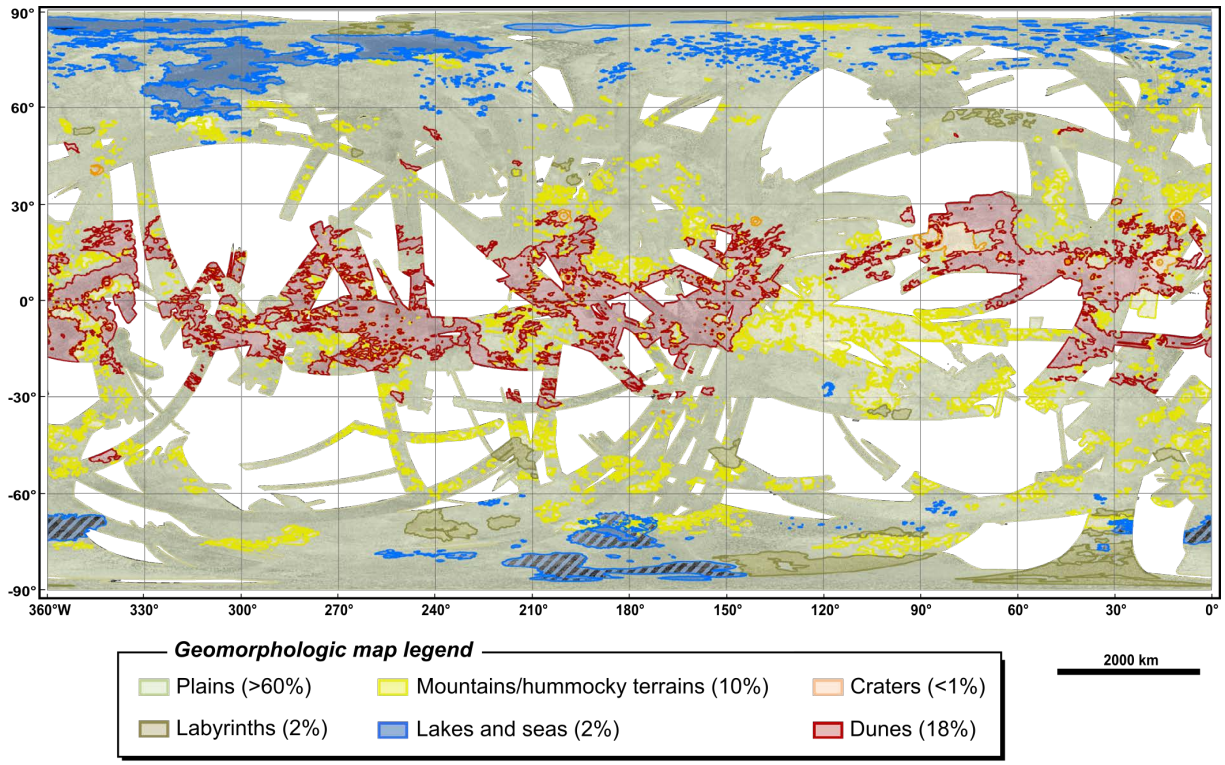

Figure 3.1 – Geomorphologic mapping of the major landscapes on Titan. Percent next to each geomorphologic unit represents their coverage area on Titan's surface in SAR imaging mode.

3.2 GEOMORPHOLOGIC UNITS

3.2.1 CRYOVOLCANIC CANDIDATE(S)

Cryovolcanism is one of the mechanisms suggested as potential sources to resupply Titan's atmosphere with methane (CH_4) (*Tobie et al.*, 2006; *Mitri et al.*, 2008), since the compound is destroyed and converted to heavier hydrocarbons irreversibly on a relatively short timescale of about a few tens of million years (*Atreya*, 2010). Here, cryovolcanism refers to volcanism with low-density, low-melting point materials such as ammonia water hydrates and methane-clathrate hydrates, as explained in *Tobie et al.* (2006) and *Mitri et al.* (2008). Since the beginning of the Cassini-Huygens mission, the RADAR data and particularly the SAR images are used to seek evidence of cryovolcanic activity on Titan, and several surface features have been identified as potentially cryovolcanic in origin, such as *Lopes et al.* (2007a, 2010, 2013) and *Solomonidou et al.* (2013). VIMS observations have also identified features that were originally thought to be cryovolcanic features (*Sotin et al.*, 2005; *Le Corre et al.*, 2009). Nonetheless, since new information, notably topographic data, were obtained throughout the mission, several of these features were reassessed as their interpretation became dubious.

The cryovolcanic candidates are not included in the map shown in Figure 3.1, as they are now classified as not cryovolcanic. However, one unique surface feature remains as the most

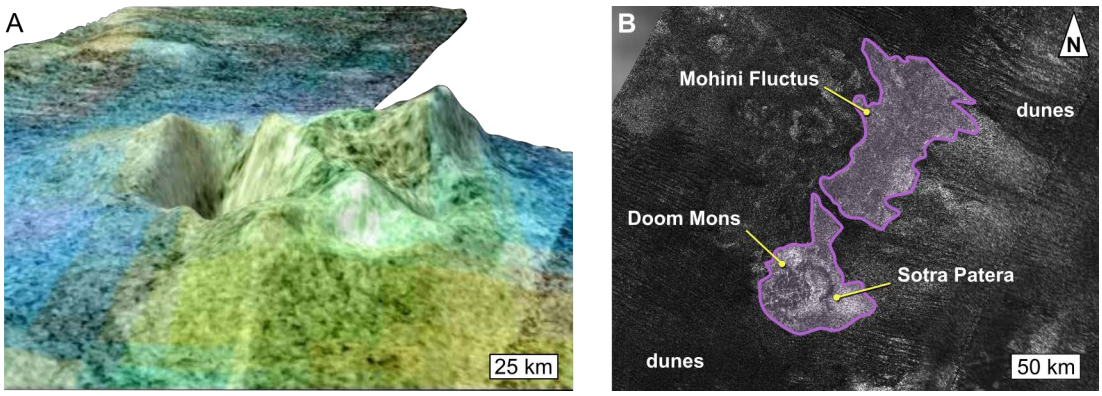

Figure 3.2 – Best candidate yet, Sotra Patera (40°W, 12.5°S, *Lopes et al.*, 2010), as seen (A) in a stereographic view combining SAR and VIMS imagery, where the topography is exaggerated by a factor of 10 (*Kirk et al.*, 2010), and (B) in a SAR mosaic displaying the 180 km-long cryovolcanic flows, named Mohini Fluctus. The volcanic shield/dome (Doom Mons) is 1.5 km-high, while the 30 km-diameter caldera (Sotra Patera) is 1.7 km-deep. SAR swaths were obtained during flybys T25 and T28 (February and April 2007, respectively).

potential cryovolcanic edifice, Sotra Patera (42°W, 15°S) (*Kirk et al.*, 2010; *Lopes et al.*, 2010). Figure 3.2A shows a stereographic view of Sotra Patera, formerly known as Sotra Facula, that consists of a 1,500 m-high peak (Doom Mons) adjacent to a 1,700 m-deep caldera (Sotra Patera), and lobate flows (Mohini Fluctus) extending to over 180 km (*Kirk et al.*, 2010).

3.2.2 MOUNTAINOUS AND HUMMOCKY TERRAINS

SAR swaths reveal evidence of mountainous and hummocky terrains widely distributed all over the surface of the moon (*Radebaugh et al.*, 2007; *Lopes et al.*, 2010; *Malaska et al.*, 2016a). These terrains consist of isolated patches of hummocky material, hills and mountain chains small in areal extent appearing very bright in SAR swaths (Figure 3.3), and hence indicating rough surfaces at RADAR's wavelength ($\lambda = 2.18$ cm). According to radarclinometry, similar to shape-from-shading, these terrains are higher than their surroundings and mostly elevated between 200 and 2,000 m (*Radebaugh et al.*, 2007). Only exception would concerns the region of Mithrim Montes whose highest peak reaches 3,337 m (Figure 3.3C).

Mountainous and hummocky terrains are thought to be the oldest surface units on Titan, although their origin still remains enigmatic. In *Malaska et al.* (2016a), the mountainous and hummocky terrains are considered as ancient crust or icebed, as they may be made of fractured water ice. *Radebaugh et al.* (2007) have suggested several possible formation mechanisms, including compressional tectonism (particularly due to Saturn's tidal forces), extensional tectonism (particularly through Titan's crustal thickening), deposition of impact ejecta blocks or removal of preexisting layers of material by methane rainfalls. In Figure 3.1, the mountainous and hummocky terrains cover about 10% of the surface mapped to date (i.e. 5.7 million km^2), and hence are one of the most widespread units on Titan.

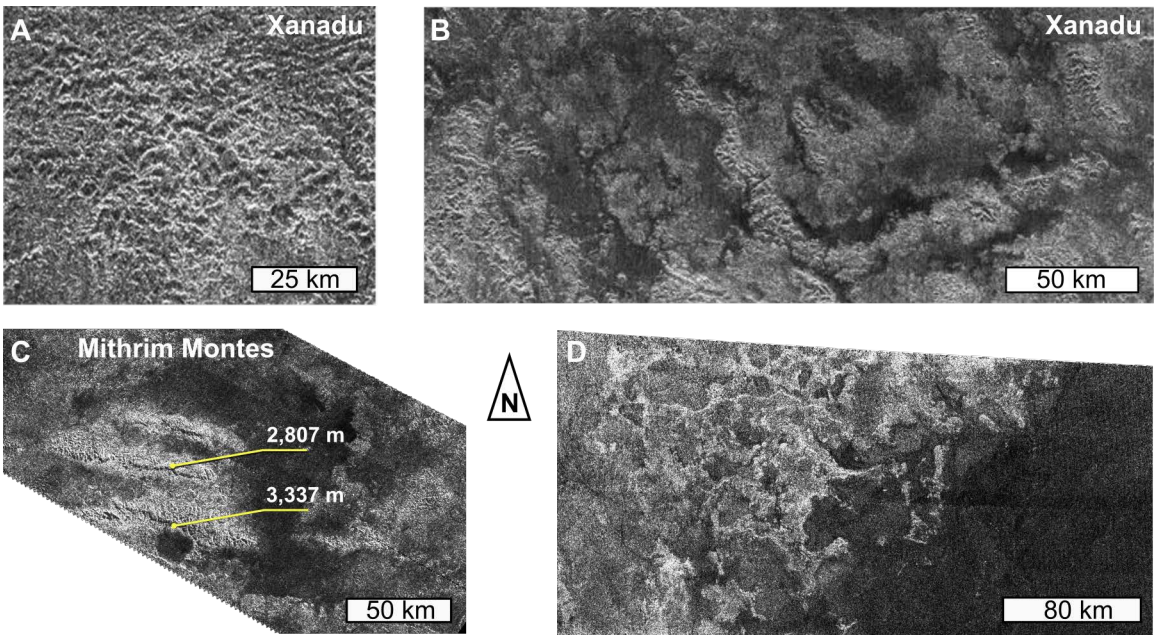

Figure 3.3 – SAR images displaying mountainous terrains: Images (A) and (B) cover the middle area of Xanadu region and were taken during flyby T13 (April 2006). Bright areas represent (A) rugged chains of hills or mountains, while (B) dark broad valleys between these chains of mountains show no topographic features. Dark areas which appear relatively uniform, could be filled with smooth or microwave-absorbing materials. These chains of mountains display also some fractures and rivers (*Radebaugh et al.*, 2011). Image (C) reveals a set of three parallel ridges observed at the northeast Xanadu region during flyby T43 (May 2008). These ridges were later named Mithrim Montes and thought to be the highest mountains on Titan, with 3,337 m and 2,807 m of elevation (Credits: NASA/JPL). Image (D) shows a region located in the southern hemisphere at about 66°S and 356°W and was captured during flyby T7 (September 2005). The rugged areas (SAR-bright) and the smooth area (SAR-dark) appear to be a shoreline. The patterns in the dark area, named Mezzoramia and later Rossak Planitia, indicate that it may once have been flooded, with the liquid having at least partially receded (*Lunine et al.*, 2008).

3.2.3 LABYRINTH TERRAINS

To date, several elevated highly-dissected terrains are identified in mid-to-high latitudes and are defined as labyrinth terrains, such as Sikun Labyrinthus (77°S, 30°W) shown in Figure 3.4 (*Malaska et al.*, 2010). These regions consist of heavily dissected plateaus composed organic materials with intersecting valleys and remnant ridges, and are strongly similar to terrestrial karstic landscapes (*Malaska et al.*, 2010; *Moore et al.*, 2014). Titan's labyrinths are thought to be subjected to chemical dissolution and physical erosion. Hence, surface materials are partially dissolved and dissected into karst-like landscapes, while remaining materials are deposited onto the surrounding plains (*Malaska et al.*, 2014; *Cornet et al.*, 2015; *Malaska et al.*, 2016a). A three-dimensional landscape evolution model (LEM) was recently developed to evaluate the elevation of the labyrinth terrains over millions of years and constrain their degree of maturation (*Cornet et al.*, 2017a).

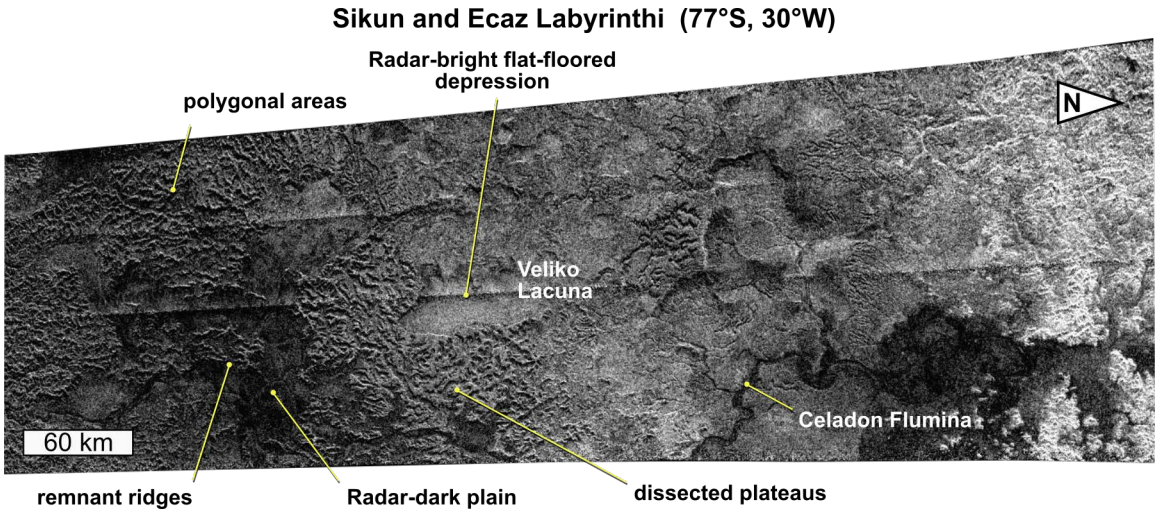

Figure 3.4 – SAR image displaying Sikun Labyrinthus located in the southern polar region (77°S 30°W) which shows evidence of flowing liquids on Titan, from sinuous, wide river channels to shorter, more chaotic drainage patterns (*Malaska et al.*, 2010).

Labyrinth terrains cover less than 2% of the surface probed in SAR imagery (i.e. 0.7 million km^2) in Figure 3.1. During my research, I had the chance to contribute in the nomenclature of a few labyrinth terrains found on Titan. Four of them were already identified and mapped in *Lopes et al.* (2016) and yet unnamed. Considering the ongoing investigations about the labyrinth terrains on Titan, it is crucial to name all the identified terrains as it would be easier to prevent any misunderstandings in future publications or presentations. Hence, I have requested names to the International Astronomical Union (IAU) Working Group for Planetary System Nomenclature (WGPSN) for these four terrains: Salusa (46°N, 264°W), Niushe (75°N, 88°W), Corrin (66°S, 31°W) and Harmonthep (72°S, 101°W) labyrinthi.

3.2.4 PLAINS

Plains are the most extensive terrains seen on Titan's surface covering more than 60% of the surface area mapped by SAR imagery and are commonly found at mid-latitudes (Figure 3.1). Figure 3.5 shows that Titan's plains are relatively homogeneous, mostly featureless and they exhibit a moderate-to-low backscatter in SAR swaths (e.g. *Stofan et al.*, 2006; *Lopes et al.*, 2010). Due to their bland aspect in SAR swaths, they are often referred as 'blandlands' in *Lopes et al.* (2016). Depending on their appearance in SAR swaths, they are subdivided into several types, such as the undifferentiated, mottled, variable, scalloped and streak-like plains (*Lopes et al.*, 2010, 2016; *Moore et al.*, 2014; *Malaska et al.*, 2016a). However, all types of plains units are mapped as one unique unit in Figure 3.1.

Lopes et al. (2016) suggested that plains are younger than mountainous, hummocky and labyrinth terrains, while they are older than dunes, although there is no consistent topographic relationship between units. As for the other considered units, such as impact craters

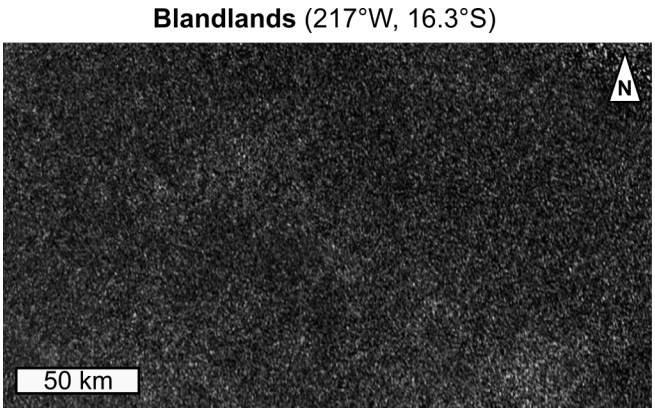

Figure 3.5 – Undifferentiated plains, also referred as "blandlands" in *Lopes et al.* (2016).

and fluvial channels, it has been notified that plains can be found in interiors of craters (*Malaska et al.*, 2016a), whereas channels are seen to dissect plains (*Lopes et al.*, 2010; *Langhans et al.*, 2012). The origin of plains has remained elusive, although different formation mechanisms are proposed in *Lopes et al.* (2016) and *Malaska et al.* (2016a). Plains were originally interpreted to be mainly composed of water ice, with possible contamination by tholins and hydrocarbons (*McCord et al.*, 2006). Nonetheless, later analyses by *Lopes et al.* (2016), suggest that plains have a composition predominantly enriched in organic material instead of ice material, and might derive from sedimentary and depositional processes.

3.2.5 IMPACT CRATERS

A few impact craters have been detected on Titan as shown in Figure 3.6 (*Lorenz et al.*, 2007; *Wood et al.*, 2010; *Neish and Lorenz*, 2012). Titan's craters are mostly seen at low latitudes and present diameters that vary from about 30 to 445 km, with the largest being named Menrva crater. Most of them were assessed in *Wood et al.* (2010) and later in *Neish and Lorenz* (2012). Their morphology varies significantly from one crater to another, depending on their state of degradation by aeolian and fluvial erosion processes. A few "fresh" craters, like Sinlap and Ksa craters, exhibit well-defined rim and blanket ejecta with an existing central peak that show a relatively high SAR backscatter and hence appear bright in SAR swaths (Figure 3.6). In contrast, for older craters, rims and ejecta blankets appear heavily degraded by drainages likely due to fluvial erosion as notified by *Hofgartner et al.* (2016). The crater floors are generally darker and can either be featureless like plains or even be buried by dunes.

The deficit of medium-sized craters (20-100 km in diameter) implies a rapid resurfacing on Titan, as they may have been erased by erosion and burial processes (*Lorenz et al.*, 2007). Although, the atmospheric shielding effects (i.e. ablation and deceleration of projectiles) may account for the paucity of craters smaller than 20 km in diameter (*Engel et al.*, 1995). Recent assessment of impact craters population suggests a crater retention age between 200 Myr and 1 Gyr (*Neish and Lorenz*, 2012). Interestingly, Titan's surface appears to be as

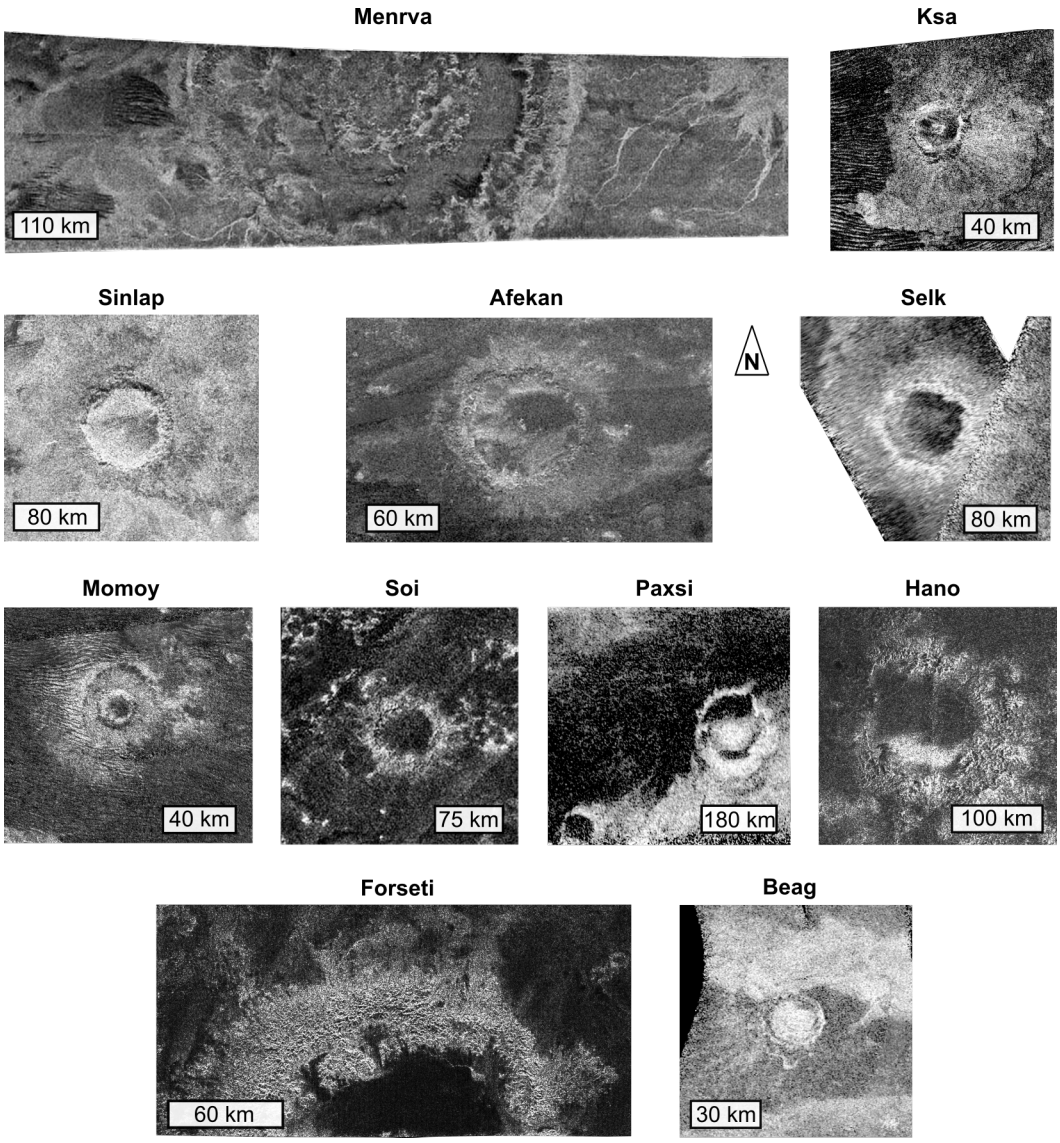

Figure 3.6 – Few impact craters seen in SAR swaths: Menrva (445 km-diameter), Ksa (30 km), Sinlap (80 km), Afekan (115 km), Selk (80 km), Momoy (40 km), Soi (75 km), Paxsi (120 km), Hano (100 km), Forseti (145 km) and Beag (27 km).

youthful in comparison to the early estimation of 100 Myr-1 Gyr obtained by *Lorenz et al.* (2007) based on only three craters identified during the first Titan flybys.

During my investigation, I have included three crater areas as regions of interest: Sinlap (11°N, 16°W), Paxsi (5°N, 341°W) and Menrva (20°N, 87°W) craters. Each area has been studied by superposing SAR and VIMS data, as discussed in Chapter 4.

3.2.6 DUNES

Figure 3.7 shows longitudinal dunes on Titan's surface with very dark appearance in SAR swaths, and seem to lie on a slightly brighter interdune substrate (e.g. *Lorenz et al.*, 2006; *Lunine et al.*, 2008; *Radebaugh et al.*, 2008). Titan's dunes are similar in size and morphology

to linear dunes on Earth, essentially in large sand seas, great sinks of sand located in dry regions like in the Saharan, Arabian, Namibian and Australian deserts (e.g. *Radebaugh et al.*, 2010; *Radebaugh*, 2013). Dunes are covering regions hundreds of kilometers in extent and dominate nearly 18% of Titan's surface mapped by SAR imagery (i.e. 9.5 million km^2) (Figure 3.1). They are essentially found in latitudes below 40° (e.g. *Radebaugh et al.*, 2008; *Lunine and Lorenz*, 2009; *Lopes et al.*, 2010), although some isolated occurrences are seen at higher latitudes (40-60°, *Radebaugh et al.*, 2012; *Paillou et al.*, 2016). Dunes areas often referred as dune fields or even sand seas at a greater extent. Topographic data derived from SAR imaging mode (SARTopo, *Stiles et al.*, 2009) tend to demonstrate that dunes occupy the lowlands (*Le Gall et al.*, 2012). The dune heights were estimated at several occasions and vary from 30 to 200 m (*Lorenz et al.*, 2006; *Barnes et al.*, 2008; *Radebaugh et al.*, 2008; *Neish et al.*, 2010; *Mastrogiuseppe et al.*, 2014). These values are consistent with those of longitudinal sand dunes seen on Earth's deserts. The interdunes width[1] were measured to be comprised between 1 and 4 km (*Barnes et al.*, 2008; *Radebaugh et al.*, 2008; *Le Gall et al.*, 2011; *Ewing et al.*, 2015). Hence, dunes can be locally spaced enough to reveal the exposed dune substrate (*Barnes et al.*, 2008; *Bonnefoy et al.*, 2016). It seems that dune fields form in the regions of relatively low sand supply, and are restricted by topography constraints. In contrast, sand seas are spaced of about 1 km, and often have SAR-dark interdune material, which indicate a higher sand supply in those areas. The dunes in sand seas are very straight for many tens to hundreds of kilometers, and are highly parallel. Dunes reflection around topographic obstacles (i.e. plateaus, inselbergs, and ejecta blanket of impact craters) indicates that sand transport direction is dominantly west to east (*Radebaugh et al.*, 2008). Their confinement, shape and eastward direction of propagation can offer significant information concerning both wind regime and sediment supply (*Lucas et al.*, 2014b).

Furthermore, dunes appear dark in RADAR and ISS observations, and correlate well with the IR-brown units identified in VIMS composites (*Rodriguez et al.*, 2014), as mentioned in earlier studies (*Barnes et al.*, 2007a; *Soderblom et al.*, 2007a; *Jaumann et al.*, 2008). Details about an updated mapping of the infrared units and their correlation with dunes are given in Chapter 4. Dunes are supposedly made of solid organics similar to atmospheric aerosols produced in Titan's atmosphere (*Soderblom et al.*, 2007a; *Rodriguez et al.*, 2014). Dune material is therefore expected to derive from photochemical debris that rained out from the atmosphere, and then deposited and altered by subsequent surficial processes into sand-sized particles suitable for dune formation (*Atreya et al.*, 2006; *Soderblom et al.*, 2007a; *Barnes et al.*, 2015). The theoretical size for sands that would be expected to saltate in Titan conditions is estimated to be around a few hundred microns in diameter (*Lorenz*, 2014; *Burr et al.*, 2015). Nonetheless, the mechanism for growing aerosols or grinding particles to sand-sized sediment that can saltate and form Titan's dunes remains uncertain.

[1]interdune = area between the crest of adjacent longitudinal dunes

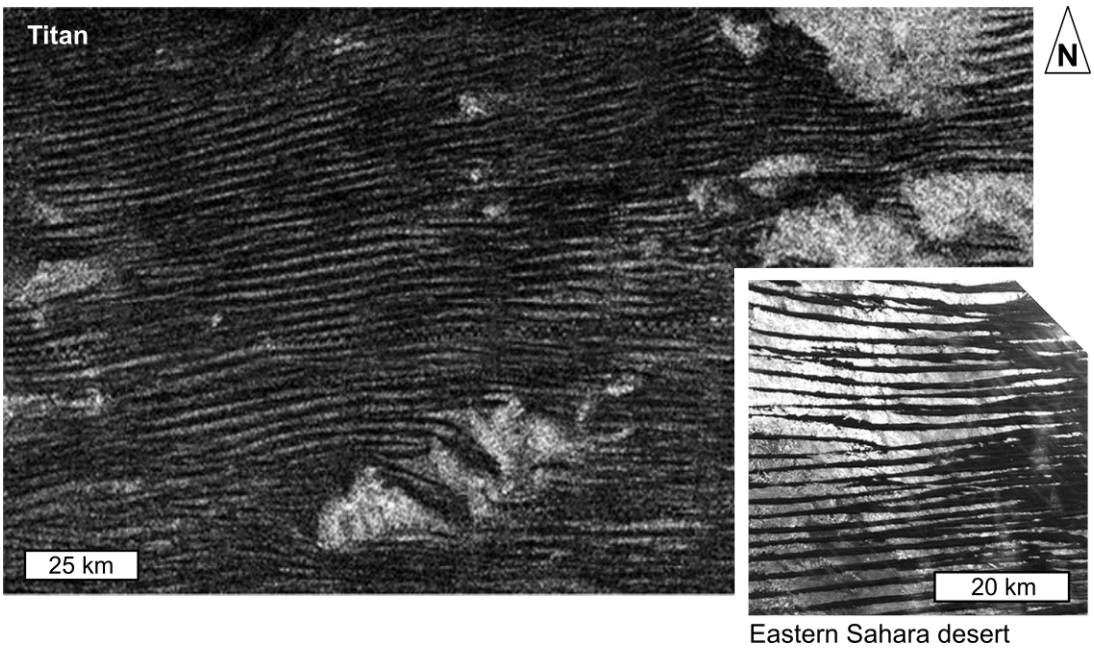

Figure 3.7 – Longitudinal dunes on Titan (from Belet sand-sea, north on top) seen by K-band ($\lambda = 2.18$ cm) SAR from flyby T8 (October 2005), in comparison to terrestrial analogs in Eastern Sahara desert as seen by X-band ($\lambda = 3$ cm) SAR (courtesy of Tom Farr and NASA/JPL). Dunes appear as SAR-dark streaks against a radar-bright and hence rough and/or fractured substrate (*Radebaugh*, 2013).

3.2.7 FLUVIAL NETWORKS

Fluvial networks on Titan have been first identified in DISR images taken by the Huygens probe (*Tomasko et al.*, 2005), and later in SAR swaths from Cassini's RADAR (*Lorenz et al.*, 2008). Figure 3.8A shows pictures of small-scale fluvial features near the equator taken during the descent of the Huygens probe (*Tomasko et al.*, 2005). Figure 3.8B is a picture of Titan's surface acquired after the Huygens probe soft-landing. This picture reveals rounded pebbles between 3 mm (i.e. resolution limit of the imager) and 20 cm in diameter and overlaid by fine sediments, suggesting that the probe landed in a dry riverbed (*Tomasko et al.*, 2005; *Perron et al.*, 2006; *Soderblom et al.*, 2007b).

Fluvial networks are widely distributed on Titan and it is likely that many more fluvial features exist on the moon than those observed but are too small for SAR swaths to resolve, as explained in *Lopes et al.* (2010). Fluvial networks seen in SAR swaths can be several hundreds of kilometers in length and few kilometers in width, and display a great morphologic diversity, such as dendritic, linear, anastomeous and sometimes braided networks (*Langhans et al.*, 2012; *Burr et al.*, 2013). As reported in *Langhans et al.* (2012), dendritic networks are the most prominent valleys on Titan and they resemble those on Earth. They are essentially observed near the north pole (*Stofan et al.*, 2007; *Mitchell et al.*, 2007). However, they also cover large areas at low-latitudes, on a local scale near the Huygens landing site (*Tomasko*

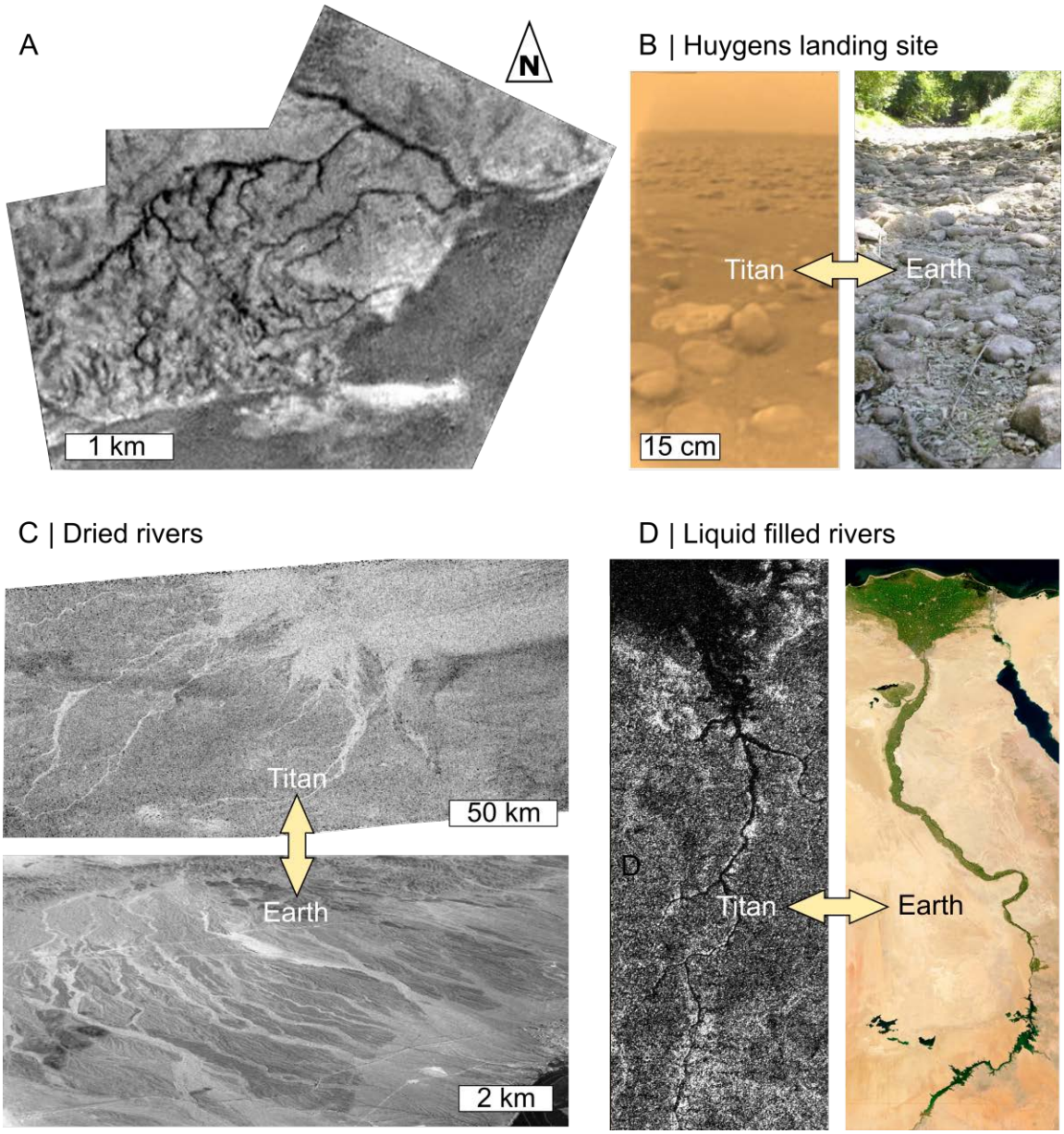

Figure 3.8 – Top row displays fluvial features identified by the DISR imager during the descent of the Huygens probe towards the surface (January 14, 2005), with morphologies of dissected channels in the bright terrains. (A) Panoramic mosaic projected from 6.5 km, showing dendritic valley network at the Huygens landing site. Image centered at 192°W, 10°S (*Tomasko et al.*, 2005; *Langhans et al.*, 2012). (B) First in-situ image of Titan's surface indicating that the probe landed in a dry riverbed like those of the terrestrial rivers, with rounded pebbles and fine sediments (Credits: NASA/JPL-Caltech/Space Science Institute). Bottom row displays Titan fluvial networks compared to terrestrial analogs. (C) SAR-bright fluvial networks near possible alluvial fans in Elivagar Flumina in comparison to analogs in Arizona (*Lorenz et al.*, 2008; *Langhans et al.*, 2012). (D) SAR-dark fluvial networks draining into Ligeia Mare in the northern pole, namely Vid Flumina (about 400 km-long), which is morphologically similar to the Nile river on Earth (about 6,700 km-long) (Credits: NASA/JPL-Caltech/ASI and Jacques DesCloitres/Modis Rapid Response Team/NASA/GFSC).

et al., 2005; *Perron et al.*, 2006; *Soderblom et al.*, 2007b) and on a regional scale within Xanadu province (*Barnes et al.*, 2007b; *Lorenz et al.*, 2008; *Radebaugh et al.*, 2011). In general, dendritic networks consist of channels with widths varying from the resolution limit of the RADAR instrument of 350 m to a few kilometers and lengths up to several hundreds of kilometers (*Langhans et al.*, 2012; *Burr et al.*, 2013). *Langhans et al.* (2012) suggested that such fluvial networks might result from surface runoff after methane rainfalls, as they are found within or close to elevated terrains.

Besides their morphologies, the fluvial networks can also be classified based on their SAR backscatter returned from the SAR imaging mode, as they appear either bright or dark in SAR swaths (*Langhans et al.*, 2012). SAR-bright channels were first essentially found at low latitudes, and might indicate dry riverbeds covered by coarse sediments, such as rounded icy blocks resulting from fluvial processes (*Le Gall et al.*, 2010; *Langhans et al.*, 2012). *Birch et al.* (2016a) report that a great number of SAR-bright channels are also identified in the southern pole, as the high latitudes became more unveiled by the SAR imaging mode. Interestingly, a few SAR-bright areas where channels seem to have disgorged have been identified, such as Leilah Fluctus (80°W 50°N, *Lopes et al.*, 2010) and Elivagar Flumina (77°W 20°N, *Lorenz et al.*, 2008) (Figure 3.8C). Both regions are interpreted as alluvial fans due to their spatial proximity to fluvial valleys and their SAR backscatter, which is very similar to that of the materials within fluvial valleys (*Birch et al.*, 2016b; *Radebaugh et al.*, 2016). Furthermore, Elivagar Flumina depicts braided and anastomeous networks that resemble those in desert washes (also called wadis) on Earth, which indicate torrential runoff events followed by long droughts (*Lorenz et al.*, 2008; *Langhans et al.*, 2012). By contrast, SAR-dark channels are located at higher latitudes and appear to drain into some lakes, and are likewise interpreted to be filled with liquid hydrocarbons after recent precipitation (*Langhans et al.*, 2012). Figure 3.8D shows Vid Flumina, an example of SAR-dark fluvial networks, flowing into the second largest sea on Titan, named Ligeia Mare.

3.2.8 LAKES AND SEAS

Titan is the only planetary body known to support standing bodies of stable liquid on its surface, along with Earth, and such bodies are therefore defined as lakes. The liquid nature of Titan's lakes was confirmed by the specular reflections detected in SAR (*Wye et al.*, 2009) and VIMS (*Stephan et al.*, 2010; *Barnes et al.*, 2011b, 2014) observations. Moreover, *Brown et al.* (2008) and *Soderblom et al.* (2012) argue that VIMS spectra acquired over these lakes is consistent with the presence of ethane and methane in liquid solution with smaller amounts of nitrogen and heavier hydrocarbons. Recent investigations based on RADAR data by *Mastrogiuseppe et al.* (2016a,b) tend to provide similar compositions.

The distribution and classification of the lacustrine features on Titan has been reported

in many studies (*Stofan et al.*, 2007; *Hayes et al.*, 2008; *Aharonson et al.*, 2009; *Birch et al.*, 2016a). They are subdivided by considering their SAR backscatter, as they appear dark, intermediate or even bright in SAR swaths. The three different classes of lacustrine features are described in detail in *Hayes et al.* (2008, 2011). Dark lakes and seas (large enough that they are designated as 'maria' by the IAU) are characterized by their extremely low SAR backscatter indicating a smooth surface or absorbing material at 2.18 cm-wavelength, and are interpreted as being filled with liquid hydrocarbons. Conversely, bright lakes are thought to be lakes that have drained or evaporated and are therefore empty (also noted as lacunae). Empty lakes reside in depressions that are not currently filled with dark materials, but their interior can exhibit different radar properties from their surroundings due to their compositional properties. As for the intermediate lakes, they are inferred as transitional between dark and bright lakes. Furthermore, *Stofan et al.* (2007) observe that such lakes do not entirely fill the depressions in which they lie, and hence suggesting evidence of lakes partly dry and liquid-filled.

Titan's lakes are limited to the polar regions, with latitudes above 50° (*Hayes et al.*, 2008). The northern pole is a region where seas, lakes, and lacunae are the most present. Figure 3.9 is a mosaic of SAR swaths centered in the northern pole with the official names attributed by the IAU. The mosaic displays three large lakes which are identified as seas (*Lopes et al.*, 2007b). In comparison to the northern pole, the southern one reveals a lack in lakes and no seas, as shown in Figure 3.10. Besides the lakes and seas, several areas with relatively low SAR backscattering and without clearly marked topographic contours were first suggested to be flood areas (*Turtle et al.*, 2009, 2011), and are mapped with hatched fill pattern in Figure 3.1. Recent investigations combining imagery and topographic data tend to support that such basins have been formerly filled seas (*Wood et al.*, 2013; *Hayes*, 2016; *Birch et al.*, 2017). Finally, my updated mapping analysis reveals that hydrocarbons liquids are covering more than 9% of the northern polar region (50-90°N) probed by the SAR imaging mode, while it is only 0.3% of the southern one (50-90°S).

3.3 SUMMARY

In this chapter, I introduced the reader the most up-to-date geomorphologic map of Titan at global scale (Figure 3.1) that I have produced at the DLR. Indeed, the map includes the SAR data acquired from Titan flybys Ta (October 2004) to T120 (June 2016). Recent maps published in *Lopes et al.* (2016) and *Malaska et al.* (2016a) are only up to and including SAR data from flybys T92 (July 2013) and T95 (October 2013), respectively. Only exception would concerns the map published by *Birch et al.* (2016a), although their investigation only concerns Titan's polar regions – down to 60° of latitudes. I thus described each of the major landscapes identified on Titan with respect to the extensive literature related to Titan's

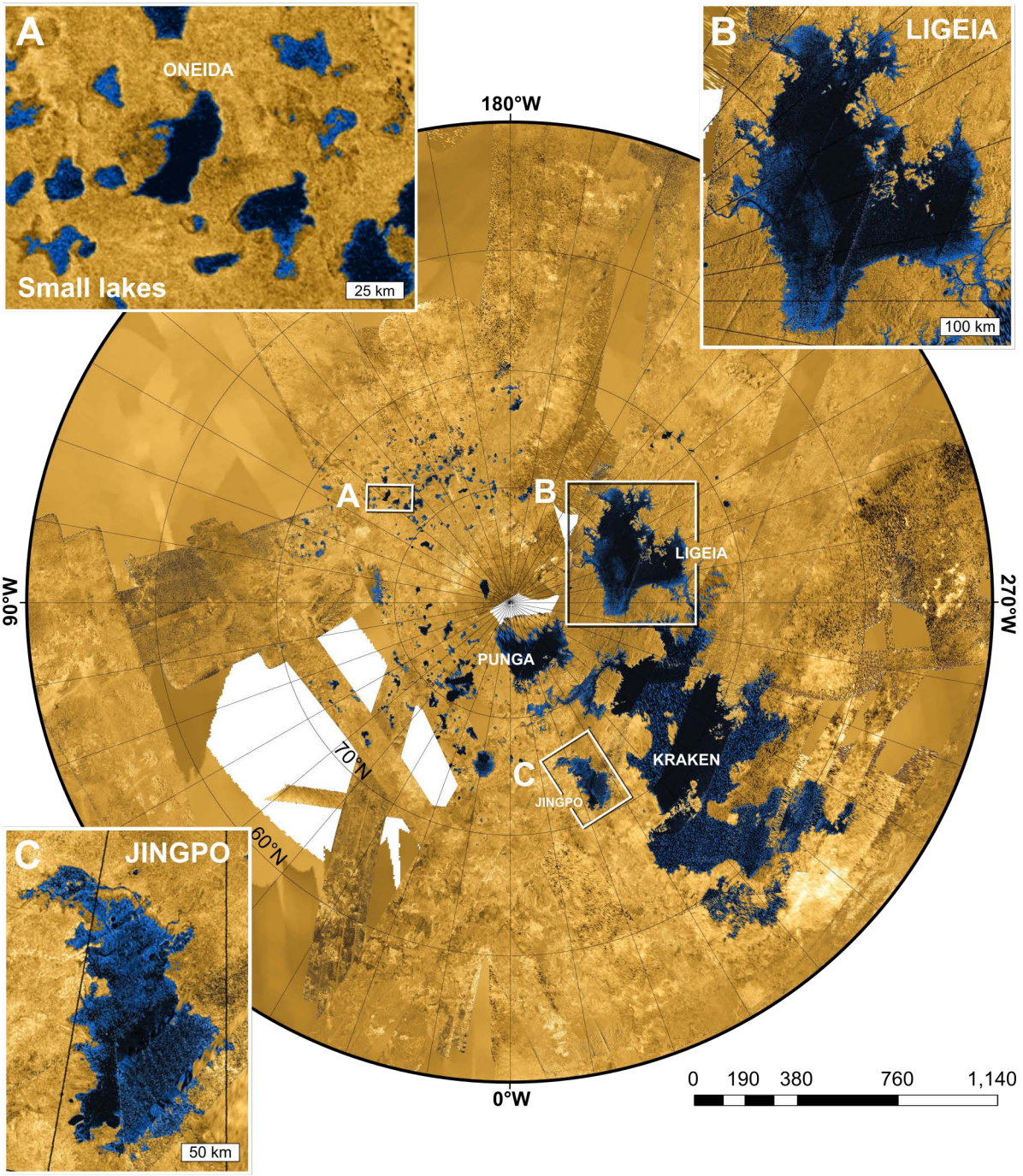

Figure 3.9 – SAR false-color mosaic of Titan's northern polar region 50-90°N, showing hydrocarbon seas, lakes and tributary networks (white areas have not been imaged). The mosaic has been colorized to emphasize the land/liquid contrast in backscatter value: blue coloring indicates low radar reflectivity areas caused by bodies of liquid ethane, methane and dissolved nitrogen. Kraken (68°N, 310°W), Ligeia (80°N, 248°W) and Punga (85°N, 340°W) maria are the three largest lakes on Titan and hence referred as seas. Beside the seas, Jingpo Lacus (73°N, 336°W) is the largest lake of the northern hemisphere. Credits: NASA/JPL-Caltech/ASI/USGS.

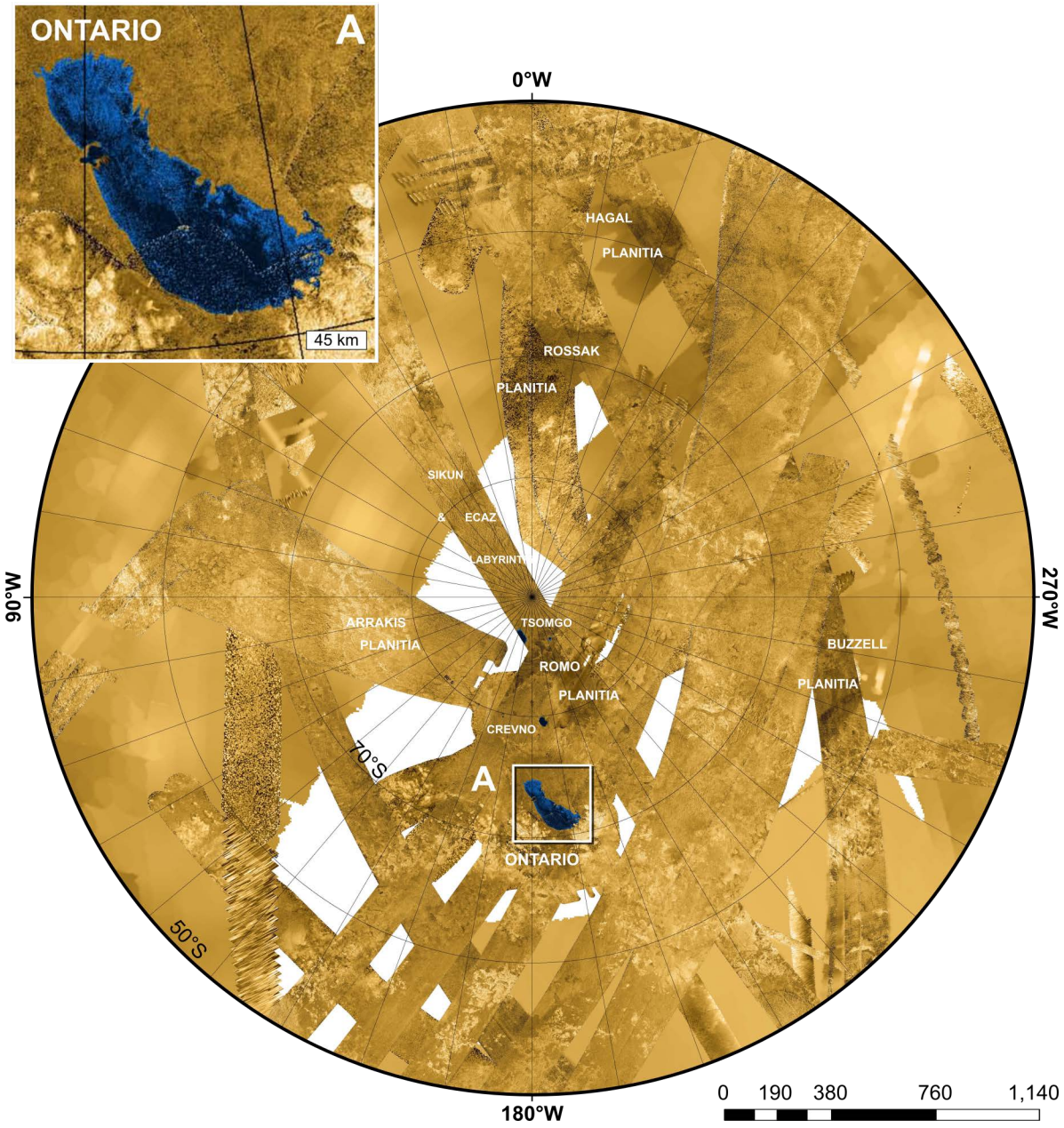

Figure 3.10 – SAR false-color mosaic of Titan's southern polar region 60-90°S (white areas have not been imaged). Ontario Lacus (72°S, 183°W) is the only relevant lake present in the southern polar region, with two smaller lakes named Tsomgo and Crevno lacūs. Rossak (71°S, 5°W), Romo (83°S, 159°W), Hagal (60°S, 345°W) and Buzzel (66°S, 263°W) planitiae are possible former seas. Credits: NASA/JPL-Caltech/ASI/USGS.

geology. This aimed to help the reader to be more familiar with the landscapes of Titan.

By combining the SAR data collected over the Cassini-Huygens mission, I have obtained pertinent hints about the geologic features covering the surface of the moon. In this chapter, I have shown that Titan's surface is morphologically affected by a rich variety of surficial processes that are likewise analogous to those on Earth, including aeolian, pluvial, fluvial, lacustrine, tectonic, impact processes and possible cryovolcanic eruptions and long-term climate cycles. Indeed, Titan shows landscapes resembling those on our planet, such as extensive dunes in dry regions, fluvial networks draining from mountains to lowlands, as well as lakes and seas. As reported in many publications and presentations, the geomorphologic map clearly shows the significant differences in the latitudinal distribution of the various surface units on Titan, especially for the dunes and lakes (e.g. *Stofan et al.*, 2007; *Lopes et al.*, 2010; *Hayes et al.*, 2011). The lakes are mostly concentrated around the high northern and, to a lesser extent, southern latitudes, and are filled with liquid ethane and methane (Figures 3.9 and 3.10). Meanwhile, mid-latitudes (between 30° and 60°) are dominated by the undifferentiated plains (*Lopes et al.*, 2016). Conversely, dunes are mainly found at low latitudes (under 30°), and may be composed of organic solids. Thus, latitude seems to be an important parameter in the distribution of Titan's landscapes. Interestingly, recent work by *Solomonidou et al.* (2018) suspects a latitudinal dependency in surface composition. Thus, to constrain the nature, origin and evolution of the diverse landscapes on Titan, and hence its geologic and climatic environment, it is essential to evaluate not only the morphology, but also the composition and granulometry of the material composing - or coating - the surface features seen on the moon. Hence, this may provide insights on the geologic processes shaping the surface of the moon, as demonstrated in Chapter 4.

Chapter 4

TITAN'S SURFACE COMPOSITION

This chapter reports the results of my compositional analysis, for which VIMS data were corrected for atmospheric effects and the surface information was extracted to be compared with synthetic candidates compounds (water ice and tholins). RADAR's SAR imagery was also utilized to provide information about the landscapes present in Titan's low-latitudes. All this work is now published in JGR Planets (*Brossier et al.*, 2018).

4.1 INTRODUCTION

Since 2004, the Visual and Infrared Mapping Spectrometer (VIMS, *Brown et al.*, 2004) onboard the Cassini orbiter, has observed at full coverage the equatorial belt of Titan (±40° latitude). VIMS false-color composites are produced by using a color scheme of simple channels (red: average over 4.90-5.12 µm, green: 2.01 µm, and blue: 1.27 µm, in Figure 4.1A) or even ratios of channels (red: 1.57/1.27 µm, green: 2.01/1.27 µm, and blue: 1.27/1.08 µm) in the near-infrared range. The analysis of the two types of composites enables the identification of four main spectral units at the lower latitudes (*Barnes et al.*, 2007a; *Soderblom et al.*, 2007a): the IR-bright, IR-brown, IR-blue and 5 µm-bright units. IR-bright units appear to correspond to mountainous terrains, craters (ejecta, rims and central peak), and most plains (notably undifferentiated and variable plains as described in *Lopes et al.*, 2010, 2016; *Malaska et al.*, 2016a), and are assumed to be formed by a layer of organic sediments similar to the atmospheric aerosols coating Titan's substratum. IR-brown units are strongly correlated with the dunes as seen by Cassini's RADAR (*Soderblom et al.*, 2007a; *Rodriguez et al.*, 2014) and are most likely made of organic sand-like particles. IR-blue units are thought to be enriched in water ice with respect to the rest of Titan's surface, and possibly result from icebed material excavated by impacts (*Le Mouélic et al.*, 2008) and fluvial erosion upon this icebed (*Rodriguez et al.*, 2006; *Barnes et al.*, 2007b; *Jaumann et al.*, 2008, 2009). The last spectral unit is very bright at longer VIMS wavelengths, and therefore named 5 µm-bright

units, and is often interpreted as evaporitic deposits related to lacustrine activities (*Barnes et al.*, 2011a; *MacKenzie et al.*, 2014; *MacKenzie and Barnes*, 2016).

This investigation is focused on the compositional and geomorphological relationships between the first three spectral units present in the equatorial regions; meaning the IR-bright, -brown, and -blue units. The latter – the 5 µm-bright units – are not being analyzed in our investigation since they do not appear to take part of the IR-bright-blue-brown contact sequence at the VIMS spatial resolution. The spectral characteristics of the three infrared units identified in the composites describe an apparent transition that is consistent with compositional mixtures that may indicate they are linked by some geologic processes, although their respective composition still remains enigmatic. First, the analysis starts with the identification and mapping of the main terrains present in the equatorial regions by using the near-infrared imaging data from the Cassini orbiter. In addition, the SAR data acquired by the RADAR instrument were used to retrieve the morphological properties of those terrains (see Chapter 3), and look for potential correlation between both SAR features and infrared units. Indeed, the dunes seen in SAR swaths appear to correspond to the IR-brown units (*Soderblom et al.*, 2007a; *Rodriguez et al.*, 2014), while the other considered infrared units (i.e. the IR-bright and -blue units) are linked to several geomorphologic units identified in SAR swaths (e.g. *Soderblom et al.*, 2007a; *Jaumann et al.*, 2008; *Malaska et al.*, 2016a), although they are not uniquely correlated to them. In addition to the geomorphological analysis, here, we constrain the composition of the considered terrains by using an updated radiative transfer model to evaluate atmospheric contributions and then extract spectral information from the surface, as well as a spectral mixing model for comparison with synthetic spectra of mixtures of Titan's surface candidates. For this investigation, we assume that equatorial terrains are mainly composed of water ice and tholin-like solid organics, the two expected major components of Titan's surface. Hence, coupling both the geomorphological and compositional analyses allows us to constrain the nature of the material found in the equatorial belt of Titan, and point out the geologic processes that could control the current distribution of the investigated terrains seen through VIMS and SAR data.

4.2 MAPPING OF THE EQUATORIAL BELT

4.2.1 IR-UNITS (VIMS AND ISS DATA)

Cassini's VIMS acquires hyperspectral images of Titan in 352 contiguous spectral channels from 0.35 to 5.12 µm (*Brown et al.*, 2004). Nevertheless, because of the dense atmosphere of Titan, made of methane and dinitrogen, the surface is only visible in seven narrow atmospheric windows of the near-infrared, while it is completely hidden in the visible. These atmospheric windows are centered at 0.93, 1.08, 1.27, 1.57, 2.01, 2.7-2.8 and 5 µm, where

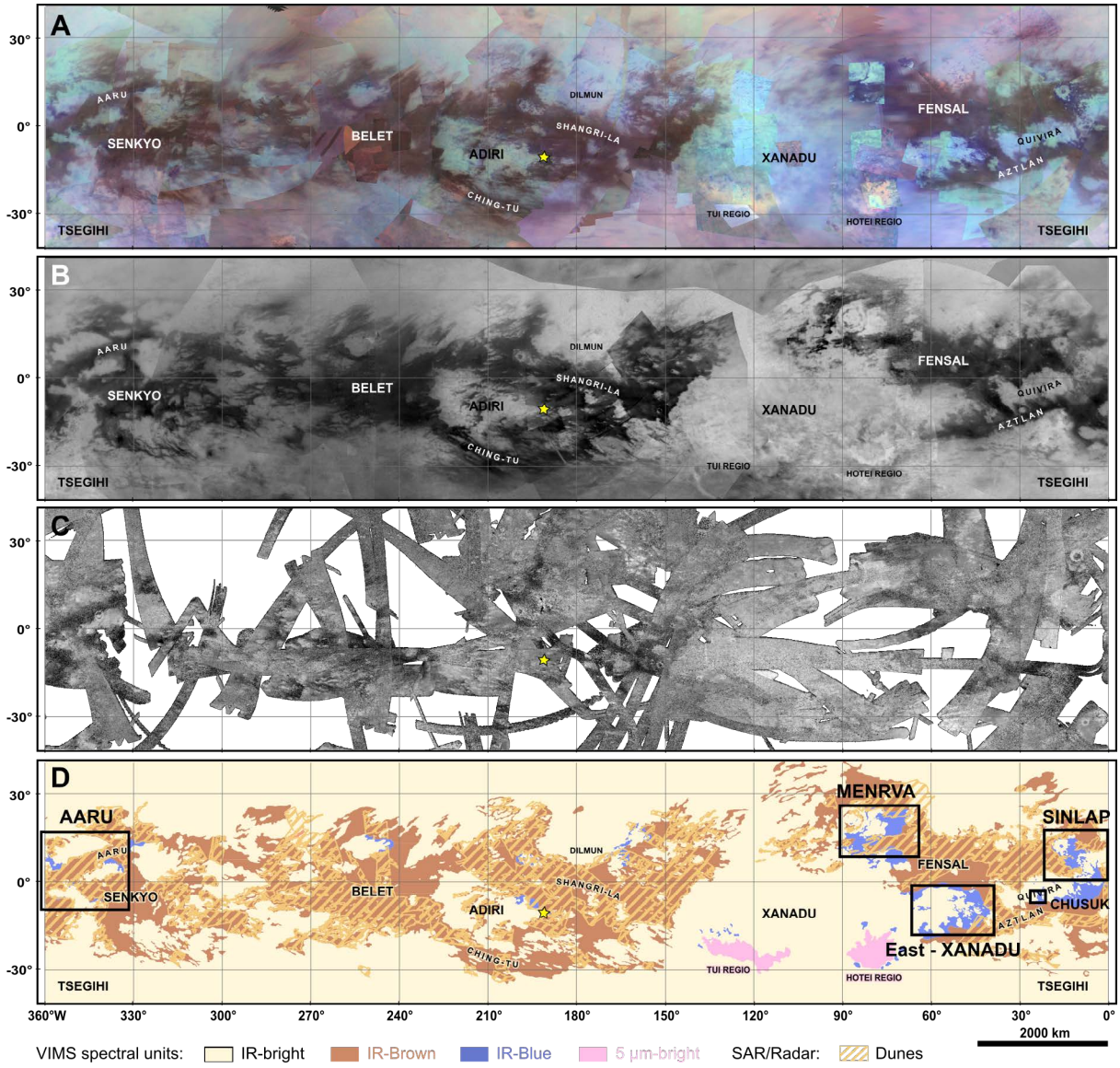

Figure 4.1 – Equatorial maps of Titan within 40° of latitude. (A) False-color composite of simple VIMS channels (red: average over 4.90-5.12 µm, green: 2.01 µm, and blue: 1.27 µm) (*Le Mouélic et al.*, 2016). (B) Near-infrared ISS images at 0.938 µm collected up to flyby T100 in April 2014 (NASA/JPL-Caltech/Space Science Institute, PIA19658). (c) Mosaic of SAR swaths at 2.18 cm through flyby T120 (June 2016) and covering about 65.7% of the total Titan's surface. (d) Color-coded map of the infrared units and the SAR-dunes by using these combined datasets. The IR-brown units cover about 18.6% of the total Titan's surface, while the IR-blue units represent only 1.5%. These maps are displayed in a simple cylindrical projection centered at 180°W and 0°N, with names of prominent surface units. The frames in the last map indicate location of the regions selected for this study: Sinlap crater, Aaru Regio, Menrva crater, Eastern Xanadu, and Chusuk Planitia (see Section 4.3). The yellow star in all the maps indicates the location of the Huygens landing site (192.4°W, 10.2°S).

methane absorption is weaker (*Sotin et al.*, 2005). These windows are still affected by a strong haze scattering, which is greater toward the shorter wavelengths and leads to a blurring effect on the observations (*Tomasko et al.*, 2005; *Rodriguez et al.*, 2006). Different correction methods have been developed and applied to compensate for these effects. In this study, we used two methods (see Chapter 2): a fast semi-empirical correction for infrared units identification and mapping purposes (*Combes et al.*, 1997; *Coustenis et al.*, 2001, 2005; *Cornet et al.*, 2012a; *Le Mouélic et al.*, 2012), and a comprehensive radiative transfer model in order to retrieve more precisely the albedo of the surface units and their composition (*Hirtzig et al.*, 2013; *Solomonidou et al.*, 2014; *Maltagliati et al.*, 2015; *Solomonidou et al.*, 2018).

The semi-empirical correction consists in subtracting the haze scattering additive contribution from the center of each atmospheric window, by using the wings[1] of the window as a proxy for the entire haze atmospheric scattering. Such method was initially employed to improve the visibility of ground features in images acquired by Earth-based telescopes prior the Cassini-Huygens mission (*Combes et al.*, 1997; *Coustenis et al.*, 2001, 2005), and then was adapted for VIMS dataset (*Cornet et al.*, 2012a; *Le Mouélic et al.*, 2012). Note that this heuristic correction is not applied for the 5 µm-window, since there is little to no haze scattering in this window at first order (*Rodriguez et al.*, 2006; *Tomasko et al.*, 2008; *Doose et al.*, 2016). The resulting radiance factor (I/F) in the atmospheric windows provides a good approximation for the surface albedo at these wavelengths. Therefore, the mapping done using a combination of single bands or band ratios chosen within the corrected atmospheric windows allows the enhanced identification and delineation of Titan's major surface spectral heterogeneities, here called spectral units. For more details about this method, the reader is referred to *Cornet et al.* (2012a) and *Le Mouélic et al.* (2012), though main description is given in Chapter 2 (see Section 2.2). Figure 4.1A is a global mosaic of Titan on which the semi-empirical correction has been applied. This newly produced mosaic was oversampled at 0.38 km per pixel for mapping purposes and composed of VIMS data acquired until flyby T114 (November 2015), as described in *Le Mouélic et al.* (2016).

By applying this method to VIMS data and using the color scheme previously described, we were able to accurately identify and map the "purest" spectral units present in the equatorial belt, representing about 64.3% (i.e. 53.6 million km^2) of Titan's surface area. Additionally, a mosaic is produced using data collected by the Imaging Science Subsystem (ISS) at 0.938 µm with a resolution as good as 4 km, up to Titan flyby T100 (April 2014, credit: NASA/JPL-Caltech/Space Science Institute), and is used to support the mapping of the ISS IR-dark units (comprising both VIMS IR-brown and -blue units) (Figure 4.1B). Because of the haze scattering and the fact that ISS probes the surface in a single narrow filter, ISS data do not provide compositional information but clearly reveal the spectral units with high albedo contrast, as seen by VIMS, allowing detailed mapping. The interpretative map of the

[1]wings = wavelengths at which surface is not detected due to absorption by atmospheric gases

equatorial belt, which we used for the selection of our regions of interest (also noted RoIs), is presented in Figure 4.1D.

4.2.2 DUNES (RADAR/SAR DATA)

The mapping of the major geomorphologic units was performed by using SAR swaths from the RADAR (*Elachi et al.*, 2004), as explained in the previous chapter (see Chapter 3) and done in previous studies (*Lopes et al.*, 2010; *Birch et al.*, 2016a; *Lopes et al.*, 2016; *Malaska et al.*, 2016a). In SAR imaging mode (f = 13.78 GHz and λ = 2.18 cm), RADAR probes the surface of Titan directly through the atmosphere and provides the best spatial sampling of the remote sensing instruments onboard the Cassini orbiter, with ground resolutions varying from about 1 kilometer to a few hundred meters when the spacecraft is close to Titan. Figure 4.1C shows the map of the equatorial belt of Titan's surface produced by gathering all the SAR data collected from the first Titan close flyby Ta (October 2004) to T120 (June 2016). SAR data have been reprojected in simple cylindrical coordinate system using the USGS/ISIS3 software (Integrated Software for Imagers and Spectrometers vers. 3) and then integrated into the ArcGIS (ESRI) software package. For further information concerning the characteristics of SAR data and their processing, the reader is first referred to the Chapter 2 and then Appendix A, respectively. At the end of June 2016, 65.6% (i.e. 35.1 million km^2) of Titan's equatorial belt is covered by the SAR mode. SAR data were used to map the dunes present on Titan's surface, the major geomorphologic unit identified in the equatorial belt, which are mainly confined to the low latitudes ($\pm 40^\circ$ N/S). After mapping, we evaluate that the dunes cover about 17.3% of Titan's surface probed in SAR imaging mode and hence 26.8% of the equatorial belt (Figure 4.1D). This corresponds to a dune-covered area of about 9.5 million km^2, which increases the dune areal coverage inferred from firm SAR swaths by about 3 million km^2 (equivalent to 10 Namib deserts on Earth) with respect to previous studies (*Le Gall et al.*, 2011; *Rodriguez et al.*, 2014; *Lopes et al.*, 2016).

4.2.3 UPDATED CORRELATION OF IR-UNITS WITH DUNES

The IR-brown units represent 18.6% (i.e. 15.5 million km^2) of the total surface area of Titan, while the IR-blue units only cover 1.5% (i.e. 1.3 million km^2), corresponding to 28.9% and 2.4% of the equatorial belt, respectively. Figure 4.1D reveals that more than 80% of the mapped dunes correspond to IR-brown units, whereas only 2.2% are found in IR-blue units. The correlation between dunes seen in SAR swaths and VIMS IR-brown unit is thus even higher than reported in *Rodriguez et al.* (2014), further supporting the extrapolation of the dune material surface area to the whole geographic extent of the IR-brown unit. Hence, the dune material coverage is assumed to be extended up to 18.6% (i.e. 15.5 million km^2) of Titan's surface area (in comparison to 17.5% in *Rodriguez et al.*, 2014).

This updated mapping of the equatorial belt enables to highlight the apparent transition from the IR-bright units to the IR-brown units, between which IR-blue units are often observed. Moreover, we demonstrated that it is necessary to compare the spectral units seen in VIMS and ISS infrared observations with the SAR swaths, in order to provide a complete description of our investigated terrains (black frames in Figure 4.1D), with the help of what was done in the previous chapter (see Chapter 3) and in recent studies (e.g. *Lopes et al.*, 2016; *Malaska et al.*, 2016a).

4.3 REGIONS OF INTEREST

The spectral and geomorphologic global mapping of the equatorial regions presented above allows us to identify regions where IR-bright, IR-brown and IR-blue units are in contact. We study several such areas: Sinlap crater (16°W, 11°N), Aaru Regio (350°W, 5°N), Menrva crater (87°W, 20°N), Eastern Xanadu province (55°W, 10°S), and Chusuk Planitia (23°W, 4.5°S). The locations of these regions are indicated in Figure 4.1D, while Table 4.1 reports their VIMS and RADAR acquisition conditions.

4.3.1 SINLAP CRATER

Sinlap is a relatively fresh crater with a diameter of about 80 km, centered at 16°W and 11°N. At a regional-scale, Sinlap crater was observed by VIMS during flyby T13 in April 2006 with a spatial sampling of about 14 km (cube CM_1525118253, in Figure 4.2A with red: 1.57/1.27 μm, green: 2.01/1.27 μm, and blue: 1.27/1.08 μm). These images show that the whole crater area is surrounded by the Fensal sand sea, as seen in green in the semi-empirically corrected VIMS false-color band ratio composites (Figures 4.2A and 4.2B). For consistency with previous studies, the green areas in Figures 4.2A and 4.2B is referred to the IR-brown dune areas (color initially found in the false-color composites of uncorrected VIMS bands and band ratios in numerous publications). The crater floor appears to be filled by IR-blue materials and is surrounded by a ring of IR-bright materials corresponding to the main ejecta blanket, Bazaruto Facula. A large halo with a low albedo and a blue appearance in the false-color composites, is oriented southeastwards and is encircling the IR-bright ejecta blanket. In *Le Mouélic et al.* (2008), this IR-blue plume-shaped, and dune free area, is suggested to be a sheet of icy deposits originated by a water vapor plume produced during the impact. Moreover, *Solomonidou et al.* (2014) applied the Principal Component Analysis (PCA) technique to calculate color units that each correspond to a unique spectral signature in the same VIMS cube as in *Soderblom et al.* (2007a) and *Le Mouélic et al.* (2008), and obtained the same results of three distinct regions.

Table 4.1 – VIMS cube observations and RADAR/SAR swaths used for this investigation.

Dataset/ Flyby	PDS label	Date	Incidence (°)	Emission (°)	Phase (°)	Altitude (km)	Spatial sampling (km/pixel)	Exposure time (ms)
Sinlap crater								
VIMS T13	CM_1525118253	April 2006	30 - 47	0 - 20	40 - 42	26,790	14	68
VIMS T105	CM_1790056808	Sept. 2014	20 - 24	20 - 48	35 - 59	3057	1.5	160
VIMS T109	CM_1802454074	Feb. 2015	25 - 31	0 - 32	21 - 29	3158	1.6	220
VIMS T110	CM_1805209469	Mar. 2015	23 - 30	18 - 27	35 - 37	6222	3.1	70
SAR T3	BIBQI22N068_D045_T003S01	Feb. 2005	4 - 30	-	-	1579	0.3	-
Aaru Regio								
VIMS T61	CM_1629905033	Aug. 2009	9 - 40	8 - 47	11 - 13	27,588	13.8	80
VIMS T109	CM_1802450543	Feb. 2015	9 - 30	18 - 49	41 - 44	24,248	12.1	90
SAR T23	BIBQI26N009_D111_T023S01	Jan. 2007	9 - 38	-	-	1000	0.3	-
SAR T104	BIBQG03S348_D261_T104S02	Aug. 2014	41 - 75	-	-	964	1.5	-
SAR T108	BIBQG01N352_D265_T108S02	Jan. 2015	10 - 60	-	-	970	1.5	-
Menrva crater								
VIMS T114	CM_1826075655	Nov. 2015	7 - 71	2 - 87	28 - 30	62,378	34	320
	CM_1826086162		36 - 52	21 - 38	56 - 64	15,177	7.6	140
SAR T3	BIBQI22N068_D045_T003S01	Feb. 2005	4 - 30	-	-	1579	0.3	-
SAR T77	BIBQI10N064_D229_T077S01	Jun. 2011	8 - 32	-	-	1359	0.3	-
	BIBQG11N071_D229_T077S03		39 - 71	-	-	1359	1.5	-
Eastern Xanadu								
VIMS T9	CM_1514313117	Dec. 2005	2 - 21	1 - 27	21 - 28	17,532	8.7	160
	CM_1514315913		14 - 26	34 - 58	59 - 70	11,182	5.6	80
VIMS T114	CM_1826082135	Nov. 2015	28 - 55	0 - 24	33 - 36	32,165	16	280
	CM_1826085255		38 - 53	10 - 17	46 - 52	18,143	9	280
SAR T113	BIBQI10S066_D271_T113S01	Sep. 2015	5 - 64	-	-	1036	0.3	-
Chusuk Planitia								
VIMS T20	CM_1540485266	Oct. 2006	13 - 15	2 - 41	10 - 44	1321	0.6	80

Note: In SAR imaging mode, the source of illumination is the antenna itself (incidence and emission angles are the same). Altitude refers to the altitude at the closest approach during the Cassini flyby. Note that there is no SAR swaths crossing Chusuk Planitia.

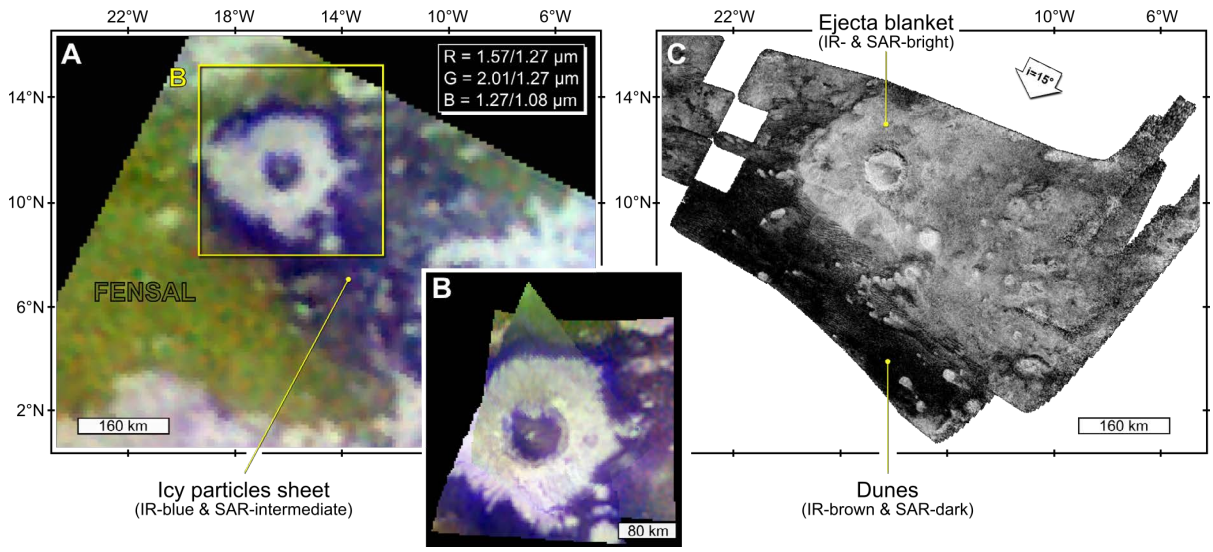

Figure 4.2 – Sinlap crater and its surroundings (16°W, 11°N). (A) VIMS false-color composite of band ratios from flyby T13 (April 2006). (B) Mosaic of the three VIMS observations from flybys T105 (September 2014), T109 (February 2015), and T110 (March 2015) (red: 1.57/1.27 µm, green: 2.01/1.27 µm, and blue: 1.27/1.08 µm). (C) SAR image from flyby T3 (February 2005) targeting Sinlap crater (same scale as (A)) with a spatial sampling of 170 m/pixel. The VIMS observations are oversampled with a scale of about (A) 6 km/pixel and (B) 1 km/pixel, and are empirically corrected from atmospheric effects. All images are displayed in simple cylindrical projection, and north is up. The white arrow on (C) indicates the RADAR illumination.

Figure 4.2B is a projected mosaic of three more recent VIMS high resolution observations displayed with the same color scheme as in Figure 4.2A. The first observation was taken during the flyby T105 in September 2014 with a spatial sampling of about 1.5 km (cube CM_1790056808). The second observation was recorded during the flyby T109 in February 2015 with a spatial sampling of about 1.6 km (cube CM_1802454074). The last observation used for this mosaic was taken one month later during the flyby T110 (March 2015), with a spatial sampling of about 3.1 km (cube CM_1805209469). The first observation, from flyby T105, was analyzed in *Neish et al.* (2015) to provide further morphological details about Sinlap's region at local-scale, while the two other observations (T109 and T110) have not been studied and published so far. This mosaic (Figure 4.2B) reveals a degraded central peak, which is as bright as the main ejecta blanket of the crater. Numerous dark linear features are seen embedded in the ejecta blanket that can be interpreted as channels (*Neish et al.*, 2015), but some of them seen in the southern part of the blanket could even be post-impact fractures since they clearly appear alongside the crater flanks (not radially) in both VIMS and SAR images. Additionally, there is evidence of IR-brown sand material within the crater floor that is spectrally similar to that of the dunes, although no dunes are seen. As shown in Figure 4.2C, Sinlap crater and its surroundings have been observed by the RADAR in SAR imaging mode during the flyby T3 (February 2005), with a resolution reaching a few hundreds of meters, clearly revealing dunes, as long dark linear streaks, within the surrounding sand

sea. While a clear difference appears between the IR-bright and IR-blue units in the VIMS false-color composites, these regional infrared differences are not seen in the SAR swaths, which may imply that the IR-blue unit in this area is quite superficial.

4.3.2 AARU REGIO

Aaru is a large region with mixed low and intermediate albedo confined at 5°S to 15°N, and 330-360°W, which can be considered as an extension of the Senkyo sand sea. VIMS acquired observations of this region at medium-scale (around 13.8 km) during the flyby T61 (August 2009, in Figure 4.3A). Aaru Regio is essentially seen in the VIMS observation cube labeled CM_1629905033 (*Buratti et al.*, 2012). A second observation, unpublished yet, was acquired later during flyby T109 (February 2015) with a higher spatial sampling at 12.1 km/pixel (cube CM_1802450543). Moreover, SAR swaths are crossing the region at high- and medium-resolutions (0.3-1.5 km), with images collected during flybys T23 (January 2007), T104 (August 2014), and T108 (January 2015) (Figure 4.3B). The northwestern area of Aaru Regio is surrounded by IR-bright units that are locally bright in the SAR swaths, which implies a rough surface at the RADAR wavelength, such as Handir Colles (356.7°W, 10°N, in Figure 4.3C). Furthermore, some areas appear blue in the VIMS false-color composite. They are devoid of dunes, featureless, and display an intermediate brightness in SAR swaths, which is likely to be due to a greater roughness and volume scattering than surrounding terrains. One of these IR-blue areas seems to be enclosed between IR-bright units and IR-brown dune areas, such as the Giedi Planitia located at 358°W, 7°N (Figure 4.3D). Figure 4.3E shows that the region is hosting a 120 km-diameter impact crater, named Paxsi (341.2°W, 5°N), with strongly breached rims and a central pit. Paxsi's rims are degraded enough to let the dunes fill in, as notified in *Buratti et al.* (2012) and *Hofgartner et al.* (2016). We cannot assess the presence of channels at the resolution of the observations.

4.3.3 MENRVA CRATER

The third region investigated in this study is centered on Menrva crater (87°W, 20°N), the largest impact crater on Titan with a diameter of about 400 km. VIMS acquired the best spatially resolved observations of this region during flyby T114 (November 2015). Those new observations were registered at both relatively low (about 34 km, Figure 4.4A) and moderate (about 7.6 km, Figure 4.4C) spatial sampling. Figure 4.4B is a mosaic of SAR swaths crossing the region, with a close up in Figure 4.4D. While the SAR swath from flyby T3 (February 2005) was crossing a small part of the crater, the images from flyby T77 (June 2011) almost cover the whole region. This large crater is a heavily eroded, double-ringed impact basin, as described in *Wood et al.* (2010) and *Williams et al.* (2011). Numerous SAR-bright channels start near the rim crest and flow eastward away from the crater, crossing the ejecta blanket

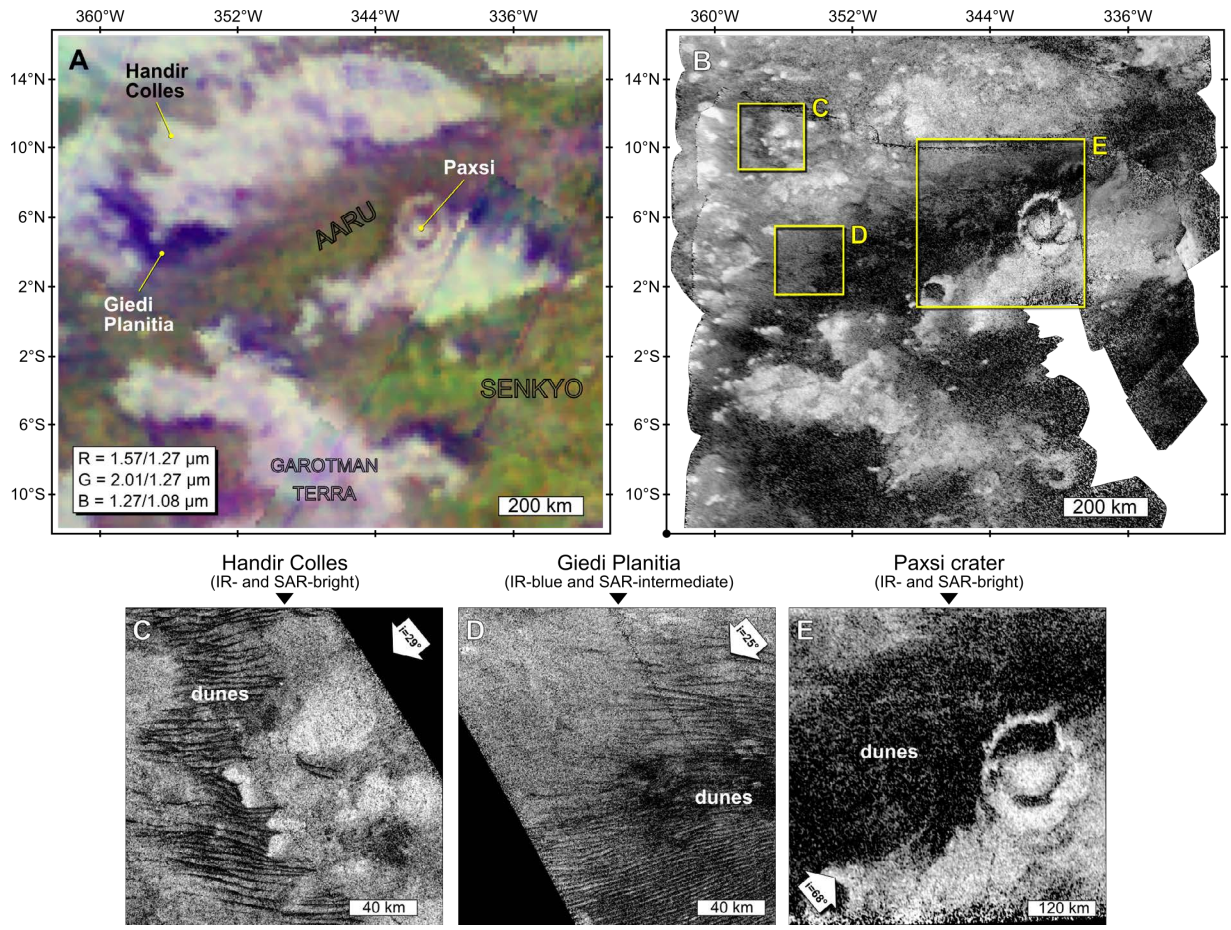

Figure 4.3 – Aaru Regio (350°W, 5°N). (A) VIMS false-color composite of band ratios from T61 (red: 1.57/1.27 µm, green: 2.01/1.27 µm, and blue: 1.27/1.08 µm), taken in August 2009. This VIMS composite is oversampled at 10 km/pixel and is empirically corrected from atmospheric effects. (B) Combined SAR images from flybys T104 and T108 at $\lambda = 2.18$ cm, taken in August 2014 and January 2015 respectively (700 m/pixel). Images (A) and (B) are displayed at the same scale. (C) Closer up on Handir Colles, an IR-and SAR-bright area as mountainous-like terrains. (D) IR-blue and SAR-intermediate Giedi Planitia as a dune-free area. (E) IR- and SAR-bright Paxsi crater, as well as the IR-brown and SAR-dark dunes. Paxsi crater (120 km diameter) displays breached rims and dunes filling in. Images (C) and (D) are derived from SAR images taken during flyby T23 (January 2007, at 170 m/pixel), while image (E) was acquired during flyby T108 (January 2015), at 700 m/pixel. All images are displayed in a simple cylindrical projection, and north is up. The white arrows on (C), (D) and (E) indicate the RADAR illumination.

and a large SAR-bright area of probable deposited material, named Elivagar Flumina (top right corner in Figure 4.4E). The channels all end up in a large fan-like area, one of the SAR-brightest areas of the region, as bright as the channels themselves, and are referred as an alluvial or fluvial fan (*Birch et al.*, 2016b; *Radebaugh et al.*, 2016). This fan-like area is strongly correlated with the IR-blue unit seen in the VIMS false-color composite in Figure 4.4C and also discussed in *Radebaugh et al.* (2016). The inner ring within Menrva crater shows SAR-bright knobs that are also bright in the near-IR data. The floor between the

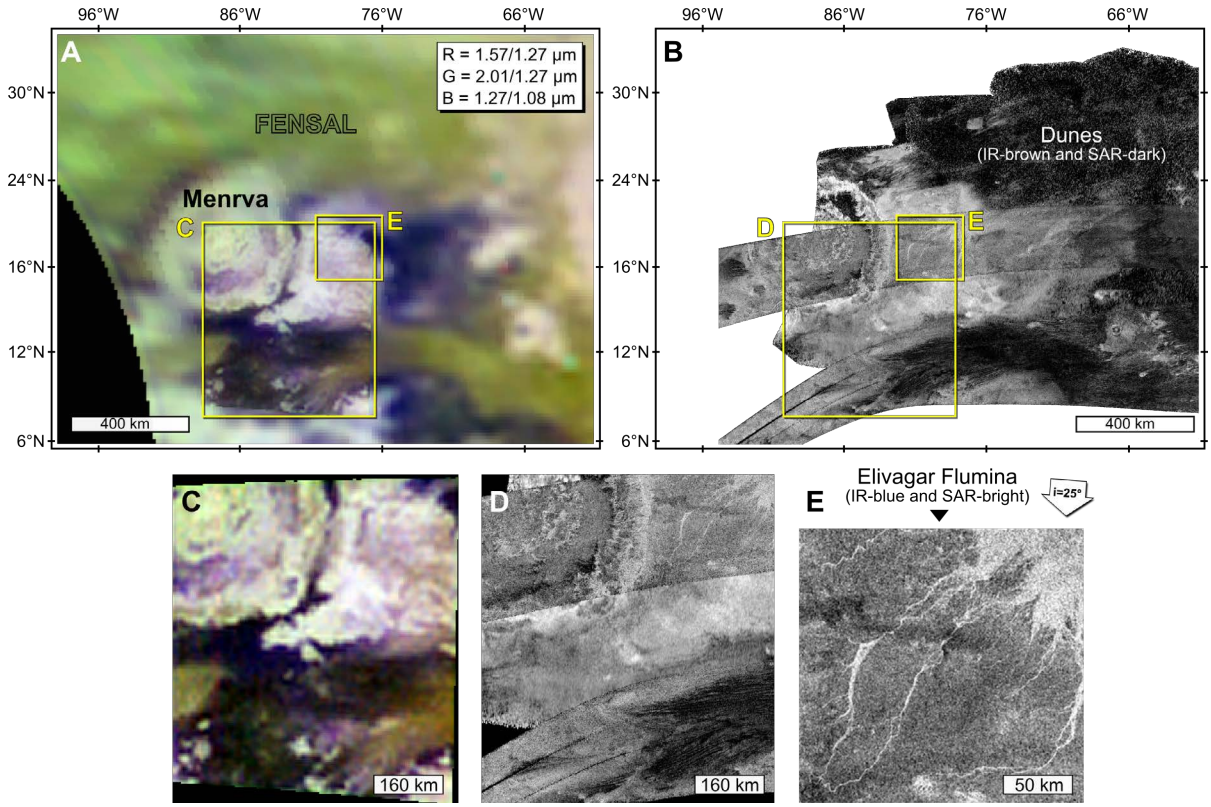

Figure 4.4 – Menrva crater and its surroundings (87°W, 20°N) as seen, for the first time, in VIMS false-color composites of band ratios (red: 1.57/1.27 µm, green: 2.01/1.27 µm, and blue: 1.27/1.08 µm) from flyby T114 (November 2015), at (A) regional-scale and at (C) higher resolution. These new VIMS observations are oversampled with a spatial sampling of about (A) 10 km/pixel and (C) 3 km/pixel, and are empirically corrected from atmospheric effects. (B) Mosaic of SAR images from flybys T3 (February 2005) and T77 (June 2011), with a spatial sampling varying from 700 to 170 m/pixel (same scale as (A)). (D) Close up of the SAR mosaic in (B), at the same location and scale of (C). (E) Close up of the IR-blue and SAR-bright dry fluvial network named Elivagar Flumina, through SAR image from flyby T3. All images are displayed in a simple cylindrical projection, and north is up. The white arrow on (E) indicates the RADAR illumination.

outer and inner rim of Menrva is dark in the SAR swaths, and is therefore relatively smooth at the RADAR wavelength. This area seems to contain a few dark streaks South-East of the crater that are probably dunes. Unfortunately, the resolution of the VIMS observations does not allow distinguishing whether these dunes are found in IR-brown or IR-blue units, or possibly in both.

4.3.4 EASTERN XANADU & CHUSUK PLANITIA

The last region we selected covers the Aztlan sand sea, forming a corridor of dunes starting from the oriental part of Xanadu to Aaru Regio, i.e. from 0 to 20°S and from 0 to 70°W. Two areas were selected in this vast region for our study: eastern Xanadu and Chusuk Planitia, as shown in Figure 4.5.

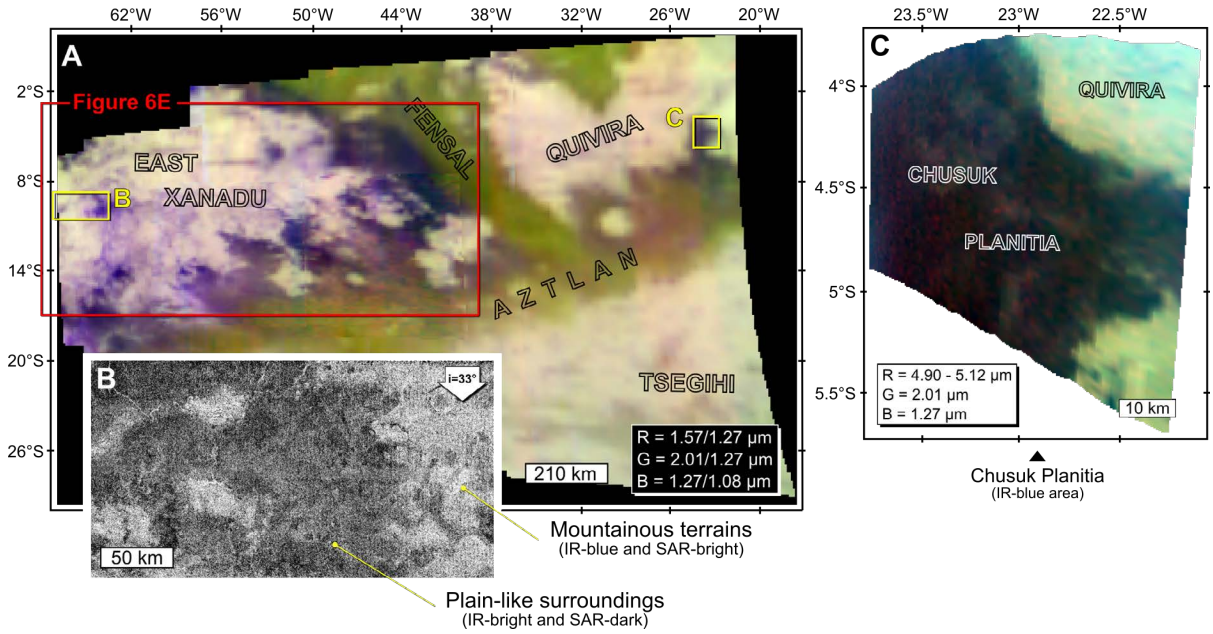

Figure 4.5 – Eastern Xanadu (55°W, 10°S) and Chusuk Planitia (23°W, 4.5°S). (A) VIMS false-color composite of band ratios covering Aztlan region from the recent flyby T114 (November 2015) (red: 1.57/1.27 µm, green: 2.01/1.27 µm, and blue: 1.27/1.08 µm). (B) Close up within the eastern part of Xanadu province through SAR image from flyby T113 (September 2015), displaying the SAR-bright and IR-blue mountains terrains, in contrast to the SAR-dark and IR-bright surroundings. (C) Chusuk Planitia as seen in VIMS observation acquired during flyby T20 (October 2006) (red: average over 4.90-5.12 µm, green: 2.01 µm, and blue: 1.27 µm). The VIMS observations are oversampled with a spatial sampling of about (A) 6 km/pixel and (C) 0.3 km/pixel, respectively, and are empirically corrected from atmospheric effects. All images are displayed in a simple cylindrical projection, and north is up. The white arrow in (B) indicates the RADAR illumination. The red frame in (A) indicates the location of Figure 4.6E.

The eastern part of the IR-bright Xanadu province was first observed at relatively high resolution by VIMS during flyby T9 (December 2005). New observations of this region have been collected by VIMS during the flyby T114 (November 2015, in Figure 4.5A). Features described as branching, dark, and curvilinear are seen in Xanadu and are interpreted as channels in *Barnes et al.* (2007b). These IR-blue channels are inferred to represent surface runoff channels that drain the IR-bright region into the surrounding IR-blue unit, westward of the IR-brown dune areas Aztlan and Fensal. In addition to these channels, IR-bluish patches are found within the IR-bright Xanadu, as also mentioned in *Barnes et al.* (2007b). As shown in Figure 4.5B, those embedded IR-blue patches correspond to SAR-bright patches, suggesting rough and possibly mountainous terrains. Conversely, the IR-bright surroundings exhibit a homogeneous SAR-dark appearance similar to that of plains (*Lopes et al.*, 2016; *Malaska et al.*, 2016a). The SAR swath shown in Figure 4.5B was acquired during flyby T113 (September 2013), and illustrates the contrast between the IR-bluish patches and channels (SAR-bright) and the IR-bright surroundings (SAR dark).

Finally, Chusuk Planitia was described as a dark indentation within the IR-bright Quivira

Table 4.2 – Correlation between the infrared units and SAR features.

IR-units	SAR backscatter	Landforms [refs]
IR-bright	moderate to low	Plains (undifferentiated and variables units) [1,2]
	high	Mountainous terrains, and craters (ejecta, rims and central peaks) [1,2]
IR-blue	moderate	Featureless, plain-like areas [3], and halos surrounding craters [4]
	high	Channels and isolated patches in mountains [5,6]
IR-brown	low (streak-shaped)	Longitudinal dunes [6,7]

Note: [1] *Lopes et al.* (*2016*); [2] *Malaska et al.* (*2016a,b*); [3] *Jaumann et al.* (*2009*); [4] *Le Mouélic et al.* (*2008*); [5] *Barnes et al.* (*2007b*); [6] *Soderblom et al.* (*2007*); [7] *Rodriguez et al.* (*2014*).

plateau (*Jaumann et al.*, 2008). Hence, this region marks the transition between IR-bright and IR-blue units, and farther southward, the IR-brown dunes from Aztlan sand sea. As shown in Figure 4.5C, Chusuk Planitia was observed by VIMS during flyby T20 in October 2005 (cube CM_1540485266) with an averaged spatial sampling of around 0.6 km. Since Chusuk Planitia is found in an IR-blue area, it was suggested to be covered by debris that have been transported after fluvial incision in the IR-bright units (*Jaumann et al.*, 2008). The absence of SAR data in this region does not allows us to state whether or not dunes are present in Chusuk Planitia.

4.3.5 OBSERVATION SUMMARY

Figure 4.6 displays interpretative maps of the regions considered through optical and microwave observations that disclose the infrared units as well as the discernible morphologies (i.e. dunes and channels) seen in SAR swaths. Additionally, Table 4.2 summarizes all those morphologies and their potential correlation with each infrared unit present in our investigated regions. This illustrates that infrared units, despite specific spectral characteristics, do not systematically correspond to one type of SAR brightness unit, especially in terms of roughness and volume scattering, and thus cannot be unequivocally associated with one type of surface feature. Rather, correlation highly depends on the local geological context. For example, the IR-blue units can be found in SAR-bright patches (corresponding to potential local topographic highs) and channels within large IR-bright units, but also in SAR-intermediate and featureless plain-like terrains at the edges of IR-bright units.

The interpretative maps shown in Figure 4.6, combined with the chemical characterization of the three infrared units (bright, blue and brown) (see Section 4.4), will allow us to propose a scenario for the formation of each of those terrains, as well as possible explanations for their geological connections (see Section 4.5).

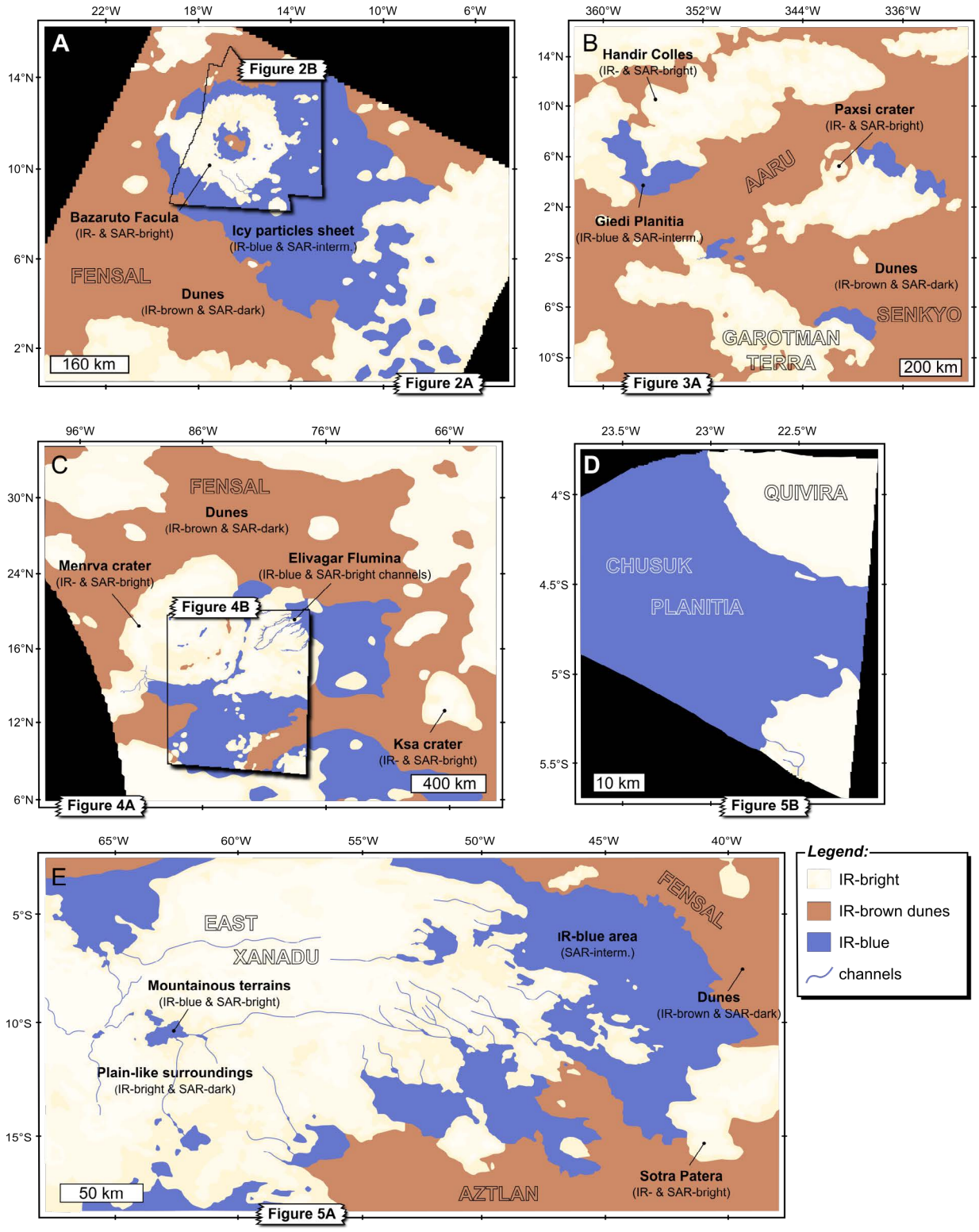

Figure 4.6 – Geologic interpretation of the regions of interest made on the basis of spectral and roughness (and/or volume scattering) variations in VIMS and SAR data, for (A) Sinlap crater, (B) Aaru Regio, (C) Menrva crater, (D) Chusuk Planitia and (E) Eastern Xanadu region. Annotations referring to the original images used for mapping are displayed on each map.

4.4 CONSTRAINTS ON IR-UNITS COMPOSITION

4.4.1 RADIATIVE TRANSFER MODELING

We thus applied a radiative transfer model in order to evaluate the atmospheric effects (gases absorption and haze scattering) on the observed spectra and retrieve the surface albedo of the infrared units. As described in Section 2.2 (see Subsection 2.2.3), the model was developed by *Hirtzig et al.* (2013) and most of the inputs feeding the solver are provided by in-situ measurements made by the instruments aboard the Huygens probe during its descent through Titan's atmosphere in January 2005. Additionally, since a classical approach with the full radiative transfer model is usually time-consuming - several (tens of) days - we decide to improve our inversion with the use of a reference Look-Up Table (LUT) (*Maltagliati et al.*, 2015), as explained in Subsection 2.2.3.

This inversion with the LUT has been applied to all the VIMS cubes listed in Table 4.1. For each of these cubes (representing in total more than 50,000 spectra), we thus obtained maps of Lambert albedo (A_L) of the surface in the eight infrared atmospheric windows. In order to dispense with the highly variable observation geometries and for the ease of comparison, we then convert the output Lambert surface albedo (A_L) into single-scattering albedo (ω_0), following the *Hapke* (2012) formalism in the case of an isotropic scattering and compacted medium. Finally, we use masks in our regions of interest (RoIs) to extract surface single-scattering albedo information for each of the spectral units, namely IR-bright, -blue and -brown units, found within each of the selected cubes (see Appendix B).

4.4.2 SPECTRAL SLOPES COMPARISON

Figure 4.7A shows spectra of the single-scattering albedo in the seven atmospheric windows, calculated from the radiative transfer model for the infrared units found in Sinlap crater and its surroundings. Spectra obtained for each region investigated are provided in the Appendix B. The spectral differences between the various infrared units on Titan essentially appear at the short wavelengths, using the 1.27, 1.57 and 2.01 µm window images (*Rodriguez et al.*, 2006). We therefore decided to extract and compare the spectral slopes of the single-scattering albedo between these windows, i.e. 1.57/1.27 µm, 2.01/1.27 µm, and 1.57/2.01 µm, for the three infrared units identified in our RoIs. Spectral slopes are particularly sensitive to subtle heterogeneities in the composition and physical structure of the surface material (e.g. *Mustard and Sunshine*, 1999).

Scatter-plots displayed in Figure 4.7B show an example for the results obtained for Sinlap crater and its surroundings as observed during the T110 flyby. The three infrared units cluster in different regions of the spectral slope space. This strongly suggests that (1) each unit has intrinsically a relatively uniform spectral behavior, and (2) they represent significant

distinctions in spectral behaviors between them, which suggest that they are likely to differ in composition and/or grain size. However, Figure 4.7C, which represents the same plots for all our RoIs, illustrates the more "transitional" behavior of the units at global scale. When comparing the 1.57/1.27 µm spectral slope as a function of the 2.01/1.27 µm spectral slope (left column in Figures 4.7B and 4.7C), and the 1.57/2.01 µm spectral slope as a function of the 2.01/1.27 µm spectral slope (right column in Figures 4.7B and 4.7C), we observe a consistent trend in which the IR-blue unit has the lowest 1.57/1.27 µm, and 2.01/1.27 µm ratios, and highest 1.57/2.01 µm ratio. Conversely, the IR-bright unit shares the highest 1.57/1.27 µm, and 2.01/1.27 µm ratios, and lowest 1.57/2.01 µm ratio.

4.4.3 SPECTRAL MIXING MODELING

For comparison purposes, we also use a spectral mixing model to generate a spectral library for linear binary mixtures of water ice and tholins (*Hapke*, 2012), as described in Section 2.3. We vary the grain sizes (from 50 nm to 1 mm in diameter) and the mixing fraction (from 0 to 100%) of the two components. Owing to the low spatial resolution of our observations, linear (also referred as areal) mixing is assumed to be the best suited effect occurring for capturing natural surface heterogeneities (*Villa et al.*, 2011), and non-linear mixing is therefore not considered in our investigation.

For every pixel (10,576 in total) of the selected spectral units in our RoIs, we then search for the linear binary mixture (varying water ice/tholins mixing factor and grain size of each component) that simultaneously best reproduces the combined single-scattering albedo in each of the 1.27, 1.57 and 2.01 µm-windows (expressed in ω_0) retrieved from the observations. We select the best solution among all the possible solutions that conservatively matches a 5% total relative difference between the observations and the model. Figure 4.8 displays the best solutions for our RoIs selected within the IR-bright, -blue and -brown units (from left to right column, respectively), while a summary can also be found in Table 4.3.

Considering the results for our linear mixing model, statistically, the IR-bright unit appears to be largely dominated by fine-grained tholins (80% of the mixture), of a few tens of microns (about 25 microns in average), with a residual amount of large-grained water ice (possibly greater than our largest size of 1 mm, in Figure 4.8, left column). In addition, our linear mixing model shows a possible contribution of smaller water ice grains for a few spectra (around 15%) of the IR-bright RoIs, all dominated by the presence of tholins.

Our linear binary mixing model finds a solution for all the pixels in the RoIs of the IR-blue units. Interestingly, the IR-blue unit is characterized by significant water ice enrichment relative to the other units, with 60% of tholins in average (Figure 4.8, middle column). The water ice component presents a grain size distribution that is slightly broader than for the IR-bright unit, starting with grains of a few hundreds of microns and reaching millimeter-

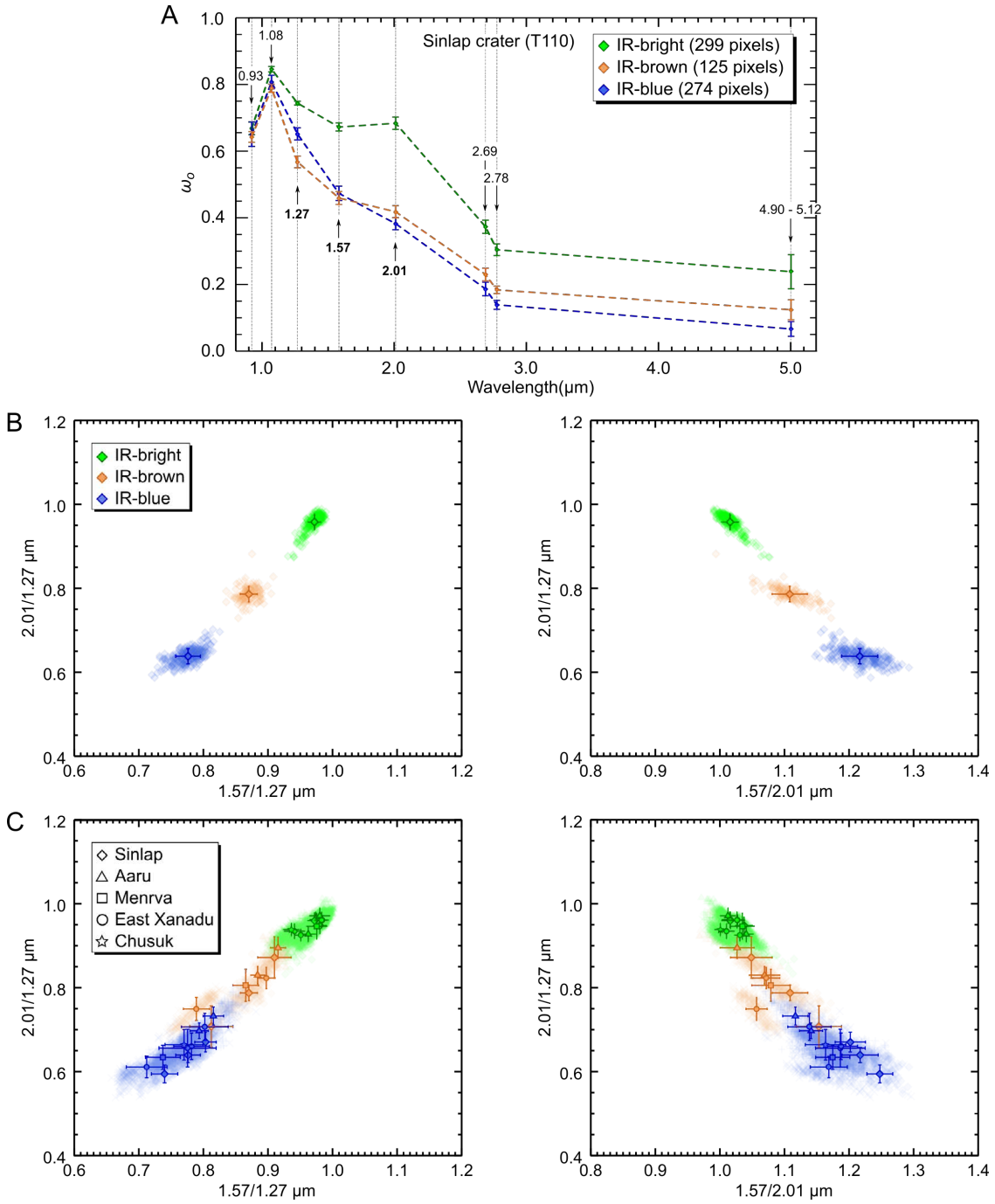

Figure 4.7 – Top row: (A) Spectra of the averaged single-scattering albedo (ω_0) in the eight infrared atmospheric windows for all the pixels comprised in each RoI of the VIMS observation targeting the Sinlap crater area (T110, CM_1805209469), as an example showing the distinct spectral characteristics of each infrared unit: IR-bright (green plots), IR-brown (brown plots) and IR-blue (blue plots) units. The number of pixels comprised in the RoIs is indicated in the top-right corner of the plot. Middle and bottom rows: Scatterplots of the (left) 1.57/1.27 μm vs 2.01/1.27 μm, and (right) 1.57/2.01 μm vs 2.01/1.27 μm spectral slopes for the infrared units. The spectral slopes are calculated from the single-scattering albedo spectra retrieved with the radiative transfer model (see text for details). Those are the results obtained for (B) the Sinlap crater area through the VIMS observation from flyby T110, and (C) all the investigated regions (all RoIs): Sinlap crater, Aaru Regio, Menrva crater, eastern Xanadu province, and Chusuk Planitia. Error bars are the standard deviation.

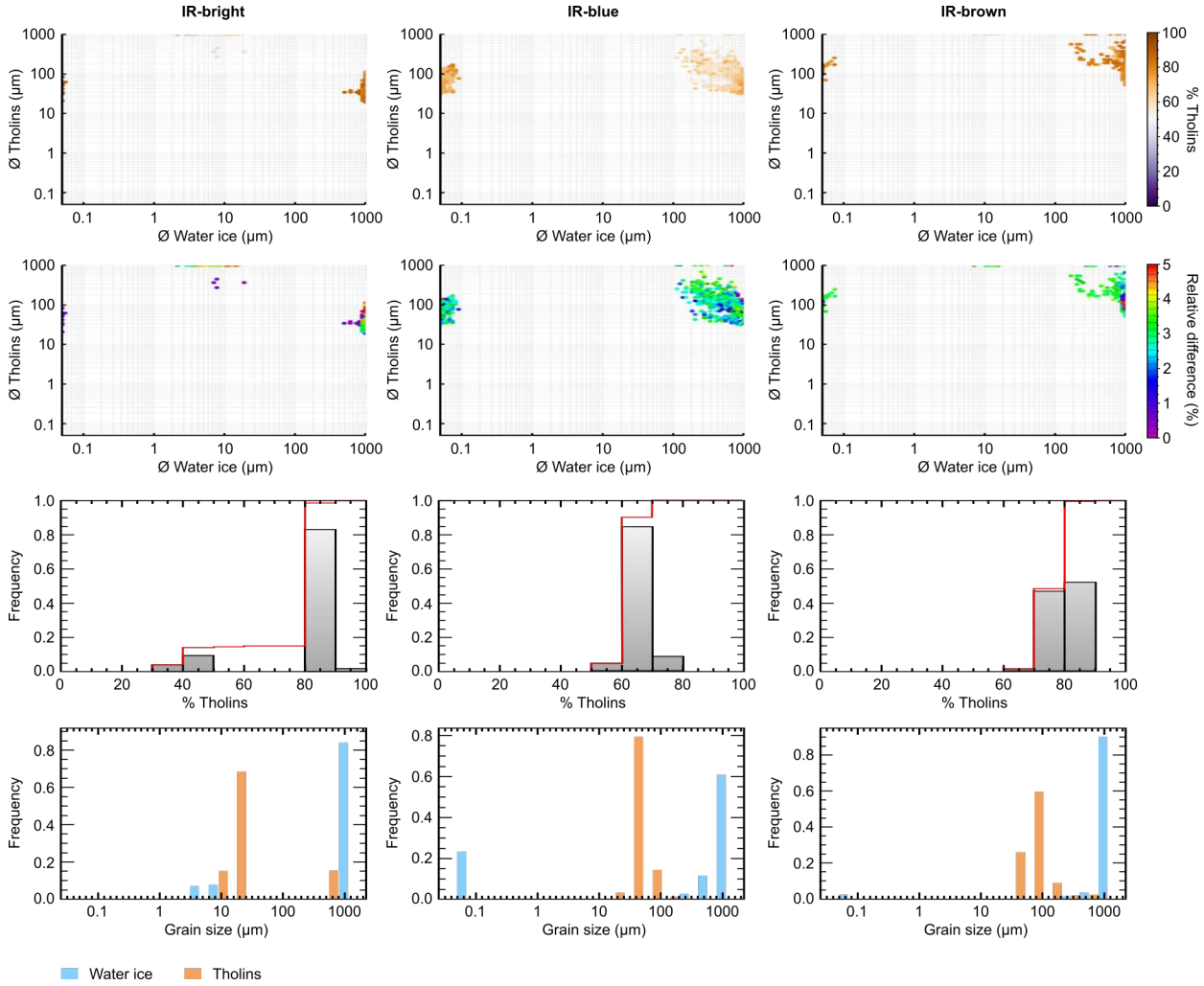

Figure 4.8 – The first row shows diagrams reporting all possible linear mixtures of water ice and tholins that could reproduce the combined single-scattering albedo values (ω_0) in each of the 1.27, 1.57 and 2.01 µm-windows range of the considered infrared units by varying grain sizes of both components (diameter in microns), and mixing fraction (% of tholins), for the IR-bright, -blue and -brown units (from left to right column, respectively). The second row shows diagrams reporting the relative difference between the observed values (retrieved from the radiative transfer inversion) and the synthetic spectra of linear mixtures. The last two rows are histograms displaying the number of solution for each parameter: (third row) tholins content, and (fourth row) water ice and tholins grain sizes (in blue and orange, respectively). Grain sizes are comprised between 50 nm and 1 mm in diameter for both components.

Table 4.3 – Synthesis of the spectral mixing modeling.

	IR-bright	IR-blue	IR-brown
Total number of pixels in RoIs	4585	4717	1274
Total number of solutions	4544	4717	1261
% of solutions	99.1%	100%	98.9%
Mixing ratio (in % tholins)	80	60	70 - 90
Water ice grain size (in µm)	800	600 - 800	800
Tholin grain size (in µm)	10 - 25	25 - 100	50 - 200

Note: Best retrieved solutions (with the highest frequency) obtained for the IR-bright, -blue and -brown spectral units selected within the RoIs (see also Figure 4.8).

sized grains. Our inversions show a possible contribution of submicronic water ice for a few spectra (around 20%) of the IR-blue RoIs. The tholin component shows a grain size distribution ranging from a few tens to hundreds of microns (about 50 microns in average, in Figure 4.8, middle column).

Finally, our mixing model successfully reproduces most of the spectra we selected in the IR-brown units. Following the results of our modeling, the IR-brown dune areas display similar characteristics to those of the IR-blue unit in terms of grain sizes, except that the tholins are expected to be slightly larger (about 100 microns in average, in Figure 4.8, right column). However, the distribution in water ice content of the mixture peaks at a higher fraction of tholins, around 80%, like in the IR-bright unit. This validates the initially thought enrichment in water ice for the IR-blue unit relative to the IR-brown unit, and its depletion in the dune areas (*Soderblom et al.*, 2007a; *Rodriguez et al.*, 2014).

4.5 GEOLOGIC INTERPRETATION

4.5.1 IR-BRIGHT UNITS

Our spectral mixing model reveals a small amount of water ice (<20%) in the IR-bright units investigated (Figure 4.8, left column). Moreover our modeling indicates that the IR-bright unit is dominated by small-sized (a few tens of microns) tholins expected to result from the atmospheric fallout (*Tomasko et al.*, 2008). This continuous fallout may form a fresh, fine-grained organic sedimentary layer that ends up covering the icebed over geological timescales. Cassini's RADAR can be used either as a SAR imager (active mode) or as a thermal radiometer (passive mode) at 2.18-cm wavelength (*Elachi et al.*, 2004). Thus, based on these two RADAR modes, *Janssen et al.* (2016) suggest the presence of water ice in the near-surface where ground features display high SAR backscatter and low thermal emissivity at a wavelength scale of 2.18 cm. These latter correspond to mountainous terrains and craters (particularly ejecta, rim and central peak), and they represent only a minor fraction of the

whole IR-bright unit. Conversely, it appears that the major fraction of the IR-bright unit on Titan, corresponding to the plains, exhibit a moderate-to-low SAR backscatter and high brightness temperatures, as shown by radiometry data analysis, which is consistent with organic material (*Janssen et al.*, 2016; *Lopes et al.*, 2016; *Malaska et al.*, 2016a). Hence, it has been assumed that the mountainous terrains and craters are partly or entirely coated by a superficial layer of organic sediments (*Barnes et al.*, 2007a; *Soderblom et al.*, 2007a; *Clark et al.*, 2010). As VIMS is only sensitive to the first few microns of Titan's surface, this layer is expected to be sufficiently thick in order to mask the infrared spectral signature of most of the underlying icebed.

Nevertheless, a few patches of IR-blue materials are seen within large IR-bright units, notably Xanadu province, which also show a bluish appearance in VIMS false color composites (Figure 4.5), as notified in earlier investigations (*Barnes et al.*, 2007b; *Soderblom et al.*, 2007a; *Langhans et al.*, 2012). At a global scale, which implies resolutions over a few to several tens of kilometers, the IR-bright units appear spectrally uniform. However, these seemingly uniform IR-bright units exhibit substantial albedo heterogeneities at a smaller scale when the spatial sampling of the images becomes sufficiently high, below 10 km/pixel. *Langhans et al.* (2012) demonstrated that these IR-bluish heterogeneities possess the spectral behavior of a mixture of IR-bright and -blue units. This suggested that those IR-bluish patches are embedded into the IR-bright units and are probably too small to be fully resolved by Cassini's infrared imaging data as part of the IR-blue unit. The IR-bluish patches are found in small SAR-bright mountainous terrains and surrounded by IR-bright and SAR-dark plains (*Barnes et al.*, 2007b; *Soderblom et al.*, 2007a). These features could represent icy outcrops in heavily degraded terrains, as the icebed is washed clean of surficial organic sediments after episodic rainfalls. Alternatively, they could also represent accumulated water ice erosional products coming from the degradation of the icebed and covering an organic layer.

Furthermore, the minor fraction of the IR-bright units represented by mountainous terrains and craters seems to be significantly modified by erosional processes, with sharp incisions by liquid hydrocarbons flows after rainfalls (e.g. *Langhans et al.*, 2012), more than any other terrains on Titan. Fluvial networks cutting through the IR-bright units were first seen in the DISR images acquired during the descent of the Huygens probe in January 2005 (*Tomasko et al.*, 2005). Since then, it has been shown that fluvial features are mostly found in the IR-bright units on Titan (*Lorenz et al.*, 2008; *Burr et al.*, 2009, 2013; *Radebaugh et al.*, 2011; *Langhans et al.*, 2012, 2013). Nevertheless, the selected areas in this study do not seem to be completely covered by channels. Indeed, it has been shown that fluvial features are mainly concentrated to the poles, while only a few occurrences are seen at lower latitudes (*Birch et al.*, 2016a; *Lopes et al.*, 2016; *Malaska et al.*, 2016a). This lack of fluvial features might be a resolution effect, since Cassini's imaging instruments are limited to resolutions at best of 300 m. Few distinct IR-blue channels were identified or merely detected at low-latitudes,

starting from the IR-bright units and draining into the IR-blue units (*Barnes et al.*, 2007b; *Jaumann et al.*, 2008, 2009; *Langhans et al.*, 2012; this work). Those channels are commonly bright in SAR swaths. This supports the hypothesis of the IR-bright units being eroded by fluids, from which material detached from the icebed is transported to the IR-blue units (*Barnes et al.*, 2007b; *Jaumann et al.*, 2008, 2009).

4.5.2 IR-BLUE UNITS

4.5.2.1 THE CASE OF OUTWASH PLAINS

Apart from the previously mentioned small-scale IR-bluish features embedded in IR-bright areas, IR-blue units are mostly found at the margins of IR-bright units, and around impact craters. It has been thought that those IR-blue units might host surface material enriched in water ice (*Rodriguez et al.*, 2006; *Barnes et al.*, 2007b; *Jaumann et al.*, 2008, 2009; *Le Mouélic et al.*, 2008; *Rodriguez et al.*, 2014). Our work (Figure 4.8, middle column) shows that the spectral signature of the IR-blue units is, indeed, in very good agreement with the water ice enrichment hypothesis relative to the other infrared units. The enrichment is particularly striking when comparing the water ice mixing fractions of the nearby IR-bright unit. Indeed, the latter barely exceeds 20% of water ice, whereas the IR-blue unit presents mixing fractions starting from 20% and reaching 50% of water ice. This water ice could correspond to icebed exposure, or even icy debris laying on surface after degradation of the icebed. It is also worth noting that, despite a clear enrichment in water ice, IR-blue units are not systematically predominantly made of water ice. As for IR-bright units, the grain size distribution of the water ice component for the IR-blue unit shows grains that are in majority larger than hundreds of microns, but the spread is skewed towards smaller sizes, with the modeling suggesting some submicronic grains (Figure 4.8, middle column). This heterogeneity in grain sizes could be related to mechanical erosion from material being transported downstream from the IR-bright unit that may break large pebbles of the icebed and then turned them into smaller blocks during transport and deposition onto the IR-blue unit (*Barnes et al.*, 2007b; *Jaumann et al.*, 2008, 2009). For instance, water ice within IR-blue units located east of Xanadu, as well as those present in Chusuk and Giedi planitiae, and around the craters, may represent erosion products derived from the fluvial incision of the icebed in the nearby IR-bright units (Figure 4.5). This water ice could have been washed out and carried by flows of liquid hydrocarbons from presumably more elevated IR-bright units, and hence contribute to the slight areal water ice enrichment of the IR-blue units detected by VIMS. The tholin component inferred from our calculations also displays a spread in the grain size distribution, but skewed towards larger sizes, allowing tholins ranging from several from several tens to hundreds of microns in the IR-blue units, larger than those fit by the model in the IR-bright units. This change in the tholin grain size distribution could argue for a progressive

processing, which results in grain size sorting of the organic material from small-sized tholins (analogous to atmospheric aerosols) to larger grains. They may grow in size by compaction or sintering over long timescales (*Barnes et al.*, 2015) in the depositional layer of the IR-bright units and then be eroded, along with the icebed material, and transported by flows from the IR-bright highlands to the IR-blue areas and deposited there. Thus, these IR-blue units could be the signature of outwash plains hosting icy blocks and pebbles, along with sediment down in size to hundreds of microns. Interestingly, similar materials were detected at the Huygens landing site (*Tomasko et al.*, 2005), an area also located in the IR-blue units, where pebbles are suspected to be made of water ice, and overlaid at some places with a layer of darker, finer-grained tholin-like sediments. Both components being transported from the IR-bright to the IR-blue units through fluvial processes.

Note that the IR-blue units surrounding impact craters, referred as halos in this work, were originally interpreted as icy deposit sheets set down from vapor plumes formed during impacts, notably in the case of Sinlap crater (*Le Mouélic et al.*, 2008), as illustrated in Figure 4.9. Here, we consider that such icy sheet deposits should be covered by organic material derived from atmospheric fallout and then could be modified by subsequent erosional processes and aeolian deposition. Indeed, IR-bright crater rims are thought to undergo from erosional processes similar to those occurring in the mountainous terrains (*Barnes et al.*, 2007b; *Jaumann et al.*, 2008, 2009). Icy materials constituting craters rims and ejecta are therefore washed out by rainfalls and/or winds, along with organic coating materials, towards the surrounding icy sheet deposits at lower elevations. This could contribute to exposing the icebed and to the enrichment of water ice around the craters (i.e. IR-blue halos), as suspected for Elivagar Flumina crossing the ejecta blanket of Menrva crater (*Radebaugh et al.*, 2016) for instance. Moreover, Selk crater (199°W, 7°N) may also be a case example of such phenomena, as it has IR-blue units exposed along the outer flank of the entire rim, extending out to the IR-brown sand sea in which the crater is set (*Soderblom et al.*, 2010).

4.5.2.2 IR-BLUE UNIT BURIAL

The map (Figure 4.1D) shows that the IR-blue units cover only 1.5% of Titan's surface (1.3 million km^2); this small fraction could be consistent with IR-blue units encroached upon by the dunes in places where the wind can transport sands. Moreover, IR-blue units are commonly located at the eastern boundaries of IR-bright units, on the downwind side of topographic obstacles (*Lucas et al.*, 2014b; *Charnay et al.*, 2015). Thus, this suggests that IR-blue units are preserved from being covered by wind-blown sands and hence from the current dune migration (*Malaska et al.*, 2016a,b). To date, the IR-blue halo around Sinlap is still present, as the crater seems well-preserved and likely recent (*Lorenz et al.*, 2007). Conversely, for older craters, like Paxsi, the associated icy halos are partly or even fully

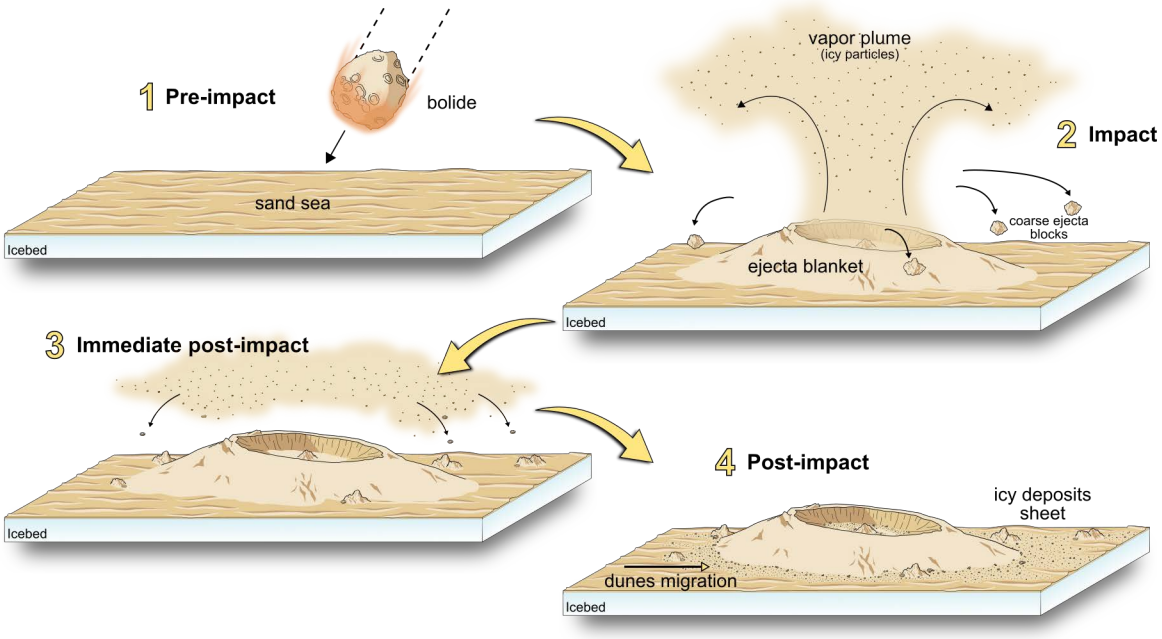

Figure 4.9 – Cartoon model displaying a satisfactorily formation scenario for impact craters on Titan. (1) The pre-impact site consist in a sand sea covered by longitudinal dunes. (2) During the impact, the main ejecta blanket is built, while a vapor plume extends to the atmosphere. (3) The icy vapor plume is then blown downwind, forming a icy-rich halo surrounding the crater once deposited on the ground. (4) After the impact, those icy deposits might be modified by erosional processes and aeolian deposition.

overtaken by dunes, as seen in the SAR swaths. Thus, we infer that these IR-blue units should exist until the dunes entirely buried them.

4.5.3 IR-BROWN UNITS

Numerous analyses of VIMS observations have suggested that the VIMS spectrum of dunes does not correspond to water ice, but broadly matches with organics, including analogues of airborne aerosols (tholins) (*McCord et al.*, 2006, 2008; *Barnes et al.*, 2007a; *Soderblom et al.*, 2007a; *Barnes et al.*, 2008; *Clark et al.*, 2010; *Rodriguez et al.*, 2014). Moreover, measurements performed by the RADAR in passive radiometer mode have confirmed that the composition of the dunes cannot be based on pure water ice (*Janssen et al.*, 2009, 2016). Further studies even potentially identified absorption signatures of benzene (*Clark et al.*, 2010) and acetylene (*Singh et al.*, 2016) in these dune areas. Our spectral mixing model reveals that IR-brown units are predominantly made of tholins (80% in average in Figure 4.8, right column), with a grain size distribution similar to that of the IR-blue units, ranging from several tens to hundreds of microns. The predominance of organic material in dune areas is in agreement with the results obtained in the aforementioned studies. This suggests that organic materials detected in IR-bright units derived from atmospheric fallout, could be

modified by surficial processes and be at the origin of the sand material composing the dunes. The smallest grains of tholins (tens of microns) may be representative of a coating of organic dust, covering the dune material made of organic sand that are expected to consist of larger particles, exceeding hundreds of microns (over 200 microns in *Lorenz*, 2014 and *Burr et al.*, 2015). This coating could mask part of the dune material at infrared wavelengths, which are only sensitive to the very first microns of the surface. Such organic dust has been detected by the DISR instrument at the Huygens landing site (*Schroeder et al.*, 2012), revealing the widespread geographic distribution of dust on Titan, especially over IR-blue and IR-brown units. Having a similar size distribution to that in the IR-blue units, this organic dust can originate from part of the IR-blue outwash plains, being then blown by the wind and accumulating in the IR-brown areas. The larger sand material composing the dunes may possibly be formed from this organic dust, itself formed from atmospheric aerosols. Finally, the large-grained water ice component of the IR-brown dune areas of our study may represent the partial areal exposure of the icebed in some of the interdunes in areas of more limited organic sediment availability, as suspected by *Barnes et al.* (2008); *Rodriguez et al.* (2014) and *Bonnefoy et al.* (2016).

4.5.4 CONNECTING THE INFRARED UNITS

If the organic sand forming the dunes derives from the atmospheric fallout, then the composition of the dune material and its source should directly reflect that of the haze particles. Nonetheless, despite the fact that dunes are commonly found in the IR-brown units (*Soderblom et al.*, 2007a; *Rodriguez et al.*, 2014), the complete history of organic sand, from its source to its sinking, still remains enigmatic. Here, we propose that the sources of the dune materials could either (1) show the same spectral signature as the dunes and hence appear also IR-brown (same composition and grain size according to our spectral mixing model), or (2) have a different spectral signature and might appear IR-bright (same composition, but different grain size) due to mechanical erosion and transport processes affecting both the icebed and the organic materials masking it.

In order to test the first hypothesis, it is necessary to look for IR-brown areas where SAR imagery does not detect any dunes. A few isolated IR-brown dune-free areas are seen at the mid-latitudes, around 30° latitudes (green areas in Figure 4.10) and could be potential sources for dune material, but most of them are not seen in SAR data. However, the sizes and locations of these possible sand sheets can hardly make those areas the sources of the equatorial dunes. Their locations are particularly difficult to reconcile with the equatorial concentration of the dunes, since the sediment pathways are commonly expected to diverge poleward at latitudes higher than 15°N/S (*Lucas et al.*, 2014b; *Charnay et al.*, 2015; *Malaska et al.*, 2016b). If these potential sand sheets can be possibly connected to the few isolated

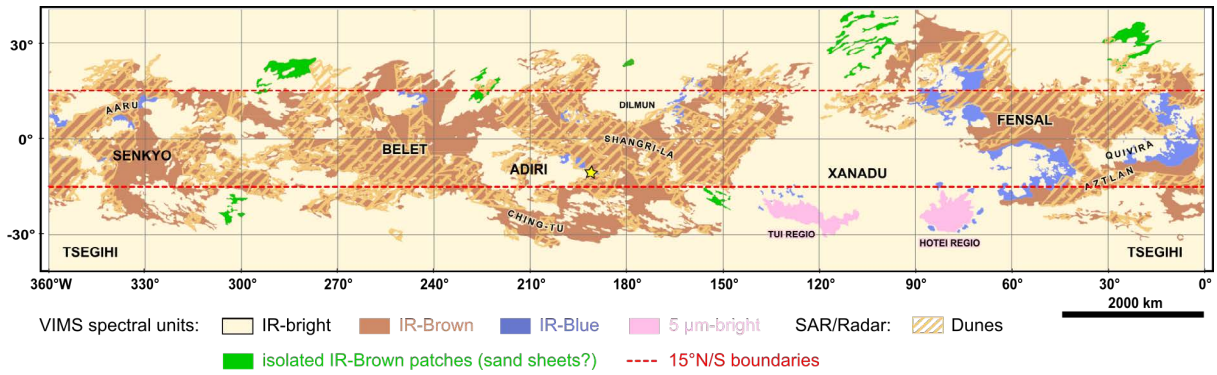

Figure 4.10 – Same as Figure 4.1D, where the green areas represent isolated IR-brown patches that could correspond to potential sand sheets. Red lines mark the 15°N/S boundaries. Note that most of those candidate areas are not observed by the SAR imager (see Figure 4.1C).

dunes found at higher latitudes, they cannot explain the presence of most of the large sand seas found closer to the equator. Following the predictions of *Lucas et al.* (2014b) and *Charnay et al.* (2015), the sand fluxes converge toward the equator only for latitudes between 15°N/S, where most of the dunes are observed, making this latitudinal belt a sand trap. Interestingly, *Malaska et al.* (2016b) have shown that the transport of dune material found within about 15°N/S is stable and remains along the equator. Otherwise, outside these boundaries, the dune material tends to deviate poleward and to accumulate in the mid-latitudes, around 30° latitudes (*Malaska et al.*, 2016b). Hence, the sand material detected in the IR-brown dunes areas should originate from the equatorial regions.

Hence, we propose an alternative explanation, where the sources of dune material have a different spectral signature corresponding to that of the IR-bright unit. In this case, sand material could derive from the degradation of the high-standing landforms in the IR-bright units and the subsequent transport to the lowlands, which consist of the IR-blue and -brown units, as discussed in *Jaumann et al.* (2008). To illustrate this assumption, we propose a cartoon model (Figure 4.11) showing a complete history of the sediment transport in the equatorial regions, by combining atmospheric and surficial processes. On highlands, methane rainfalls cause the fluvial erosion of the icebed and the organic sedimentary layer masking it. This organic sedimentary layer being primarily made of the smallest tholins grains (Figure 4.8), accumulated from atmospheric fallout, creates the IR-bright unit that exhibits a high albedo in VIMS spectra with respect to the other considered units. Erosion products, comprising both water ice and organic coating materials, are transported through channels flowing across the IR-bright plains towards lowlands. Depending on the outflow in the channels, large particles to pebbles could be transported by the liquids (*Collins*, 2005). Then, the deposition of these erosion products results in grain size sorting and hence implies a compositional discrimination where ice-rich, large-grained materials lie on top and creates the IR-blue unit (outwash plains, or alluvial fans in *Birch et al.*, 2016b and *Radebaugh et al.*,

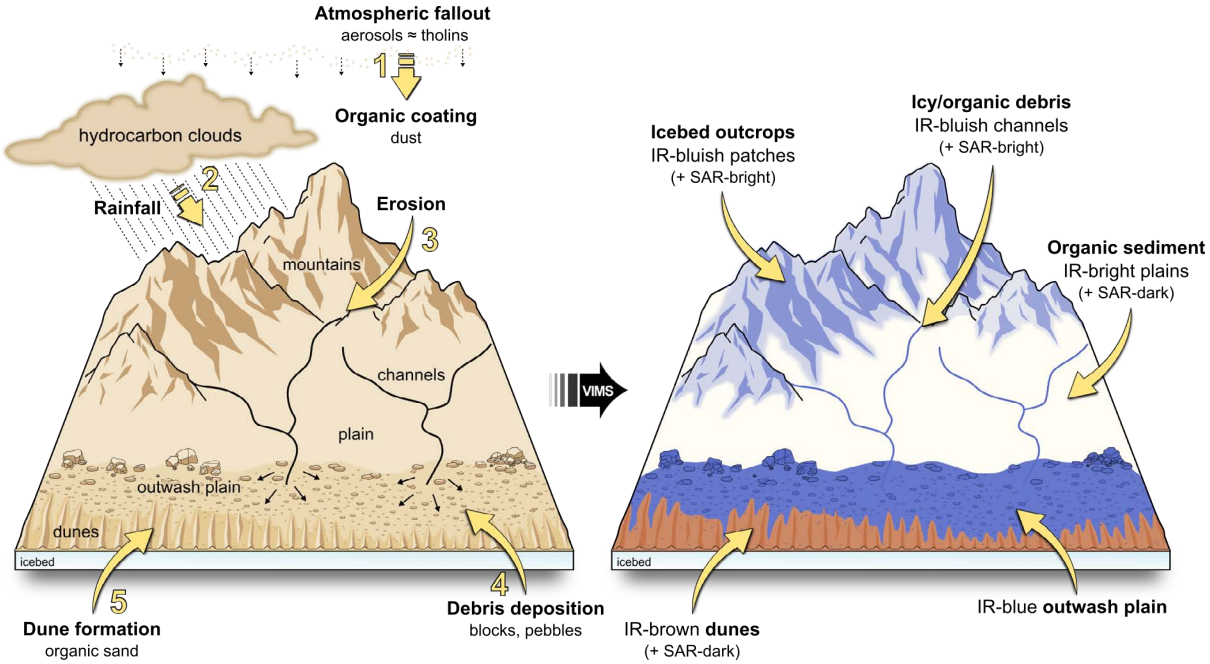

Figure 4.11 – (left) Cartoon model illustrating the series of processes that could explain the actual distribution and the structural relationship of the infrared units in the equatorial belt of Titan, as seen through usual VIMS composites (right). In the atmosphere, photochemically produced aerosols fall down on the surface and form an organic sedimentary layer covering the icebed. Additionally, methane condenses and precipitates, which leads to the degradation of mountainous terrains (and craters rims) via rainfalls. This degradation is followed by the transport of debris, including organic sediment and icebed material, through fluvial channels crossing the plains (and ejecta blankets). The debris are then washed out at the margins of the IR-bright units, resulting in a IR-blue outwash plain exhibiting blocks and pebbles similar to those seen in the Huygens landing site (*Tomasko et al.*, 2005), which is also IR-blue (*Rodriguez et al.*, 2006). The outer boundary of the IR-blue units mark the beginning of the dune fields formation, essentially made of organic sand. IR-bluish patches seen in mountainous terrains indicate a strong erosion of those terrains that could probably expose the icebed.

2016). In IR-blue outwash plains, materials are moved farther away by wind, causing further grain size sorting, where aeolian processes may create granular mixtures of water ice and organic materials. These granular mixtures become the IR-brown unit, in which the grains that are small enough to saltate[2] (sand) are shaped into dunes and the grains even smaller are blown away into dust storms.

As explained earlier, some traces of large-grained water ice are expected by our spectral mixing model, which could be compatible with the presence of the water ice exposed in the interdunes (icebed or icy debris) that are included alongside with dunes in the IR-brown unit in our study. The interdune composition and/or grain size is seen to vary spatially over Titan (*Le Gall et al.*, 2011, 2012; *Bonnefoy et al.*, 2016; *Lucas et al.*, 2017), and could correspond to that of the neighboring terrains that the dunes are developing upon, such as

[2]saltation = low hopping process by which sand move (carried by the wind) to form the dunes.

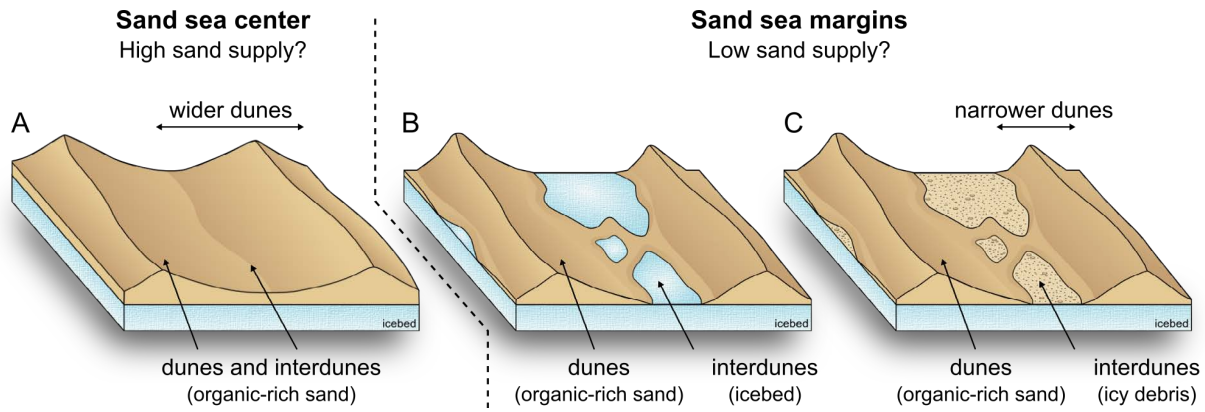

Figure 4.12 – Cartoon models showing the different relationships between dunes and interdunes in the equatorial belt of Titan. (A) In the middle of sand seas, dunes and interdunes are both made of organic sand material that could imply a high sand supply. Conversely, at the margins of sand seas (or near topographic obstacles), interdunes are probably lacking in sand material. This deficiency could lead to the exposure of underlying material that could correspond to (B) icebed or (C) icy debris resulting from previous erosional processes or impact cratering. Note that the dunes seem larger toward areas with higher sand supply, as explained in *Bishop et al.* (2017) and *Lewis et al.* (2017).

mountainous terrains, crater ejecta and rims, or even IR-blue units. Thus, the interdune signature in the infrared range strongly depends on the location of the investigated dune areas and the spatial resolution of the available VIMS cubes. We suggest that the dunes are actively developing from the fine organic material transported along with icy grains over the older water ice-rich hills and plains. Recent analysis of the morphometric variations of the dunes with the RADAR data tends to confirm those assumptions, as described in *Bishop et al.* (2017) and *Lewis et al.* (2017). Dunes are expected to be wider at low latitudes, which generally corresponds to the sand seas centers (*Le Gall et al.*, 2011; *Savage et al.*, 2014). Conversely, they are narrower at the margins or near topographic obstacles (*Le Gall et al.*, 2012), which could explain the exposure of underlying ice material in the sand-free interdunes. Figure 4.12 depicts the distinctions between sand-rich and sand-free interdunes that appear to be influenced by the proximity to sand sea margins.

4.6 SUMMARY

In this chapter, I discussed about the infrared properties and geological relationships of the three spectral units detected in the equatorial regions of Titan based on VIMS observations and SAR swaths for detailing the geomorphological context. The joint use of updated radiative transfer and spectral mixing models for grains of water ice and tholins (see Chapter 2) gave new insights on the composition and structural relationships between the major infrared units found in Titan's low latitudes. The results shown in this chapter support a number of assumptions made in previous studies during and even prior the Cassini-Huygens mis-

sion. Hence, through this study, I have shown that all the infrared units considered appear to contain organic material (here tholins) that likely derive from the atmospheric fallout. The presence of a mixture of medium-sized tholins and large grained water ice could explain the low albedo of the IR-brown and -blue units relative to the IR-bright unit, composed in majority by fine grained tholins. Interestingly, IR-blue units are clearly enriched in large water ice grains in comparison to the other considered units. This water ice material could result from the mechanical erosion of the icebed following hydrocarbon rainfalls on highlands. Thus, I confidently suggest a scenario that can explain the current distribution of the infrared units present in the equatorial belt, as illustrated in Figure 4.11. This distribution is very similar to that of a transition from mountains to stony and sandy deserts on Earth (Figure 4.13). I therefore expect the presence of mountainous terrains near the IR-blue and -brown dunes transition. IR-blue units would be analogous to the terrestrial stony deserts (also called *regs*), where ice and organic materials are laid after erosional and depositional processes from the IR-bright units. Conversely, IR-brown units would be analogous to the terrestrial sandy deserts (also called *ergs*) that are covered by longitudinal dunes mainly made of organic sand, in the case of Titan.

Since my proposed scenario implies geologic processes that are partly driven by the topography, as the IR-bright units must be elevated relative to the IR-blue outwash plains and IR-brown dunes areas, the topographic distribution of the three infrared units should thoroughly be investigated. Analysis of topographic data acquired by RADAR could support the assumptions made in this chapter, particularly with the SARTopo (*Stiles et al.*, 2009) and Altimetry (*Zebker et al.*, 2009a) datasets. By using such data, recent studies obtained significant information about the superposition relations between the major landscapes on Titan. Mountainous terrains and craters are often defined as the oldest geomorphologic units, and are found to be topographically higher than plains and dunes (*Birch et al.*, 2016a; *Lopes et al.*, 2016; *Malaska et al.*, 2016a). However, the horizontal resolution and vertical accuracy of those data are not necessarily suited for the relatively small scale of the transition zones studied here. For instance, an elevation difference of a few tens of meters will be comprised within the vertical accuracy of the topographic data (75 m for SARTopo, and 35-50 m for Altimetry). Even so, a recent study of Menrva crater area shows a topographic profile, describing a moderate regional gradient from the elevated crater rim to the end of the Elivagar Flumina fans, in the lowlands (*Radebaugh et al.*, 2016). This latter work exactly matches with our proposed scenario from Figure 4.11. Additionally, an accurate and complete model for sediment formation and transport could test our hypotheses, giving further insights in the origin and transport of debris through liquid hydrocarbons and/or winds, from the mountainous terrains and craters (IR-bright unit) to the outwash plains (IR-blue unit) and sand seas (IR-brown unit).

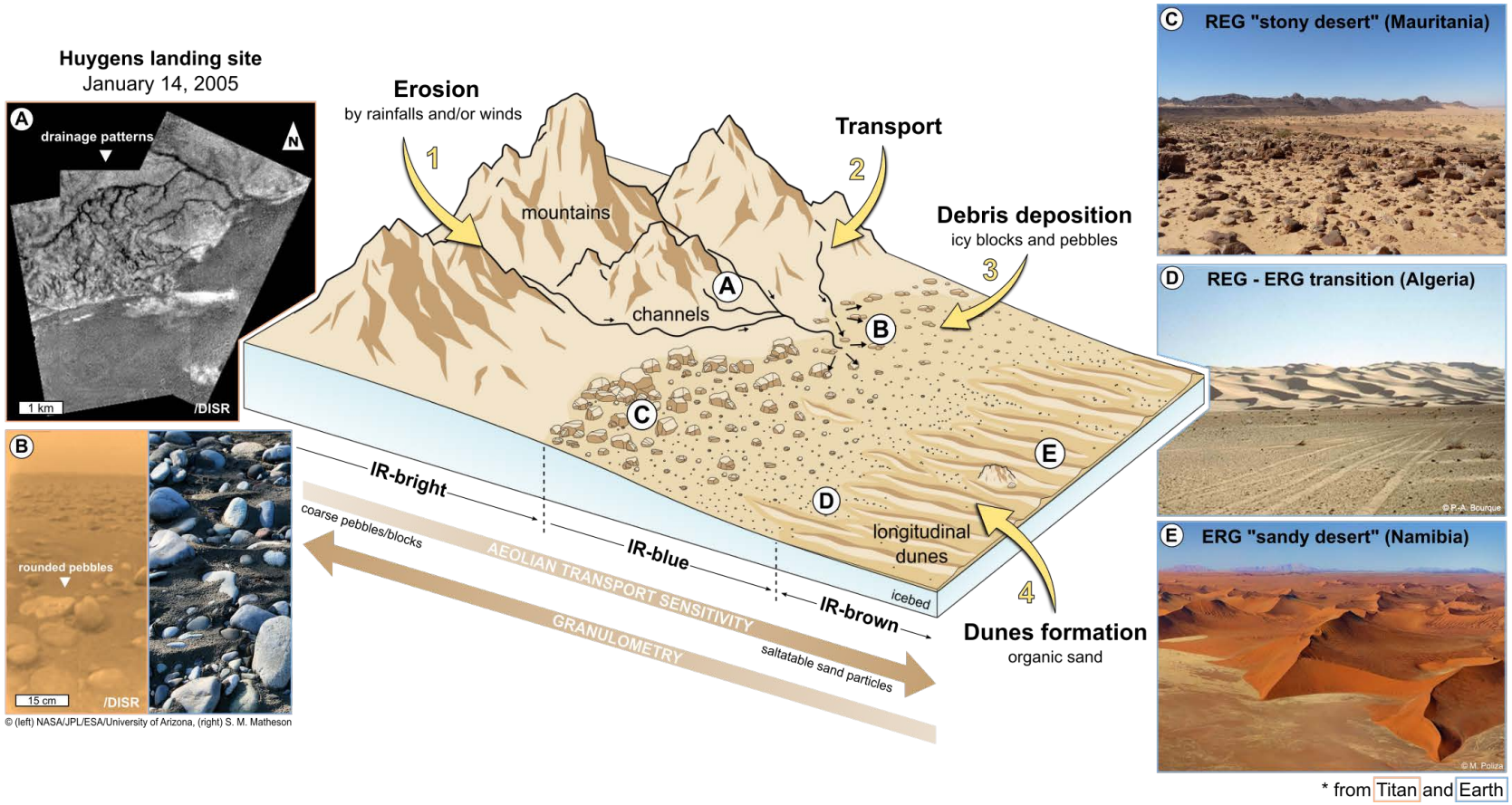

Figure 4.13 – Cartoon model displaying a typical transition between the mountainous/hummocky terrains and dune fields on Titan's equatorial belt (*Brossier et al.*, 2017b). This transition implies similar landscapes than those seen in the hamada-reg-erg transition in Earth's deserts, such as in Namib, Sahara and Egypt. Most of the mountainous and hummocky terrains (SAR-bright, roughest) on Titan are found in IR-bright units, whereas dunes are in good agreement with the IR-brown units. IR-blue units can be considered as transition area where coarser materials (icy blocks, pebbles) are washed out and sorted after fluvial/aeolian erosion of the mountainous terrains.

Chapter 5

CONCLUSIONS

Over these three years of doctoral research, I managed to process thirteen years of imaging data targeting Titan's surface when the Cassini orbiter flew by the moon (2004 – 2017). My work contributes in the extensive investigation of its surface geology. Titan is a frozen version of Earth with surface temperatures 200 degrees colder, and where methane acts as water, water ice may be as hard as rock, and weather cycles last for centuries. Indeed, despite all of its strange properties, Titan exhibits landscapes very familiar to those on Earth, and whose associated processes are likewise analogous to those on our planet. In this chapter, I briefly summarize the main segments of my research and contributions in the survey of Titan's surface geology.

In my first year, I began my research by using a fast semi-empirical technique on infrared observations obtained by VIMS in order to mitigate the atmospheric effects that obstruct the surface of the moon (see Section 2.2). This approach helped me to significantly improve the imaging capacities of the VIMS composites and led me to accurately identify and map the main spectral units present in the equatorial regions of Titan, namely the IR-bright, -blue and -brown units (see Section 4.2). In the meantime, I have integrated and processed the totality of the SAR swaths acquired by Cassini's RADAR in order to produce the most up-to-date global mosaic of Titan's surface, at the wavelength scale of 2.18 cm. This led me to perform a geomorphologic mapping to evaluate the global distribution of the major landscapes identified on the moon, as shown in Section 3.1. The combination of the spectral and geomorphologic maps allowed me to select a few regions located at low latitudes that display an apparent transition in composition and structure that could reveal geologic processes shaping the surface of Titan, such as erosional and depositional processes associated to fluvial and aeolian activities.

During the mapping of Titan's surface, I had the opportunity to identify and request names for a few spectral units (infrared units in VIMS composites) and geomorphologic units (Labyrinth terrains in SAR swaths), which are reported in Table 5.1. Names were

Table 5.1 – Names requested for surface features identified in VIMS and SAR data.

Name	Center latitude	Center longitude	Diameter	Feature	Approval date
Geomorphologic Units (SAR swaths)					
Salusa Labyrinthus	45.6°N	264.2°W	212	Labyrinth terrain	September 14, 2017
Niushe Labyrinthus	74.9°N	88.0°W	244	Labyrinth terrain	September 14, 2017
Harmonthep Labyrinthus	71.1°S	98.2°W	420	Labyrinth terrain	September 14, 2017
Corrin Labyrinthus	66.0°S	31.0°W	273	Labyrinth terrain	September 14, 2017
Infrared Units (VIMS composites)					
Giedi Planitia	5.4°N	356.0°W	375	IR-blue unit	August 24, 2017
Tsiipyia Terra	3.7°N	340.2°W	572	IR-bright unit	August 24, 2017
Ochumare Regio	10.4°N	348.1°W	930	IR-bright unit	September 14, 2017

Note: Diameters are reported in kilometers

requested in March 2017 to the IAU and approved in August and September 2017.

The geomorphologic map clearly displays strong latitudinal distribution of the landscapes, particularly for the polar lakes and equatorial dunes, while the mid-latitudes are dominated by plains. This latitudinal dependency has been suggested to derive from Titan's global weather and climate. Indeed, general circulation modeling (*Rannou et al.*, 2006) predict low humidities at low latitudes, and damp conditions around the poles, consistent with the presence of lakes at the poles (*Stofan et al.*, 2007) and the prevalence of dunes near the equator (*Lorenz et al.*, 2006). Methane rainfall often occurs at the poles while relatively dry, desert-like conditions occur at low latitudes, where the surface is essentially shaped by winds and only occasionally by rainfalls. Interestingly, *Solomonidou et al.* (2018) have found that Titan might describe a latitudinal pattern in the distribution of the surface materials.

Since my objective was to constrain the nature, origin and evolution of the major terrains on Titan, it was essential to evaluate not only the morphology of the moon, but also its surface composition. Hence, I have established a close collaboration with Sébastien Rodriguez starting in the second year of my doctoral research. Through the help of his team, we used a newly updated radiative transfer model which is described in Section 2.2. As explained in Section 4.4, this model was applied on VIMS data targeting the regions of my interest to evaluate the atmospheric effects and retrieve the contribution of the surface for each of the three infrared units identified in VIMS composites and hence their corresponding geomorphologic units seen in SAR swaths. I have limited the compositional analysis to low-latitude regions due to the radiative transfer model limitations at high latitudes (less favorable viewing conditions and low resolution). This is through this collaboration that I got involved in a working group strongly engaged in the retrieval of Titan's surface composition by the application of the radiative transfer code. This led to my participation in a paper recently accepted at JGR Planets (*Solomonidou et al.*, 2018) in addition to my own paper, which is now published in JGR Planets (*Brossier et al.*, 2018).

Furthermore, to complete the compositional analysis, I have compared the surface albedos inferred from the radiative transfer inversion with synthetic mixtures of candidate compounds; water ice that is supposed to form Titan's upper crust (*Tobie et al.*, 2005), and tholin-like solid organics that are photochemically produced in the atmosphere (*Tomasko et al.*, 2008). Due to the presence of the thick and complex atmosphere, which does not allow us to retrieve full spectra and to the difficulty of inferring material characteristics on a surface as sophisticated as Titan's one, we cannot currently provide exact compositions of the selected surface units but rather estimations of the main contributors to their infrared spectra. As presented in Section 4.4, we also evaluated the grain size range for each of the components of the synthetic mixture, and hence gave new valuable insights on the formation and evolution of the infrared units identified in VIMS composites. Thus, this analysis reveals that, in each of them, both water ice and tholins are present, although their stratigraphy and mixing may differ. All the infrared units are being dominated by organics, with a slight enrichment in water ice for the IR-blue unit. The grain size distribution of organics is shifting towards larger sizes from the IR-bright to IR-brown (from about 10 to 200 microns), while that of water ice relatively equivalent from a unit to another (over 800 microns). Putting the spectral properties of the infrared units derived from my compositional analysis together with their geographic and topographic connection, a relatively self-consistent scenario seems to emerge. IR-bright units are therefore interpreted as the source of materials found in both IR-blue units and IR-brown units. The differences in the predicted composition result from differences in mechanical erosion and grain size sorting by alluvial processes, and mixing by aeolian processes. Indeed, the main material covering the IR-bright units (small sized organics) can be transported downward by fluvial processes (numerous IR-blue rivers seen to dissect the IR-bright units seem further support this hypothesis) and can be then blown by the winds to form the dune fields in the lower plains, exactly as on Earth transition areas between oueds, regs and ergs. This seems to be consistent with rivers transporting both blocks of icebed (large water ice grains) and organic fine-grained sediment from the highlands (IR-bright units), where blocks end in the lows (outwash plains associated with the IR-blue units) and organic fine-grained sediment being transported further away and possibly blown away and processed by the winds (enlarging the average grain size by coalescence and sticking) to finally end up in the dune fields (IR-brown units).

Finally, by coupling these two complementary approaches; geomorphologic mapping (see Chapter 3) and compositional analysis (see Chapter 4), I have shown that Titan's low-latitude regions undergo geologic processes very similar to those occurring on terrestrial desertic regions. Indeed, the possible interpretation of the origin of the infrared units and the distribution of surface materials remind the transition from mountainous to stony and sandy deserts in arid regions on Earth (Figure 4.13).

FUTURE WORK(S)

During my investigation and particularly during the review of my paper as first author (*Brossier et al.*, 2018), two major issues were raised by reviewers and members of Cassini's VIMS and RADAR science teams concerning the compositional analysis:

Why only 3 atmospheric windows?

First of all, the radiative transfer model utilized in this study is still under improvement, as explained in *Cornet et al.* (2017b). Among the eight atmospheric windows in VIMS data, only estimations at the 1.27, 1.57 and 2.01 μm-windows are trustable from the radiative transfer model, and hence used in my compositional analysis discussed in Section 4.4. In addition, these three windows are located where much of the spectral variability lies for all infrared units. To date, although haze scattering is much lower relative to shorter wavelengths, there is substantial uncertainty in the spectral properties of the haze, which is particularly poorly known above 2.5 μm, and the methane CH_4 absorption coefficient below 1 μm. Once these properties are known, it would be interesting to include additional atmospheric windows in the analysis to enhance the robustness our results.

Interestingly, Figure B.6 (see Appendix B) shows that the spectra obtained for each regions of interest exhibit a negative slope between 2.7 and 2.8 μm that could indicate the absorption band of water ice at 3 μm, but with a lower magnitude than for pure water ice. Since this spectral characteristic is also shared by the tholins, my collaborators and I favored a possible mixing of water ice and organics (here tholins).

Why only 2 candidate compounds?

My collaborators and I made a starting assumption for the spectral analysis on the candidate materials to be characterized, meaning water ice and tholins. This assumption comes from the fact that Titan is an icy moon, and hence the crust should be mainly made of water ice (e.g. *Tobie et al.*, 2005) that could appear at the surface. Moreover, Titan has a thick atmosphere that produces solid organics, spectrally similar to laboratory tholins, settling down onto the surface over time and ending up in dunes. Thus, this assumption about the composition has been made in several earlier studies and here we have tested this assumption by quantifying the abundance and grain sizes of the components if existing on Titan's surface, as discussed in Section 4.4. Note that numerous atmospheric models have suggested other compounds to be possibly present on Titan's surface (*Lavvas et al.*, 2008a,b; *Krasnopolsky*, 2009, 2014; *Willacy et al.*, 2016). Nonetheless, we do not currently have the optical constants of these materials under the relevant state (solid, liquid ...), temperatures (90 K), and wavelength range (0.9 to 5 microns) to be able to apply the spectral mixing model to those candidates.

Furthermore, a large part of the synthesized components mentioned in the photochemical models is lost to build up larger molecules for which we do not know the exact composition, but for which the laboratory tholins (*Khare et al.*, 1984) provide hitherto the best available analogues. We thus chose to be restrictive with respect to the two candidate materials to limit the inverse problem complexity and because refractive indices of compounds are needed, as explained in Section 2.3. However, it would be interesting to include additional material candidates in future investigations, such as benzene, nitriles (*Clark et al.*, 2010), acetylene (*Singh et al.*, 2016), or a dark absorbent material (*Solomonidou et al.*, 2018).

Bibliography

Aharonson, O., A. G. Hayes, J. I. Lunine, R. D. Lorenz, M. D. Allison, and C. Elachi (2009), An asymmetric distribution of lakes on Titan as a possible consequence of orbital forcing, *Nature Geoscience*, *2*(12), 851 – 854.

Atreya, S. K. (2010), The significance of trace constituents in the solar system, *Faraday Discuss*, *147*, 9 – 29.

Atreya, S. K., E. Y. Adams, H. B. Niemann, J. E. Demick-Montelara, T. C. Owen, M. Fulchignoni, F. Ferri, and E. H. Wilson (2006), Titan's methane cycle, *Planetary and Space Science*, *54*(12), 1177 – 1187.

Barnes, J. W., R. D. Lorenz, J. Radebaugh, A. G. Hayes, K. Arnold, and C. Chandler (2015), Production and global transport of Titan's sand particles, *Planetary Science*, *4*(1), 1 – 19, doi:10.1186/s13535-015-0004-y.

Barnes, J. W., et al. (2007a), Global-scale surface spectral variations on Titan seen from Cassini/VIMS, *Icarus*, *186*(1), 242 – 258, doi:http://dx.doi.org/10.1016/j.icarus.2006.08.021.

Barnes, J. W., et al. (2007b), Near-infrared spectral mapping of Titan's mountains and channels, *Journal of Geophysical Research: Planets*, *112*(E11), doi:10.1029/2007JE002932.

Barnes, J. W., et al. (2008), Spectroscopy, morphometry, and photoclinometry of titan's dunefields from Cassini/VIMS, *Icarus*, *195*(1), 400 – 414, doi:http://doi.org/10.1016/j.icarus.2007.12.006.

Barnes, J. W., et al. (2011a), Organic sedimentary deposits in Titan's dry lakebeds: Probable evaporite, *Icarus*, *216*(1), 136 – 140.

Barnes, J. W., et al. (2011b), Wave constraints for Titan's jingpo lacus and kraken mare from VIMS specular reflection lightcurves, *Icarus*, *211*(1), 722 – 731.

Barnes, J. W., et al. (2014), Cassini/vims observes rough surfaces on titan's punga mare in specular reflection, *Planetary Science*, *3*(1), 3, doi:10.1186/s13535-014-0003-4.

Birch, S. P. D., A. G. Hayes, A. D. Howard, J. M. Moore, and J. Radebaugh (2016b), Alluvial fan morphology, distribution and formation on Titan, *Icarus*, *270*, 238 – 247, doi:http://dx.doi.org/10.1016/j.icarus.2016.02.013.

Birch, S. P. D., A. G. Hayes, P. Corlies, C. Wood, J. I. Lunine, R. Lorenz, M. J. Malaska, R. M. C. Lopes, and the Cassini RADAR team (2017), Morphologic evidence that Titan's southern hemisphere basins are paleoseas, in *the 48th LPSC Abstracts*, p. 2598.

Birch, S. P. D., et al. (2016a), Geomorphologic mapping of Titan's polar terrains: Constraining surface processes and landscape evolution, *Icarus*, *270*, 214 – 236, doi:http://dx.doi.org/10.1016/j.icarus.2016.08.003.

Bishop, B., R. C. Lewis, J. Radebaugh, and E. H. Christiansen (2017), Spatial variations of dune parameters and relationship to elevation and geographic position within the Belet sand sea, in *the 48th LPSC Abstracts*, p. 2425.

Bonnefoy, L. E., A. G. Hayes, P. O. Hayne, M. J. Malaska, A. L. Gall, A. Solomonidou, and A. Lucas (2016), Compositional and spatial variations in Titan dune and interdune regions from Cassini VIMS and RADAR, *Icarus*, *270*, 222 – 237, doi:http://dx.doi.org/10.1016/j.icarus.2015.09.014.

Brassé, C., O. Munoz, P. Coll, and F. Raulin (2015), Optical constants of Titan aerosols and their tholins analogs: Experimental results and modeling/observational data, *Planetary and Space Science*, *109 - 110*, 159 – 174, doi:https://doi.org/10.1016/j.pss.2015.02.012.

Brossier, J. F., K. Stephan, R. Jaumann, S. L. Mouélic, and R. H. Brown (2015), Dark areas on equatorial regions of Titan: Implication in particles size of water-ice and combination with tholins., in *the 48th AGU Fall Meeting Abstracts*.

Brossier, J. F., S. Rodriguez, L. Maltagliati, S. L. Mouélic, A. Solomonidou, A. Coustenis, M. Hirtzig, R. Jaumann, and R. H. Brown (2016a), Characterization of the Titan's VIMS - units: Using spectral slopes, in *the 13th EGU General Assembly Abstracts*, p. 3821.

Brossier, J. F., S. Rodriguez, L. Maltagliati, S. L. Mouélic, A. Solomonidou, A. Coustenis, M. Hirtzig, R. Jaumann, and R. H. Brown (2016b), Equatorial belt of Titan: Aaru Region as seen by VIMS/Cassini, in *the 48th DPS Meeting/ 11th EPSC Abstracts*, p. 412.06.

Brossier, J. F., et al. (2017a), Equatorial belt of Titan revisited unsing a comprehensive radiative tranfer model, in *the 48th LPSC Abstracts*, p. 1399.

Brossier, J. F., et al. (2017b), Constraining the composition and geological history of the main types of terrains found in the equatorial belt of Titan, in *the 12th EPSC Abstracts*, p. 88.

Brossier, J. F., et al. (2018), Geological evolution of titan's equatorial regions: Possible nature and origin of the dune material, *Journal of Geophysical Research: Planets*, *123*(5), 1089 – 1112, doi:https://doi.org/10.1029/2017JE005399.

Brown, R. H., and D. P. Cruikshank (1997), Determination of the composition and state of icy surfaces in the outer Solar System 1, *Annual Review of Earth and Planetary Sciences*, *25*(1), 243 – 277.

Brown, R. H., et al. (2004), The Cassini Visual and Infrared Mapping Spectrometer VIMS investigation, in *The Cassini - Huygens Mission*, edited by C. Russell, pp. 111 – 168, Springer Netherlands, doi:10.1007/1-4020-3874-7_3.

Brown, R. H., et al. (2008), The identification of liquid ethane in Titan's Ontario Lacus, *Nature*, *454*(7204), 607 – 610.

Buratti, B. J., et al. (2012), A newly discovered impact crater in Titan's Senkyo: Cassini VIMS observations and comparison with other impact features, *Planetary and Space Science*, *60*(1), 18 – 25, doi:http://dx.doi.org/10.1016/j.pss.2011.05.004.

Burr, D. M., R. E. Jacobsen, D. L. Roth, C. B. Phillips, K. L. Mitchell, and D. Viola (2009), Fluvial network analysis on Titan: Evidence for subsurface structures and west-to-east wind flow, southwestern Xanadu, *Geophysical Research Letters*, *36*(22), doi:10.1029/2009GL040909.

Burr, D. M., S. A. Drummond, R. Cartwright, B. A. Black, and J. T. Perron (2013), Morphology of fluvial networks on Titan: Evidence for structural control, *Icarus*, *226*(1), 742 – 759, doi:http://doi.org/10.1016/j.icarus.2013.06.016.

Burr, D. M., N. T. Bridges, J. R. Marshall, J. K. Smith, and E. J. P. White, B. R. (2015), Higher-than-predicted saltation threshold wind speeds on Titan, *Nature*, *517*, 60–63, doi:10.1038/nature14088.

Cable, M. L., S. M. Horst, R. Hodyss, P. M. Beauchamp, M. A. Smith, and P. A. Willis (2012), Titan Tholins: Simulating Titan organic chemistry in the Cassini-Huygens era, *Chemical Reviews*, *112*(3), 1882–1909, doi:10.1021/cr200221x.

Charnay, B., E. Barth, S. Rafkin, C. Narteau, S. Lebonnois, S. Rodriguez, S. Courrech du Pont, and A. Lucas (2015), Methane storms as a driver of Titan's dune orientation, *Nature Geoscience*, *8*(5), 362 – 366.

Choukroun, M., and C. Sotin (2012), Is Titan's shape caused by its meteorology and carbon cycle?, *Geophysical Research Letters*, *39*(4), doi:http://dx.doi.org/10.1029/2011GL050747.

Clark, R. N., et al. (2010), Detection and mapping of hydrocarbon deposits on Titan, *J. Geophys. Res.*, *115*(E10), E10,005, doi:http://doi.org/10.1029/2009JE003369.

Collins, G. C. (2005), Relative rates of fluvial bedrock incision on Titan and Earth, *Geophysical Research Letters*, *32*(22), L22,202, doi:10.1029/2005GL024551.

Combes, M., L. Vapillon, E. Gendron, A. Coustenis, O. Lai, R. Wittemberg, and R. Sirdey (1997), Spatially resolved images of Titan by means of adaptive optics, *Icarus*, *129*(2), 482 – 497.

Cornet, T. (2012b), Formation et développement des lacs de Titan: Interprétation géomorphologique d'Ontario Lacus et analogues terrestres, Ph.D. thesis, Université de Nantes, UFR Sciences et Techniques.

Cornet, T., D. Cordier, T. L. Bahers, O. Bourgeois, C. Fleurant, S. L. Mouélic, and N. Altobelli (2015), Dissolution on Titan and on Earth: Toward the age of Titan's karstic landscapes, *Journal of Geophysical Research: Planets*, *120*(6), 1044 – 1074, doi: 10.1002/2014JE004738.

Cornet, T., C. Fleurant, B. Seignovert, D. Cordier, O. Bourgeois, S. Le Mouélic, S. Rodriguez, and A. Lucas (2017a), Landscape formation through dissolution on Titan: a 3D landscape evolution model, in *the 48th LPSC Abstracts*, p. 1835.

Cornet, T., et al. (2012a), Geomorphological significance of Ontario Lacus on Titan: Integrated interpretation of Cassini VIMS, ISS and RADAR data and comparison with the Etosha Pan (Namibia), *Icarus*, *218*(2), 788 – 806, doi:http://doi.org/10.1016/j.icarus.2012.01.013.

Cornet, T., et al. (2017b), Radiative transfer modelling in Titan's atmosphere: Application to Cassini/VIMS data, in *the 48th LPSC Abstracts*, p. 1847.

Coustenis, A., and B. Bézard (1995a), Titan's atmosphere from voyager infrared observations: IV. latitudinal variations of temperature and composition., *Icarus*, *115*(1), 126 – 140.

Coustenis, A., E. Lellouch, J. P. Maillard, and C. P. McKay (1995b), Titan's surface: Composition and variability from the near-infrared albedo, *Icarus*, *118*, 87–104.

Coustenis, A., M. Hirtzig, E. Gendron, P. Drossart, O. Lai, M. Combes, and A. Negrao (2005), Maps of Titan's surface from 1 to 2.5 microns, *Icarus*, *177*(1), 89 – 105, doi: http://dx.doi.org/10.1016/j.icarus.2005.03.012.

Coustenis, A., et al. (2001), Images of Titan at 1.3 and 1.6 microns with adaptive optics at the CFHT, *Icarus*, *154*(2), 501 – 515, doi:http://dx.doi.org/10.1006/icar.2001.6643.

Danielson, R. E., J. J. Caldwell, and D. R. Larach (1973), An inversion in the atmosphere of Titan, *Icarus*, *20*(4), 437 – 443.

de Kok, R., et al. (2007), Oxygen compounds in Titan's stratosphere as observed by Cassini CIRS, *Icarus*, *186*(2), 354 – 363, doi:http://dx.doi.org/10.1016/j.icarus.2006.09.016.

Doose, L. R., E. Karkoschka, M. G. Tomasko, and C. M. Anderson (2016), Vertical structure and optical properties of Titan's aerosols from radiance measurements made inside and outside the atmosphere, *Icarus*, *270*, 355 – 375, doi:http://dx.doi.org/10.1016/j.icarus.2015.09.039.

Elachi, C., et al. (2004), RADAR: The Cassini Titan radar mapper, *Space Science Reviews*, *115*(1-4), 71–110, doi:10.1007/s11214-004-1438-9.

Elachi, C., et al. (2005), Cassini RADAR views the surface of Titan, *Science*, *308*(5724), 970 – 974.

Elachi, C., et al. (2006), Titan Radar Mapper observations from Cassini's T3 fly-by, *Nature*, *441*, 709 – 713, doi:10.1038/nature04786.

Engel, S., J. I. Lunine, and W. K. Hartmann (1995), Cratering on Titan and implications for Titan's atmospheric history, *Planetary and Space Science*, *43*(9), 1059 – 1066, doi:http://dx.doi.org/10.1016/0032-0633(95)00044-6.

Evans, K. F. (2007), SHDOMPPDA: A Radiative Transfer Model for Cloudy Sky Data Assimilation, *Journal of the Atmospheric Sciences*, *64*(11), 3854 – 3864, doi:http://dx.doi.org/10.1175/2006JAS2047.1.

Ewing, R. C., A. G. Hayes, and A. Lucas (2015), Sand dune patterns on Titan controlled by long-term climate cycles, *Nature Geoscience*, *8*(1), 15 – 19, doi:http://dx.doi.org/10.1038/ngeo2323.

Flasar, F. M. (1983), Oceans on Titan?, *Science*, *221*(4605), 55–57, doi:10.1126/science.221.4605.55.

Fortes, A. (2012), Titan's internal structure and the evolutionary consequences, *Planetary and Space Science*, *60*(1), 10 – 17.

Fulchignoni, M., et al. (2005), In situ measurements of the physical characteristics of Titan's environment, *Nature*, *438*(7069), 785 – 791, doi:10.1038/nature04314.

Gillett, F. C. (1975), Further observations of the 8-13 microns spectrum of Titan, *Astrophysical Journal*, *201*, L41 – L43.

Gillett, F. C., W. J. Forrest, and K. M. Merrill (1973), 8-13 microns observations of Titan, *Astrophysical Journal*, *184*, L93 – L95.

Griffith, C. A., T. Owen, and R. Wagener (1991), Titan's surface and troposphere, investigated with ground-based, near-infrared observations, *Icarus*, *93*(2), 362 – 378.

Griffith, C. A., T. Owen, T. R. Geballe, J. Rayner, and P. Rannou (2003), Evidence for the exposure of water ice on Titan's surface, *Science*, *300*(5619), 628 – 630.

Griffith, C. A., J. M. Lora, J. Turner, P. F. Penteado, R. H. Brown, M. G. Tomasko, L. Doose, and C. See (2012), Possible tropical lakes on Titan from observations of dark terrain, *Nature*, *486*, 237 – 239.

Grundy, W. M., and B. Schmitt (1998), The temperature-dependent near-infrared absorption spectrum of hexagonal H2O ice, *Journal of Geophysical Research: Planets*, *103*(E11), 25,809–25,822, doi:10.1029/98JE00738.

Hanel, R., et al. (1981), Infrared observations of the Saturnian system from Voyager 1, *Science*, *212*(4491), 192 – 200.

Hapke, B. (2012), Theory of reflectance and emittance spectroscopy, Topics in Remote Sensing, p. 513, 2nd ed. Cambridge University Press, doi:https://dx.doi.org/10.1017/CBO9781139025683.

Hartung, M., T. M. Herbst, C. Dumas, and A. Coustenis (2006), Limits to the abundance of surface CO2 ice on Titan, *Journal of Geophysical Research: Planets*, *111*(E7), doi:http://dx.doi.org/10.1029/2005JE002642.

Hayes, A. G. (2016), The lakes and seas of Titan, *Annual Review of Earth and Planetary Sciences*, *44*(1), 57 – 83, doi:10.1146/annurev-earth-060115-012247.

Hayes, A. G., et al. (2008), Hydrocarbon lakes on Titan: Distribution and interaction with an isotropic porous regolith, *Geophysical Research Letters*, *35*, L09,204.

Hayes, A. G., et al. (2011), Transient surface liquid in Titan's polar regions from Cassini, *Icarus*, *211*(1), 655–671.

Hirtzig, M., A. Coustenis, O. Lai, E. Emsellem, A. Pecontal-Rousset, P. Rannou, A. Negrao, and B. Schmitt (2005), Near-infrared study of Titan's resolved disk in spectro-imaging with CFHT/OASIS, *Planetary and Space Science*, *53*(5), 535 – 556, doi:http://dx.doi.org/10.1016/j.pss.2004.08.006.

Hirtzig, M., et al. (2013), Titan's surface and atmosphere from Cassini/VIMS data with updated methane opacity, *Icarus*, *226*(1), 470 – 486, doi:http://doi.org/10.1016/j.icarus.2013.05.033.

Hofgartner, J. D., B. J. Buratti, R. H. Brown, J. W. Barnes, C. Sotin, and K. Lawrence (2016), Erosion of Titan's craters from Cassini/RADAR and VIMS imagery, in *the 47th LPSC Abstracts*, p. 2591.

Janssen, M. A., et al. (2009), Titan's surface at 2.2-cm wavelength imaged by the Cassini RADAR radiometer: Calibration and first results, *Icarus*, *200*, 222 – 239, doi:http://doi.org/10.1016/j.icarus.2008.10.017.

Janssen, M. A., et al. (2016), Titan's surface at 2.18-cm wavelength imaged by the cassini {RADAR} radiometer: Results and interpretations through the first ten years of observation, *Icarus*, *270*, 443 – 459, doi:http://dx.doi.org/10.1016/j.icarus.2015.09.027.

Jaumann, R., et al. (2006), High-resolution Cassini-VIMS mosaics of Titan and the icy Saturnian satellites, *Planetary and Space Science*, *54*(12), 1146 – 1155, doi:http://dx.doi.org/10.1016/j.pss.2006.05.034.

Jaumann, R., et al. (2008), Fluvial erosion and post-erosional processes on Titan, *Icarus*, *197*(2), 526 – 538, doi:http://dx.doi.org/10.1016/j.icarus.2008.06.002.

Jaumann, R., et al. (2009), Geology and surface processes on Titan, in *Titan from Cassini-Huygens*, edited by R. H. Brown, J.-P. Lebreton, and J. H. Waite, pp. 75 – 140, Springer Netherlands, doi:10.1007/978-1-4020-9215-2_5.

Khare, B. N., and C. Sagan (1973), Red clouds in reducing atmospheres, *Icarus*, *20*(3), 311 – 321.

Khare, B. N., C. Sagan, E. T. Arakawa, F. Suits, T. A. Callcott, and M. W. Williams (1984), Optical constants of organic tholins produced in a simulated Titanian atmosphere: From soft x-ray to microwave frequencies, *Icarus*, *60*(1), 127 – 137, doi:http://dx.doi.org/10.1016/0019-1035(84)90142-8.

Kirk, R. L., et al. (2010), La Sotra y las otras: Topographic evidence for (and against) cryovolcanism on Titan (Invited), *the 43th AGU Fall Meeting Abstracts*.

Krasnopolsky, V. A. (2009), A photochemical model of Titan's atmosphere and ionosphere, *Icarus*, *201*(1), 226 – 256.

Krasnopolsky, V. A. (2014), Chemical composition of Titan's atmosphere and ionosphere: Observations and the photochemical model, *Icarus*, *236*, 83 – 91, doi:http://dx.doi.org/10.1016/j.icarus.2014.03.041.

Langhans, M., J. I. Lunine, and G. Mitri (2013), Titan's Xanadu region: Geomorphology and formation scenario, *Icarus*, *223*(2), 796 – 803, doi:http://doi.org/10.1016/j.icarus.2013.01.016.

Langhans, M., et al. (2012), Titan's fluvial valleys: Morphology, distribution, and spectral properties, *Planetary and Space Science*, *60*(1), 34 – 51, doi:http://doi.org/10.1016/j.pss.2011.01.020.

Lavvas, P., A. Coustenis, and I. Vardavas (2008a), Coupling photochemistry with haze formation in Titan's atmosphere, Part 1: Model description, *Planetary and Space Science*, *56*(1), 27 – 66, doi:http://dx.doi.org/10.1016/j.pss.2007.05.026.

Lavvas, P., A. Coustenis, and I. Vardavas (2008b), Coupling photochemistry with haze formation in Titan's atmosphere, Part 2: Results and validation with Cassini/Huygens data, *Planetary and Space Science*, *56*(1), 67 – 99, doi:http://dx.doi.org/10.1016/j.pss.2007.05.027.

Le Corre, L., et al. (2009), Analysis of a cryolava flow-like feature on Titan, *Planetary and Space Science*, *57*(7), 870 – 879, doi:https://doi.org/10.1016/j.pss.2009.03.005.

Le Gall, A., M. Janssen, P. Paillou, R. Lorenz, and S. Wall (2010), Radar-bright channels on Titan, *Icarus*, *207*(2), 948 – 958, doi:http://dx.doi.org/10.1016/j.icarus.2009.12.027.

Le Gall, A., A. G. Hayes, R. Ewing, M. A. Janssen, J. Radebaugh, C. Savage, and P. Encrenaz (2012), Latitudinal and altitudinal controls of Titan's dune field morphometry, *Icarus*, *217*(1), 231 – 242, doi:http://dx.doi.org/10.1016/j.icarus.2011.10.024.

Le Gall, A., et al. (2011), Cassini SAR, radiometry, scatterometry and altimetry observations of Titan's dune fields, *Icarus*, *213*(2), 608 – 624.

Le Mouélic, S., et al. (2008), Mapping and interpretation of sinlap crater on Titan using Cassini VIMS and RADAR data, *Journal of Geophysical Research: Planets*, *113*(E4), doi:10.1029/2007JE002965.

Le Mouélic, S., et al. (2010), Imaging of Titan in the infrared with Cassini VIMS: Toward homogeneous surface maps, in *the 7th EGU General Assembly Abstracts*, vol. 12, pp. EGU2010–8483.

Le Mouélic, S., et al. (2012), Global mapping of Titan's surface using an empirical processing method for the atmospheric and photometric correction of Cassini/VIMS images, *Planetary and Space Science*, *73*(1), 178 – 190, doi:http://doi.org/10.1016/j.pss.2012.09.008.

Le Mouélic, S., et al. (2016), Producing seamless global mosaics of Titan with the VIMS imaging spectrometer, in *the 47th LPSC Abstracts*.

Lemmon, M. T., E. Karkoschka, and M. G. Tomasko (1993), Titan's rotation: Surface feature observed, *Icarus*, *103*(2), 329 – 332, doi:http://dx.doi.org/10.1006/icar.1993.1074.

Lewis, R. C., B. Bishop, J. Radebaugh, and E. H. Christiansen (2017), A comparative analysis of sediment transport and deposition trends of the sand seas of Earth and Titan, in *the 48th LPSC Abstracts*, p. 2559.

Lindal, G., G. Wood, H. Hotz, D. Sweetnam, V. Eshleman, and G. Tyler (1983), The atmosphere of Titan: An analysis of the voyager 1 radio occultation measurements, *Icarus*, *53*(2), 348 – 363.

Lopes, R. M., et al. (2007a), Much like Earth: Distribution and interplay of geologic processes on Titan from Cassini RADAR data, pp. 78 – 79.

Lopes, R. M., et al. (2007b), The lakes and seas of Titan, *Eos, Transactions American Geophysical Union*, *88*(51), 569 – 570, doi:10.1029/2007EO510001.

Lopes, R. M., et al. (2010), Distribution and interplay of geologic processes on Titan from Cassini RADAR data, *Icarus*, *205*(2), 540 – 558.

Lopes, R. M., et al. (2013), Cryovolcanism on Titan: New results from Cassini RADAR and VIMS, *Journal of Geophysical Research: Planets*, *118*(3), 416 – 435, doi:10.1002/jgre.20062.

Lopes, R. M., et al. (2016), Nature, distribution, and origin of Titan's Undifferentiated Plains, *Icarus*, *270*, 162 – 182, doi:http://dx.doi.org/10.1016/j.icarus.2015.11.034.

Lorenz, R. D. (2014), Physics of saltation and sand transport on Titan: A brief review, *Icarus*, *230*, 162 – 167, doi:http://dx.doi.org/10.1016/j.icarus.2013.06.023.

Lorenz, R. D., and J. Radebaugh (2009), Global pattern of Titan's dunes: radar survey from the Cassini prime mission, *Geophysical Research Letters*, *36*(3).

Lorenz, R. D., et al. (2006), The sand seas of Titan: Cassini RADAR observations of longitudinal dunes, *Science*, *312*(5774), 724–727, doi:10.1126/science.1123257.

Lorenz, R. D., et al. (2007), Titan's young surface: Initial impact crater survey by Cassini RADAR and model comparison, *Geophysical Research Letters*, *34*(7), L07,204.

Lorenz, R. D., et al. (2008), Fluvial channels on Titan: Initial Cassini RADAR observations, *Planetary and Space Science*, *56*(8), 1132 – 1144, doi:http://dx.doi.org/10.1016/j.pss.2008.02.009.

Lucas, A., O. Aharonson, C. Deledalle, A. G. Hayes, R. L. Kirk, and E. Howington-Kraus (2014a), Insights into Titan's geology and hydrology based on enhanced image processing of Cassini RADAR data, *Journal of Geophysical Research: Planets*, *119*, 2149 – 2166, doi:doi:10.1002/2013JE004584.

Lucas, A., S. Rodriguez, F. Lemonnier, A. Le Gall, C. Ferrari, P. Paillou, and C. Narteau (2017), Texture and composition of Titan's equatorial region inferred from Cassini SAR inversion: Implications for aeolian transport at Saturn's largest moon, *ArXiv e-prints*.

Lucas, A., et al. (2014b), Growth mechanisms and dune orientation on Titan, *Geophysical Research Letters*, *41*(17), 6093 – 6100, doi:10.1002/2014GL060971.

Lunine, J. I., and R. D. Lorenz (2009), Rivers, lakes, dunes, and rain: Crustal processes in Titan's methane cycle, *Annual Review of Earth and Planetary Sciences*, *37*(1), 299–320, doi:10.1146/annurev.earth.031208.100142.

Lunine, J. I., D. J. Stevenson, and Y. L. Yung (1983), Ethane Ocean on Titan, *Science*, *222*(4629), 1229 – 1230, doi:10.1126/science.222.4629.1229.

Lunine, J. I., et al. (2008), Titan's diverse landscapes as evidenced by Cassini RADAR's third and fourth looks at Titan, *Icarus*, *195*(1), 415–433, doi:10.1016/j.icarus.2007.12.022.

MacKenzie, S. M., and J. W. Barnes (2016), Compositional similarities and distinctions between Titan's evaporitic terrains, *Astrophysical Journal*, *821*(1), 17, doi:http://dx.doi.org/10.3847/0004-637X/821/1/17.

MacKenzie, S. M., et al. (2014), Evidence of Titan's climate history from evaporite distribution, *Icarus*, *243*, 191 – 207, doi:http://dx.doi.org/10.1016/j.icarus.2014.08.022.

Malaska, M. J., J. Radebaugh, R. Lorenz, K. Mitchell, T. Farr, and E. R. Stofan (2010), Identification of karst-like terrain on Titan from valley analysis, in *the 41st LPIS Abstracts*, pp. 1544–1545.

Malaska, M. J., J. Radebaugh, R. M. Lopes, K. L. Mitchell, A. G. Hayes, A. L. Gall, E. Turtle, A. Solomonidou, and R. Lorenz (2014), Labyrinth terrain on Titan, in *the 126th GSA Annual Meeting Abstracts*.

Malaska, M. J., R. M. Lopes, A. G. Hayes, J. Radebaugh, R. D. Lorenz, and E. P. Turtle (2016b), Material transport map of Titan: The fate of dunes, *Icarus*, *270*, 183 – 196, doi:http://dx.doi.org/10.1016/j.icarus.2015.09.029.

Malaska, M. J., et al. (2016a), Geomorphological map of the Afekan Crater region, Titan: Terrain relationships in the equatorial and mid-latitude regions, *Icarus*, *270*, 130 – 161, doi:10.1016/j.icarus.2016.02.021.

Maltagliati, L., S. Rodriguez, C. Sotin, T. Cornet, P. Rannou, S. Le Mouélic, A. Solomonidou, A. Coustenis, and R. H. Brown (2015), Simultaneous mapping of Titan's surface albedo and aerosol opacity from Cassini/VIMS massive inversion, in *the 10th EPSC Abstracts*, pp. EPSC2015–687.

Mastrogiuseppe, M., V. Poggiali, R. Seu, R. Martufi, and C. Notarnicola (2014), Titan dune heights retrieval by using Cassini Radar Altimeter, *Icarus*, *230*, 191 – 197, doi:http://dx.doi.org/10.1016/j.icarus.2013.09.028.

Mastrogiuseppe, M., A. G. Hayes, V. Poggiali, R. Seu, J. I. Lunine, and J. D. Hofgartner (2016a), Radar sounding using the Cassini Altimeter: Waveform modeling and Monte Carlo approach for data inversion of observations of Titan's seas, *IEEE Transactions on Geoscience and Remote Sensing*, *54*(10), 5646 – 5656, doi:10.1109/TGRS.2016.2563426.

Mastrogiuseppe, M., et al. (2016b), Bathymetry and composition of Titan's Ontario Lacus derived from Monte Carlo-based waveform inversion of Cassini RADAR altimetry data, *Icarus*, *300*, 203 – 209, doi:http://dx.doi.org/10.1016/j.icarus.2017.09.009.

McCord, T. B., et al. (2006), Composition of Titan's surface from Cassini VIMS, *Planetary and Space Science*, *54*(15), 1524 – 1539, doi:http://doi.org/10.1016/j.pss.2006.06.007.

McCord, T. B., et al. (2008), Titan's surface: Search for spectral diversity and composition using the Cassini VIMS investigation, *Icarus*, *194*(1), 212 – 242, doi:http://dx.doi.org/10.1016/j.icarus.2007.08.039.

Mitchell, K. L., et al. (2007), Titan's north polar lakes as observed by Cassini Radar: An update, p. 6042.

Mitri, G., A. P. Showman, J. I. Lunine, and R. D. Lorenz (2007), Hydrocarbon lakes on Titan, *Icarus*, *186*(2), 385–394.

Mitri, G., A. P. Showman, J. I. Lunine, and R. M. Lopes (2008), Resurfacing of Titan by ammonia-water cryomagma, *Icarus*, *196*(1), 216 – 224, doi:http://dx.doi.org/10.1016/j.icarus.2008.02.024.

Moore, J. M., A. D. Howard, and A. M. Morgan (2014), The landscape of Titan as witness to its climate evolution, *Journal of Geophysical Research: Planets*, *119*(9), doi:10.1002/2014JE004608.

Mustard, J. F., and J. M. Sunshine (1999), Spectral analysis for earth science: Investigation using remote sensing data, in *Remote sensing for Earth Sciences: Manual of Remote Sensing*, vol. 3, edited by A. M. Rencz, 3rd ed., Wiley & Sons.

Negrao, A., A. Coustenis, E. Lellouch, J.-P. Maillard, P. Rannou, B. Schmitt, C. McKay, and V. Boudon (2006), Titan's surface albedo variations over a Titan season from near-infrared CFHT/FTS spectra, *Planetary and Space Science*, *54*(12), 1225 – 1246, doi:http://dx.doi.org/10.1016/j.pss.2006.05.031.

Neish, C. D., and R. D. Lorenz (2012), Titan's global crater population: A new assessment, *Planetary and Space Science*, *60*(1), 26 – 33.

Neish, C. D., R. D. Lorenz, R. L. Kirk, and L. C. Wye (2010), Radarclinometry of the sand seas of Africa's Namibia and Saturn's moon Titan, *Icarus*, *208*(1), 385 – 394, doi:http://dx.doi.org/10.1016/j.icarus.2010.01.023.

Neish, C. D., et al. (2015), Spectral properties of Titan's impact craters imply chemical weathering of its surface, *Geophysical Research Letters*, *42*(10), 3746 – 3754, doi:10.1002/2015GL063824.

Niemann, H. B., et al. (2010), Composition of Titan's lower atmosphere and simple surface volatiles as measured by the Cassini-Huygens probe gas chromatograph mass spectrometer experiment, *Journal of Geophysical Research*, *115*(E12), E12,006.

Paganelli, F., et al. (2008), Titan's surface from the Cassini RADAR radiometry data during SAR mode, *Planetary and Space Science*, *56*(1), 100 – 108, doi:http://dx.doi.org/10.1016/j.pss.2007.03.015.

Paillou, P., B. Seignovert, J. Radebaugh, and S. D. Wall (2016), Radar scattering of linear dunes and mega-yardangs: Application to Titan, *Icarus*, *270*, 211 – 221, doi:http://dx.doi.org/10.1016/j.icarus.2015.07.038.

Perron, J. T., M. P. Lamb, C. D. Koven, I. Y. Fung, E. Yager, and M. Ádámkovics (2006), Valley formation and methane precipitation rates on Titan, *Journal of Geophysical Research: Planets*, *111*(E11), doi:10.1029/2005JE002602.

Perry, J. E., A. S. McEwen, S. Fussner, E. P. Turtle, R. A. West, C. C. Porco, B. Knowles, D. D. Dawson, and the Cassini ISS Team (2005), Processing ISS images of Titan's surface, in *the 36th LPSC Abstracts*, p. 2312.

Porco, C. C., et al. (2004), Cassini imaging science: Instrument characteristics and anticipated scientific investigations at Saturn, *Space Science Reviews*, *115*(1-4), 363–497, doi:10.1007/s11214-004-1456-7.

Porco, C. C., et al. (2005), Imaging of Titan from the Cassini spacecraft, *Nature*, *434*(7030), 159 – 168.

Radebaugh, J. (2013), Dunes on Saturn's moon Titan as revealed by the Cassini mission, *Aeolian Research*, *11*, 23 – 41.

Radebaugh, J., R. D. Lorenz, R. L. Kirk, J. I. Lunine, E. R. Stofan, R. M. C. Lopes, and S. D. Wall (2007), Mountains on Titan observed by Cassini Radar, *Icarus*, *192*(1), 77 – 91, doi:http://dx.doi.org/10.1016/j.icarus.2007.06.020.

Radebaugh, J., R. Lorenz, T. Farr, P. Paillou, C. Savage, and C. Spencer (2010), Linear dunes on Titan and Earth: Initial remote sensing comparisons, *Geomorphology*, *121*(1 - 2), 122 – 132, doi:http://dx.doi.org/10.1016/j.geomorph.2009.02.022.

Radebaugh, J., A. Le Gall, J. W. Barnes, R. D. Lorenz, J. I. Lunine, R. L. Kirk, and Cassini RADAR Team (2012), Stabilized Dunes on Titan Indicate Changes in Climate and Surface Processes, in *the 43rd LPSC Abstracts*, p. 2224.

Radebaugh, J., et al. (2008), Dunes on Titan observed by Cassini Radar, *Icarus*, *194*(2), 690 – 703, doi:http://dx.doi.org/10.1016/j.icarus.2007.10.015.

Radebaugh, J., et al. (2011), Regional geomorphology and history of Titan's Xanadu province, *Icarus*, *211*(1), 672 – 685.

Radebaugh, J., et al. (2016), Alluvial and fluvial fans on Saturn's moon Titan reveal processes, materials and regional geology, *Geology Society, London, Special Publication*, *440*.

Rannou, P., F. Montmessin, F. Hourdin, and S. Lebonnois (2006), The latitudinal distribution of clouds on Titan, *Science*, *311*(5758), 201 – 205.

Rannou, P., D. Toledo, P. Lavvas, E. D'Aversa, M. L. Moriconi, A. Adriani, S. Le Mouélic, C. Sotin, and R. H. Brown (2016), Titan's surface spectra at the Huygens landing site and Shangri-La, *Icarus*, *270*, 291 – 306.

Raulin, F. (2008), Planetary Sciences: Organic lakes on Titan, *Nature*, *454*, 587 – 589, doi:http://dx.doi.org/10.1038/454587a.

Rodriguez, S., et al. (2006), Cassini/VIMS hyperspectral observations of the Huygens landing site on Titan, *Planetary and Space Science*, *54*(15), 1510 – 1523, doi:http://doi.org/10.1016/j.pss.2006.06.016.

Rodriguez, S., et al. (2014), Global mapping and characterization of Titan's dune fields with Cassini: Correlation between RADAR and VIMS observations, *Icarus*, *230*, 168 – 179, doi:http://doi.org/10.1016/j.icarus.2013.11.017.

Sagan, C. (1971), The solar system beyond Mars: An exobiological survey, *Space Science Reviews*, *11*, 827 – 866.

Sagan, C., and B. N. Khare (1979), Tholins : organic chemistry of interstellar grains and gas, *Nature*, *277*(5692), 102 – 107.

Savage, C. J., J. Radebaugh, E. H. Christiansen, and R. D. Lorenz (2014), Implications of dune pattern analysis for Titan's surface history, *Icarus*, *230*, 180 – 190, doi:http://doi.org/10.1016/j.icarus.2013.08.009.

Schroeder, S. E., and H. U. Keller (2008), The reflectance spectrum of Titan's surface at the Huygens landing site determined by the descent imager/spectral radiometer, *Planetary and Space Science*, *56*(5), 753 – 769, doi:http://dx.doi.org/10.1016/j.pss.2007.10.011.

Schroeder, S. E., E. Karkoschka, and R. D. Lorenz (2012), Bouncing on Titan: Motion of the Huygens probe in the seconds after landing, *Planetary and Space Science*, *73*, 327 – 340.

Singh, S., T. Cornet, V. F. Chevrier, J. P. Combe, T. B. McCord, L. A. Roe, S. Le Mouélic, E. Le Menn, and F. C. Wasiak (2016), Near-infrared spectra of liquid/solid acetylene under Titan relevant conditions and implications for Cassini/VIMS detections, *Icarus*, *270*, 429 – 434, doi:http://dx.doi.org/10.1016/j.icarus.2015.11.002.

Soderblom, J. M., et al. (2010), Geology of the Selk crater region on Titan from Cassini VIMS observations, *Icarus*, *208*(2), 905 – 912, doi:http://doi.org/10.1016/j.icarus.2010.03.001.

Soderblom, J. M., et al. (2012), Modeling specular reflections from hydrocarbons lakes on Titan, *Icarus*, *220*(2), 744 – 751, doi:http://doi.org/10.1016/j.icarus.2012.05.030.

Soderblom, L. A., et al. (2007a), Correlations between Cassini VIMS spectra and RADAR and SAR images: Implications for Titan's surface composition and the character of the Huygens probe landing site, *Planetary and Space Science*, *55*(13), 2025 – 2036, doi:http://dx.doi.org/10.1016/j.pss.2007.04.014.

Soderblom, L. A., et al. (2007b), Topography and geomorphology of the Huygens landing site on Titan, *Planetary and Space Science*, *55*(13), 2015 – 2024, doi:http://dx.doi.org/10.1016/j.pss.2007.04.015.

Sohl, F., W. D. Sears, and R. D. Lorenz (1995), Tidal Dissipation on Titan, *Icarus*, *115*(2), 278 – 294.

Solomonidou, A., G. Bampasidis, M. Hirtzig, A. Coustenis, K. Kyriakopoulos, K. S. Seymour, E. Bratsolis, and X. Moussas (2013), Morphotectonic features on Titan and their possible origin, *Planetary and Space Science*, *77*(0), 104 – 117, doi:http://dx.doi.org/10.1016/j.pss.2012.05.003.

Solomonidou, A., et al. (2014), Surface albedo spectral properties of geologically interesting areas on Titan, *Journal of Geophysical Research: Planets*, *119*(8), 1729 – 1747, doi:10.1002/2014JE004634.

Solomonidou, A., et al. (2016), Temporal variations of Titan's surface with Cassini/VIMS, *Icarus*, *270*, 85 – 99, doi:http://dx.doi.org/10.1016/j.icarus.2015.05.003.

Solomonidou, A., et al. (2018), The spectral nature of Titan's major geomorphological units: Constraints on surface composition, *Journal of Geophysical Research: Planets*, doi:http://dx.doi.org/10.1002/2017JE005477.

Sotin, C., et al. (2005), Release of volatiles from a possible cryovolcano from near-infrared imaging of Titan, *Nature*, *435*, 786 – 789, doi:http://dx.doi.org/10.1038/nature03596.

Stephan, K., et al. (2010), Specular reflection on Titan: Liquids in Kraken Mare, *Geophysical Research Letters*, *37*(7), doi:10.1029/2009GL042312.

Stiles, B. W. (2008), Cassini Radar Basic Image Data Records SIS, Version 2.0., http://pds-imaging.jpl.nasa.gov/documentation/Cassini_BIDRSIS.PDF.

Stiles, B. W., et al. (2009), Determining Titan surface topography from Cassini SAR data, *Icarus*, *202*(2), 584 – 598.

Stofan, E. R., et al. (2006), Mapping of Titan: Results from the first Titan radar passes, *Icarus*, *185*(2), 443 – 456, doi:http://dx.doi.org/10.1016/j.icarus.2006.07.015.

Stofan, E. R., et al. (2007), The lakes of Titan, *Nature*, *445*(7123), 61 – 64.

Tobie, G., O. Grasset, J. I. Lunine, A. Mocquet, and C. Sotin (2005), Titan's internal structure inferred from a coupled thermal-orbital model, *Icarus*, *175*(2), 496 – 502, doi:http://doi.org/10.1016/j.icarus.2004.12.007.

Tobie, G., J. I. Lunine, and C. Sotin (2006), Episodic outgassing as the origin of atmospheric methane on Titan, *Nature*, *440*(7080), 61 – 64, doi:http://dx.doi.org/10.1038/nature04497.

Tomasko, M. G., L. Doose, S. Engel, L. E. Dafoe, R. West, M. Lemmon, E. Karkoschka, and C. See (2008), A model of Titan's aerosols based on measurements made inside the atmosphere, *Planetary and Space Science*, *56*(5), 669 – 707, doi:http://dx.doi.org/10.1016/j.pss.2007.11.019.

Tomasko, M. G., et al. (2005), Rain, winds and haze during Huygens probe descent to Titan surface, *Nature*, *438*, 765 – 778, doi:10.1038/nature04126.

Turtle, E. P., J. E. Perry, A. S. McEwen, A. D. Del Genio, J. Barbara, R. A. West, D. D. Dawson, and C. C. Porco (2009), Cassini imaging of Titan's high-latitude lakes, clouds, and south-polar surface changes, *Geophysical Research Letters*, *36*(2).

Turtle, E. P., J. E. Perry, A. G. Hayes, and A. S. McEwen (2011), Shoreline retreat at Titan's Ontario Lacus and Arrakis Planitia from Cassini Imaging Science Subsystem observations, *Icarus*, *212*(2), 957–959.

Tyler, G. L., V. R. Eshleman, J. D. Anderson, G. S. Levy, G. F. Lindal, G. E. Wood, and T. A. Croft (1981), Radio science investigations of the Saturn system with Voyager 1: Preliminary results, *Science*, *212*(4491), 201–206, doi:10.1126/science.212.4491.201.

Villa, A., J. Chanussot, J. A. Benediktsson, and C. Jutten (2011), Spectral unmixing for the classification of hyperspectral images at a finer spectral resolution, *IEEE Journal of Selected Topics in Signal Processing*, *5*(3).

Vinatier, S., et al. (2010), Analysis of Cassini/CIRS limb spectra of Titan acquired during the nominal mission I. Hydrocarbons, nitriles and CO2 vertical mixing ratio profiles, *Icarus*, *205*, 559 – 570, doi:10.1016/j.icarus.2009.08.013.

Willacy, K., M. Allen, and Y. Young (2016), A new astrobiological model of the atmosphere of Titan, *Astrophysical Journal*, *829*, 79, doi:http://dx.doi.org/10.3847/0004-637X/829/2/79.

Williams, D. A., J. Radebaugh, R. M. C. Lopes, and E. Stofan (2011), Geomorphologic mapping of the Menrva region of Titan using Cassini RADAR data, *Icarus*, *212*, 744 – 750, doi:http://dx.doi.org/10.1016/j.icarus.2011.01.014.

Wood, C. A., R. Lorenz, R. L. Kirk, R. Lopes, K. Mitchell, and E. R. Stofan (2010), Impact craters on Titan, *Icarus*, *206(1)*, 334–344.

Wood, C. A., E. R. Stofan, A. G. Hayes, R. K. Kirk, J. I. Lunine, J. Radebaugh, and M. Malaska (2013), Morphological evidence of former seas near Titan's south pole, in *the 44th LPSC Abstracts*.

Wye, L. C., H. A. Zebker, and R. D. Lorenz (2009), Smoothness of Titan's Ontario Lacus: Constraints from Cassini RADAR specular reflection data, *Geophysical Research Letters*, *36*(16), doi:10.1029/2009GL039588.

Zebker, H. A., Y. Gim, P. Callahan, S. Hensley, and R. Lorenz (2009a), Analysis and interpretation of Cassini Titan radar altimeter echoes, *Icarus*, *200*(1), 240 – 255, doi: http://dx.doi.org/10.1016/j.icarus.2008.10.023.

APPENDICES

A/ SAR SWATHS - PROCESSING

PROCESSING OF RADAR BIDR PRODUCTS USING ISIS3

Cassini's RADAR microwaves were able to penetrate the dense and opaque atmosphere of Titan and hence probe its surface. RADAR data enable evaluating the surface physical properties and composition through its various operational modes. One of the specific objectives of RADAR was to determine the existence and distribution of the lakes on Titan. RADAR was also used to investigate the geologic features and topography of the solid surface of the moon, thanks to its high spatial resolution relatively to the optical imaging instruments (VIMS and ISS). For the present work I essentially used the Basic Image Data Records (BIDR), which are the single pass, calibrated and gridded Synthetic Aperture Radar (SAR) data. SAR/BIDR data are publicly released in Planetary Data System (PDS) format and produced in an oblique cylindrical map projection.

LABEL FOR CASSINI SAR/BASIC IMAGE DATA RECORD

Each SAR/BIDR swath is labeled as follows: "aabcdeefggg_Dhhh_TiiiSjj_Vnn", where each term indicates the different characteristics of the data, as show in Table A.1. Thus, a given SAR swath labeled as BIBQI49N071_D035_T00AS01.IMG should represent BIDR dataset, with values in dB normalized between 0 and 255, with an oblique cylindrical projection and a map resolution at 256 pixel/degree (0.17 km/pixel). Moreover this SAR swath is centered at 49°N and 71°W, and it will be acquired during the flyby Ta by the first trace segment (S01), stored in the CORADR archive 35.

DATA INGESTION

The BIDR data (PDS product) are compressed and have a .ZIP file extension. A BIDR data contains map projection keyword labels which are required by the Integrated Software for Imagers and Spectrometers version 3 (ISIS3). After decompressing the .ZIP file, the pds2isis application is then used to ingest the PDS product into ISIS3, as follows.

(1) - Download the image and label files:
Search in the PDS Image Node website[1] the "CORADR_0045" archive folder for the files listed below: Find both files "BIBQH22N068_D045_T003S01_V02.ZIP" and "-.LBL" in the archive folder and copy them to the local work area.

(2) - Decompress the PDS .ZIP file:
Unzip BIBQH22N068_D045_T003S01_V02.ZIP

(3) - Ingest the PDS .IMG file into ISIS3 using pds2isis application:

```
pds2isis from=BIBQH22N068_D045_T003S01_V02.IMG
to=BIBQH22N068_D045_T003S01_V02.cub
```

The pipeline of those SAR/BIDR data processing is described in the ISIS Workshop website[2].

REPROJECTION

SAR/BIDR data are initially in oblique cylindrical projection and each one has its own unique mapping parameters. Then, it is difficult to visualize where the north is on the images. That is why converting the file to a different map projection enables identifying the image coordinates. If the images have to be imported into a GIS, they need to be reprojected to a common set of map parameters (map scale, center latitude, center longitude ...). There are two options: (1) use the current mapping information and only modify the map projection, or (2) redefine the appropriate mapping parameters to import all the reprojected images in a GIS. The two following examples show both possibilities.

Example (1) - Convert to a different projection with map2map file for visual inspection:

```
map2map from=BIBQH51S121_D177_T049S01_V02.cub
to=BIBQH51S121_D177_T049S01_V02_simp.cub
map=\$ISIS3DATA/base/templates/maps/simplecylindrical.map.
```

Example (2) - Define map parameters to import data in a GIS:

Run maptemplate to redefine some mapping parameters in order to import the reprojected images in a GIS. The center latitude, center longitude, and map resolution must match. The user will also need to select the longitude domain (180 or 360).

[1]Link to PDS Image Node: http://pds-imaging.jpl.nasa.gov/
[2]Link to ISIS workshop: https://isis.astrogeology.usgs.gov/IsisWorkshop/index.php

Note that ISIS3 defaults to a Positive Longitude East direction, and thus the map template file can be used to specify a Positive Longitude West:

```
maptemplate map=my_simp.map  projection=simplecylindrical  clon=0
targopt=user  targetname=Titan  londir=positivewest  londom=180
```

The program produces a PVL file containing the following parameters:

```
Group = Mapping
  ProjectionName = SimpleCylindrical
  CenterLongitude = 0.0
  TargetName = Titan
  EquatorialRadius = 2575000.0 <meters>
  PolarRadius = 2575000.0 <meters>
  LatitudeType = Planetocentric
  LongitudeDirection = PositiveWest
  LongitudeDomain = 180
End_Group
End
```

In this example, the file is reprojected to a simple cylindrical projection using map2map application:

```
map2map from=BIBQH51S121_D177_T049S01_V02.cub
to=BIBQH51S121_D177_T049S01_V02_simp.cub
map=my_simp.map
```

Occasionally map2map will fail if it cannot resolve the default latitude and longitude extents of the input file. The error message reported is:

```
Error message:
  Group = Error
    Program = map2map
    Code = 1
    Message = "Unable to determine the correct
[MinimumLongitude,MaximumLongitude].
Please specify these values in the [MINLON,MAXLON] parameters"
    File = map2map.cpp
    Line = 304
  End_Group
```

This error is mostly due to the longitude range falling outside of the longitude domain previously selected. For example, the 180 longitude domain was chosen but the longitude range for this file goes beyond 180. Since the map template does not contain the image boundary, the values in the labels are used. In this case, the latitude and longitude extents need to be entered by the used in order to remap the pixels to the correct locations in a 180 longitude domain. The values entered must be appropriate for the longitude domain selected.

```
Group = Mapping
  ProjectionName = ObliqueCylindrical
  TargetName = Titan
  EquatorialRadius = 2575000.0 <meters>
  PolarRadius = 2575000.0 <meters>
  LatitudeType = Planetocentric
  LongitudeDirection = PositiveWest
  LongitudeDomain = 360
  MinimumLatitude = -89.99653831
  MaximumLatitude = -10.56685759
  MinimumLongitude = 0.0
  MaximumLongitude = 360.0
  UpperLeftCornerX = -2067342.51008 <meters>
  UpperLeftCornerY = 4449280.61952 <meters>
  PixelResolution = 351.11116 <meters/pixel>
  Scale = 128.0 <pixels/degree>
  Rotation = 90.0
  PoleLatitude = -15.827261 <DEG>
  PoleLongitude = 342.714697
  PoleRotation = 43.599373 <DEG>
  XAxisVector = (-0.39349534, 0.59978022, -0.69672456)
  YAxisVector = (-0.03558647, 0.74735851, 0.66346730)
  ZAxisVector = (0.91863759, 0.28586526, -0.27273803)
End_Group
```

Look at the latitude and longitude extents of the file, bolded values above, to help determine what values to enter. If the longitude range goes from 0 to 360 and the longitude domain selected is 180, then use minlon=-180 and maxlong=180. The only requirement is that there must be sufficient work space available to generate a large file.

```
map2map from=BIBQH51S121_D177_T049S01_V02.cub
to=BIBQH51S121_D177_T049S01_V02_simp.cub
map=my_simp.map minlat=-90.0 maxlat=-10.5 minlon=-180 maxlon=180
```

Display the file to view the result using qview:

```
qview BIBQH22N068_D045_T003S01_V02_simp.cub
```

CONVERSION TO GIS FORMAT

After map-projection the SAR swaths need to be converted into a JP2 or TIF format (Jpeg2000 or GeoTiff, respectively) in order to import them into a GIS (here, ArcGIS), which is done by using isis2std application.

```
isis2std from=BIBQD03S325_D100_T019S03_V02_simp.cub
to=BIBQD03S325_D100_T019S03_V02_simp.jp2
format=JP2

or

isis2std from=BIBQD03S325_D100_T019S03_V02_simp.cub
to=BIBQD03S325_D100_T019S03_V02_simp.tif
format=TIFF

Group = Results
  OutputFileName = BIBQD03S325_D100_T019S03_V02_simp.tif
  InputMinimum = -13.30000184
  InputMaximum = 0.10001424
End_Group
```

INTEGRATION INTO A GIS

After map-projection and conversion into JP2 (or TIF) format, SAR swaths are imported in the GIS. Nevertheless few steps are necessary to allow the correct integration of the SAR swaths in the software, as shown in Figure A.1.

In ArcCatalog:

In the folder where all the SAR images are stored
Properties (right click)
→ Spatial References: Edit
→ Add a new coordinate system:
- Name it: Titan (for example)
- Choose Plate_Carree as projection

- Define a central meridian (0 or 180)
- Select the datum D_Titan_2000 as geographic coordinate system

In ArcMap:

Import the new edited SAR swaths from ArcCatalog. The display parameters can be re-defined in the layer properties (right click > Properties > Symbology), in order to remove the black background behind each integrated SAR swath (Display Background Value: 0 as No Color).

SAR data used in the present investigation are listed in the following tables (Tables A.2, A.3, A.4, A.5 and A.6) with their most relevant characteristics (flyby, segment, date, altitude, latitude and longitude ranges, incidence angle range and resolution). Note that last flybys operating in SAR imaging mode were performed in July 2016 (T121) and April 2017 (T126), but the corresponding data are not included in this work since they are not yet calibrated and publicly released.

Table A.1 – Description of the label for SAR/Basic Image Data Records (*Stiles*, 2008).

Typical SAR/BIDR swath labelled "aabcdeefggg_Dhhh_TiiiSjj_Vnn"		
aa	Dataset	
	BI	Basic Imaging Data Records (BIDR)
b	Dataset	
	F	Primary dataset with σ0 corrected from the incidence angle and noise, in 32-bit floating point format (linear scale values, not in dB)
	B	Primary dataset in unsigned byte format (values converted to dB and normalized to fit in [0,255] range)
	U	σ0 values corrected from the noise but not from incidence angle, in 32-bit floating point format (linear scale values, not in dB)
	E	Incidence angle map, floating point values in degrees
	T	Latitude map, floating point values in degrees
	N	Longitude map, floating point values in degrees
	M	Beam mask map, 8 bit values
	L	Number of looks map, 32 bit integer values
c	Map projection	
	Q	Oblique cylindrical (used to conform with higher level product naming convention)
d	Map resolution	
	B	2 pixels/degree (22 km/pixel at the equator)
	D	8 pixels/degree (5.5 km/pixel at the equator)
	F	32 pixels/degree (1.38 km/pixel at the equator)
	G	64 pixels/degree (0.7 km/pixel at the equator)
	H	128 pixels/degree (0.34 km/pixel at the equator)
	I	256 pixels/degree (0.17 km/pixel at the equator)
ee	Absolute value of latitude at center of file, rounded to nearest degree	
f	Hemisphere of the center	
	N	North
	S	South
ggg	West longitude at the center, rounded to nearest degree	
hhh	3-digit mission unique Cassini RADAR data take number from which data are included	
iii	3-digit integer indicating the number of the flyby during which data are acquired	
jj	2-digit integer indicating the number of the segment which acquired the data	
nn	2-digit integer indicating the version number of a product file	

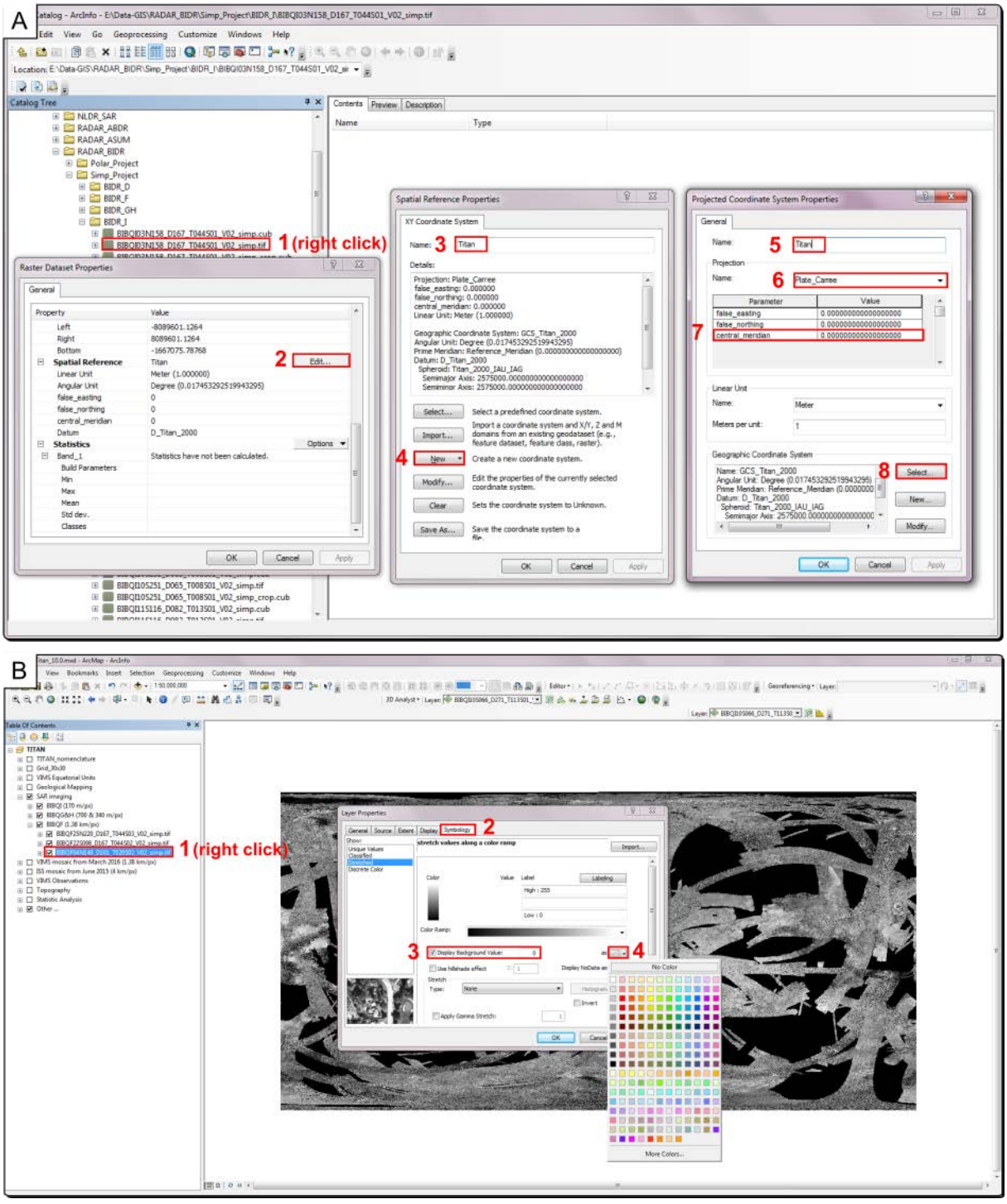

Figure A.1 – Screenshots explaining how to process in (A) ArcCatalog and (B) ArcMap in order to integrate the SAR swaths on ArcGIS (Esri) software package

Table A.2 – Characteristics of SAR swaths used in this work.

Flyby	Segm.	Date	Altitude (km)	Lat. range (°N/S)	Lon. range (°W)	Incidence (°)	Sampling (m/pixel)
T00a	S01	Oct. 27, 2004	1174	30 - 54N	6 - 134	5.5 - 44.3	170
T003	S01	Feb. 15, 2005	1579	38 - 23N	0 - 134	3.7 - 29.6	170
T007	S01	Sept. 7, 2005	1075	28 - 74S	0 - 28/342 - 360	8.2 - 34.7	170
T008	S01 S02 S03	Oct. 28, 2005	1353	4 - 18S 178 - 5N 178 - 6N	183 - 319 309 - 319 181 - 188	8.9 - 28.5 4.3 - 29.3 15.5 - 24.7	170 340 340
T013	S01 S02 S03	Apr. 30, 2006	1856	3 - 17S 17S - 8N 0 - 12S	62 - 171 165 - 171 182 - 200	10.7 - 28.7 2.4 - 26.4 3.7 - 24.8	170 340 340
T015	S02 S03	Jul. 2, 2006	1906	23 - 39S 17 - 29S	13 - 50 36 - 50	32.5-41.6 25-40.9	340 340
T016	S01 S02 S03	Jul. 21, 2006	950	13 - 83N 18 - 30N 13 - 22N	0 - 150/340 - 360 137 - 154 336 - 348	9.7 - 39.6 2.1 - 29.3 2 - 22	170 340 340
T017	S01	Sept. 7, 2006	1000	3 - 16N	32 - 68	29.7 - 44	170
T018	S01	Sept. 23, 2006	960	34 - 75N	0 - 106/346 - 360	19.5 - 44.3	170
T019	S01 S02 S03 S04 S05 S06	Oct. 9, 2006	980	68 - 87N 33 - 48N 0 - 5S 15S - 13N 15S - 13N 15S - 2N	0 - 160/313 - 360 136 - 153 318 - 330 307 - 325 290 - 310 289 - 296	9.8 - 38.2 1.9 - 23.3 2.7 - 22.2 5.2 - 39.3 31.4 - 39.4 34 - 45.9	170 340 340 340 340 340
T020	S02 S03 S04	Oct. 25, 2006	1030	14S - 14N 10S - 14N 5 - 35N	98 - 177 98 - 146 130 - 146	19.8 - 61 24.1 - 42.7 4.2 - 29	1380 340 340
T021	S01 S02	Dec. 12, 2006	1000	30S - 53N 14 - 28S	192 - 305 297 - 302	9.6 - 54.2 2 - 23	170 340
T023	S01 S02 S03	Jan. 13, 2007	1000	40S - 60N 49 - 62N 27 - 40S	0 - 102/327 - 360 90 - 98 327 - 343	9.6 - 37.5 2 - 22.3 2.2 - 28	170 340 340
T025	S01 S02 S04 S05 S06	Feb. 22, 2007	1000	36S - 86N 29 - 34S 63 - 89N 63 - 90N 63 - 90N	0 - 59/211 - 360 39 - 54 70 - 160 70 - 214 162 - 258	9.1 - 37 2.1 - 21.7 35.4 - 44.9 31.9 - 41.6 28.5 - 38.3	170 340 340 340 340
T028	S01 S02 S03	Apr. 10, 2007	990	21S - 82N 10 - 21S 51 - 56N	0 - 44/203 - 360 25 - 43 215 - 230	6.5 - 34.9 2.6 - 26.4 2.5 - 17.7	170 340 340
T029	S01 S02 S03	Apr. 26, 2007	980	4S - 87N 0 - 4S 44 - 50N	0 - 40/196 - 360 26 - 35 199 - 222	9.3 - 38.2 1.7 - 16.6 2 - 25.3	170 340 340

Note: Resolution should be about twice the spatial sampling to allow resolving and identifying surface features.

Table A.3 – Characteristics of SAR swaths used in this work (*continued*).

Flyby	Segm.	Date	Altitude (km)	Lat. range (°N/S)	Lon. range (°W)	Incidence (°)	Sampling (m/pixel)
T029	S04	Apr. 26, 2007	980	48 - 79N	155 - 185	32.9 - 57.9	340
	S05			48 - 79N	155 - 194	27.9 - 57.9	340
	S06			48 - 81N	183 - 218	28 - 55.1	340
T030	S01	May 12, 2007	960	29 - 74N	219 - 333	9.4 - 46.6	170
	S02			69 - 75N	329 - 357	2.9 - 32	340
	S03			30 - 42N	217 - 233	2.4 - 28	340
T036	S01	Oct. 2, 2007	975	12 - 50S	12 - 45	3.5 - 36.7	340
	S02			12 - 50S	8 - 46	11 - 53	170
	S03			37 - 72S	25 - 196	30.8 - 59.2	170
	S04			21S - 26N	182 - 210	4.9 - 68.4	340
T039	S01	Dec. 20, 2007	970	27 - 90S	0 - 360	9.7 - 51	170
	S02			30 - 40S	21 - 36	1.9 - 22.8	340
	S03			11S - 26N	187 - 206	4.3 - 50.9	340
	S04			38 - 65S	0 - 19/348 - 360	38.7 - 48	340
	S05			40 - 87S	0 - 11/256 - 360	42.4 - 79.5	340
	S06			37 - 87S	0 - 2/259 - 360	43.7 - 78.8	340
	S07			30 - 41S	0 - 32/345 - 360	2.5 - 49	340
T041	S01	Feb. 22, 2008	1000	16 - 37S	60 - 162	12.3 - 41.9	170
	S02			30S - 13N	169 - 219	3.5 - 25	170
	S03			20 - 37S	63 - 68	1.8 - 25	340
	S04			9 - 11N	208 - 216	4.3 - 18.2	340
	S05			6 - 13N	43 - 47	41.4 - 48.1	340
	S06			6S - 14N	43 - 92	36.6 - 53.9	340
	S07			2 - 32S	59 - 92	4.8 - 54.3	340
T043	S01	May 12, 2008	1000	36S - 32N	74 - 220	7.7 - 41.4	170
	S02			12 - 37S	71 - 85	3.5 - 26.8	340
	S03			16 - 41N	206 - 221	2 - 27.4	340
	S04			23 - 37S	67 - 136	8.7 - 69	340
	S05			22 - 34S	106 - 135	41.3 - 69.3	340
	S06			20 - 33S	106 - 134	41.3 - 68.7	340
	S07			18 - 31S	74 - 134	3.7 - 68.5	340
T044	S01	May 28, 2008	1360	32S - 26N	95 - 225	9.5 - 26.8	170
	S02			17 - 29S	97 - 99	1.7 - 18.5	1380
	S03			18 - 29N	216 - 225	1.7 - 22.4	1380
T048	S01	Dec. 5, 2008	971	20 - 33S	96 - 138	11.2 - 29.5	170
	S02			15 - 27S	118 - 138	16.3 - 67	170
	S03			18S - 47N	118 - 230	31 - 74.1	170
	S04			47 - 59S	115 - 179	26.6 - 67.3	700
	S05			25 - 37S	98 - 112	1.8 - 23.8	340
T049	S01	Dec. 21, 2008	971	13 - 86S	67 - 165	8.5 - 56.7	340
	S02			64S - 29N	242 - 280	9 - 39	170
	S03			8S - 17N	270 - 285	20 - 50.9	340
	S04			19 - 26N	260 - 274	1.9 - 22.4	340
T050	S01	feb 7, 2009	967	58S - 17N	0 - 17/298 - 360	31.1 - 57.9	170

Note: Resolution should be about twice the spatial sampling to allow resolving and identifying surface features.

Table A.4 – Characteristics of SAR swaths used in this work (*continued*).

Flyby	Segm.	Date	Altitude (km)	Lat. range (°N/S)	Lon. range (°W)	Incidence (°)	Sampling (m/pixel)
T050	S02 S03 S04 S05 S06	Feb. 7, 2009	967	23 - 70S 11S - 13N 31 - 54S 24 - 64N 52 - 68S	0 - 155/340 - 360 245 - 280 44 - 48 257 - 290 48 - 64	14.4 - 74.2 37.3 - 63.7 23 - 53.1 4.5 - 65 3.8 - 22.2	700 700 340 340 340
T055	S01 S02 S03 S04 S05	May 21, 2009	966	77S - 38N 15 - 42N 58 - 83S 32 - 35N 62 - 71S	120 - 285 92 - 143 140 - 290 125 - 141 254 - 278	9.4 - 38.3 3.8 - 40 5.2 - 58.9 1.9 - 22.8 2.2 - 21.8	340 700 700 340 340
T056	S01 S02 S03 S04	Jun. 6, 2009	968	77S - 30N 8 - 32N 25 - 28N 62 - 67S	125 - 313 102 - 142 130 - 145 274 - 301	9.6 - 38.3 7.5 - 40.5 1.9 - 22.4 1.9 - 20.5	170 700 340 340
T057	S01 S02	Jun. 22, 2009	955	82S - 18N 36 - 53S	130 - 318 219 - 301	31.3 - 71 3.4 - 71.4	170 700
T058	S01 S02 S03	Jul. 8, 2009	966	82S - 6N 36S - 4N 50 - 59S	135 - 337 140 - 150 247 - 320	9.7 - 38.5 13.1 - 61.3 22.3 - 61	170 340 340
T059	S01	Jul. 24, 2009	956	8 - 22S	140 - 335	31.4 - 53.7	170
T061	S01 S02 S03 S04 S05 S06	Aug. 25, 2009	961	16S - 19N 0 - 15S 0 - 14S 14S - 2N 10 - 14N 3 - 5N	166 - 310 152 - 162 154 - 162 154 - 166 169 - 170 300 - 308	9.2 - 38.2 8.8 - 25.5 9.2 - 23.7 2.4 - 21.6 17.6 - 22.8 22.7 - 33	170 340 340 340 340 340
T064	S01 S02	Dec. 27, 2009	955	10 - 87N 10 - 53N	0 - 14/209 - 360 155 - 203	10.1 - 53.3 6.9 - 65.7	170 700
T065	S01 S02 S03 S04 S05	Jan. 12, 2010	1073	40 - 85S 64 - 74S 71 - 73S 71 - 73S 2 - 71S	0 - 8/168 - 360 174 - 198 180 - 189 180 - 189 185 - 244	2.8 - 45.4 18.8 - 44.3 41.9 - 46.1 45.9 - 47.5 17.5 - 70.4	170 170 340 340 340
T069	S01	Jun. 5, 2010	2044	10S - 60N	0 - 62/325 - 360	13 - 65.2	700
T071	S01	Jul. 7, 2010	1005	30 - 70S	0 - 20/210 - 360	29.7 - 59.4	170
T077	S01 S02 S03 S04	Jun. 20, 2011	1358.7	1 - 21N 5 - 31S 6 - 34N 1 - 16N	33 - 96 111 - 152 50 - 92 35 - 41	8 - 31.4 49.4 - 78.6 38.7 - 71 1.9 - 26	170 700 700 170
T083	S01 S02 S04	May 21, 2012	955	14 - 86N 4 - 30N 17 - 21N	20 - 216 32 - 52 198 - 206	10.3 - 53.7 8.6 - 61 1.9 - 15.2	170 700 340

Note: Resolution should be about twice the spatial sampling to allow resolving and identifying surface features.

Table A.5 – Characteristics of SAR swaths used in this work (*continued*).

Flyby	Segm.	Date	Altitude (km)	Lat. range (°N/S)	Lon. range (°W)	Incidence (°)	Sampling (m/pixel)
T083	S05	May 21, 2012	955	6 - 28N	152 - 200	6.5 - 59.7	700
T084	S01	Jun. 6, 2012	959	3 - 54N	0 - 20/206 - 360	9.7 - 38.9	170
	S02			31 - 75N	0 - 4/285 - 360	29 - 81.7	700
	S03			26 - 31N	0 - 14	2 - 20.7	340
	S04			5 - 9N	211 - 221	2 - 18.9	340
	S05			2 - 22S	212 - 258	4.9 - 55.7	700
T086	S01	Sep. 26, 2012	956	20 - 81N	212 - 346	31.2 - 52.8	170
	S02			74 - 80N	238 - 273	55.4 - 64	340
	S03			48 - 78N	268 - 357	29.5 - 69	340
	S04			17S - 20N	212 - 220	51.1 - 79.6	340
T091	S01	May 23, 2013	969.8	5 - 47N	240 - 256	6.8 - 38.3	170
	S02			53 - 81N	0 - 51/270 - 360	10 - 73.3	700
	S03			59 - 69N	61 - 87	2 - 25.3	340
	S04			56 - 84N	74 - 157	13.1 - 30.5	170
	S05			80 - 88N	157 - 230	2.4 - 22.2	340
	S06			45 - 51N	240 - 248	2.4 - 18.1	340
	S07			4 - 7N	240 - 244	2 - 7.7	340
	S08			8 - 23S	202 - 237	10 - 46	700
T092	S01	Jul. 10, 2013	964	35S - 88N	74 - 277	2.5 - 38	170
	S02			40 - 90N	0 - 50/245 - 360	11.5 - 81.6	700
	S03			66 - 78N	70 - 90	1.7 - 21.6	340
	S05			10 - 36S	170 - 288	6.9 - 66.4	700
T095	S01	Oct. 14, 2013	961	64S - 70N	148 - 220	21.5 - 69	170
	S02			38 - 85N	212 - 268	19.5 - 61.2	700
	S03			30 - 85S	148 - 222	11.7 - 44.3	700
T098	S01	Feb. 2, 2014	1235.7	28 - 90S	0 - 360	12.4 - 31.5	170
	S02			1S - 64N	176 - 245	29 - 73.8	700
	S03			74 - 86S	260 - 307	2.8 - 23.2	340
	S04			50 - 90S	0 - 360	20.5 - 52.9	700
	S05			24 - 30S	171 - 177	2.3 - 19.5	340
	S06			12 - 45N	158 - 196	5.9 - 61.4	340
T104	S01	Aug. 21, 2014	964	11S - 56N	332 - 360	20.3 - 53.1	170
	S02			20S - 14N	0 - 3/332 - 360	40.9 - 74.7	700
	S04			54 - 64N	335 - 338	2.3 - 21.8	340
	S05			68 - 83N	205 - 285	2.7 - 18.9	170
T108	S01	Jan. 11, 2015	970	6S - 78N	0 - 30/354 - 360	2.8 - 13.4	170
	S02			25S - 25N	0 - 12/324 - 360	9.9 - 59.9	700
	S03			6S - 7N	12 - 22	3.3 - 17.4	340
	S04			51 - 89N	200 - 270	2.2 - 13.4	170
	S05			22 - 90N	0 - 360	56.6 - 76.9	700
T113	S01	Sep. 28, 2015	1035.6	0 - 20S	0 - 138/353 - 360	4.8 - 64.2	170
	S02			1 - 7S	125 - 135	2.2 - 18.5	340
	S03			28 - 42S	316 - 331	53 - 74.8	340

Note: Resolution should be about twice the spatial sampling to allow resolving and identifying surface features.

Table A.6 – Characteristics of SAR swaths used in this work (*continued*).

Flyby	Segm.	Date	Altitude (km)	Lat. range (°N/S)	Lon. range (°W)	Incidence (°)	Sampling (m/pixel)
T113	S04	Sep. 28, 2015	1035.6	10 - 30S	330 - 343	25.7 - 52.7	170
	S05			1 - 12S	341 - 353	2.1 - 26.3	340
	S06			1 - 6S	5 - 30	24 - 51.6	340
	S07			8 - 38N	5 - 56	38.3 - 80.6	700
T120	S01	Jun. 8, 2016	975	81S - 25N	0 -360	9.9 - 65.4	170
	S02			65S - 46N	25 - 58	2 - 22	340
	S03			11 - 46N	183 - 220	13.2 - 52.3	340
	S04			29S - 44N	136 - 208	19.3 - 46	340
	S05			35S - 90N	85 - 264	11.7 - 63.4	700

Note: Resolution should be about twice the spatial sampling to allow resolving and identifying surface features.

B/ SURFACE ALBEDO EXTRACTION

INVERSION OF VIMS DATA WITH RADIATIVE TRANSFER CODE

Figures B.1 to B.4 are Lambert albedo (A_L) maps of the surface in the eight atmospheric windows (0.93, 1.07, 1.27, 1.57, 2.01, 2.68, 2.76 and 5 µm) for the VIMS cubes listed in Table 4.1 (see Chapter 4). Two additional maps are provided: a haze factor map (gray scale) and a RMS map (rainbow scale) accounting for the classical quadratic difference between data and model. Note that two of the VIMS cubes listed in Table 4.1 (i.e. CM_1525118253 and CM_1826075655) are not used for the radiative transfer inversion, as they are only necessary to display the regional context of Sinlap (Figure 4.2A) and Menrva (Figure 4.4A) craters.

EXTRACTION OF SINGLE-SCATTERING ALBEDO (ω_0)

After applying the radiative transfer model on the selected VIMS data and converting the Lambert albedo (A_L) to a single-scattering albedo (ω_0), masks were used in the regions of interest (also noted RoIs) to extract surface information. Figure B.5 illustrates this procedure with each considered RoIs, where masks indicate the locations where surface albedo were extracted for the IR-bright (green masks), IR-brown (brown masks), and IR-blue (blue masks) units. Here, the observations are non-projected (north is up) and displayed as false-color composites of simple channels (red: average over 4.90-5.12 µm, green: 2.01 µm, and blue: 1.27 µm).

SPECTRA OF SINGLE-SCATTERING ALBEDO (ω_0)

Figure B.6 displays the spectra of the single-scattering albedo (ω_0) in the eight infrared atmospheric windows for the infrared units found in each of the investigated region: IR-bright (green), IR-blue (blue) and IR-brown (brown). The single-scattering albedo values are derived from the radiative transfer model applied in the VIMS observations listed in Table 4.1. (A) Sinlap crater, using VIMS observation cubes from T105, T109 and T110. (B) Aaru Regio with T61 and T109. (C) Menrva crater with T114. (D) Eastern Xanadu with T9 and T114. (E) Chusuk Planitia with T20. Error bars are the standard deviation.

Note that the IR-blue unit in Chusuk Planitia (Spectra in Figure B.6E) is slightly brighter than the IR-bright unit in the 0.93 µm-window. This observations seems quite unexpected since the IR-bright units are brighter than the IR-blue and -brown units in all the atmospheric windows of the infrared range. Hence, the IR-blue unit found in Chusuk Planitia is expected to be darker in the 0.93 µm-window, as seen in the ISS observations (0.938 µm). This effect is assumed to be due to an instrumental issue (additional scattering) which is met when the spectrometer probes the surface at low altitude. Indeed, during the T20 flyby, Cassini was very close to the surface, with an altitude of about 1321 km (this approach was usually used for RADAR operations). As seen in Figure B.6E, this effect is only important at shorter wavelengths, particularly at 0.93 µm where the surface is not even distinguishable (Figure B.4B). Thus, this issue does not affect our inversions since we are not using this window in our investigation.

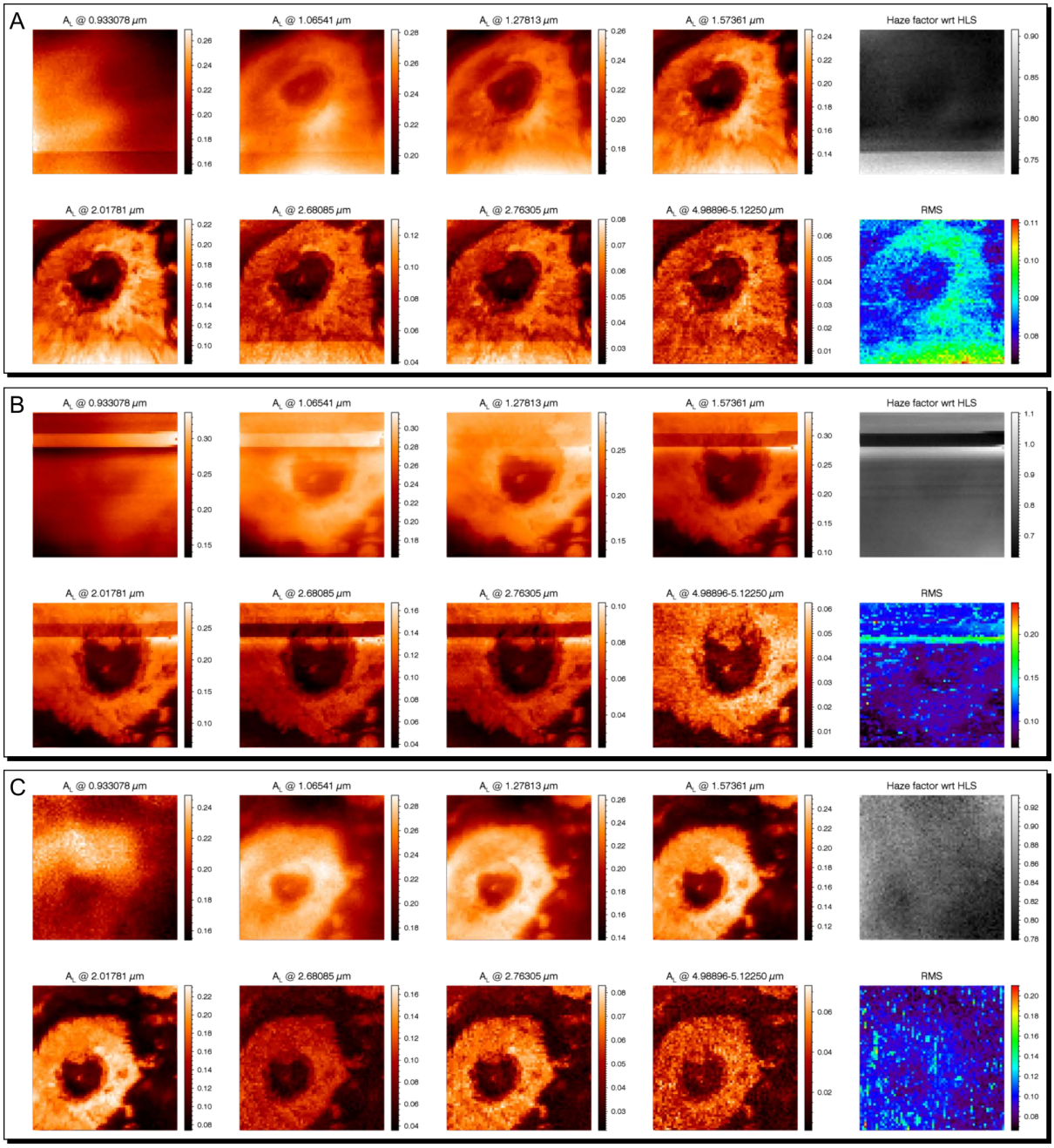

Figure B.1 – Lambert albedo maps produced after applying the radiative transfer model for VIMS data targeting Sinlap crater and its surroundings through (A) CM_1790056808 (T105, September 2014), (B) CM_1802454074 (T109, February 2015), and (C) CM_1805209469 (T110, March 2015).

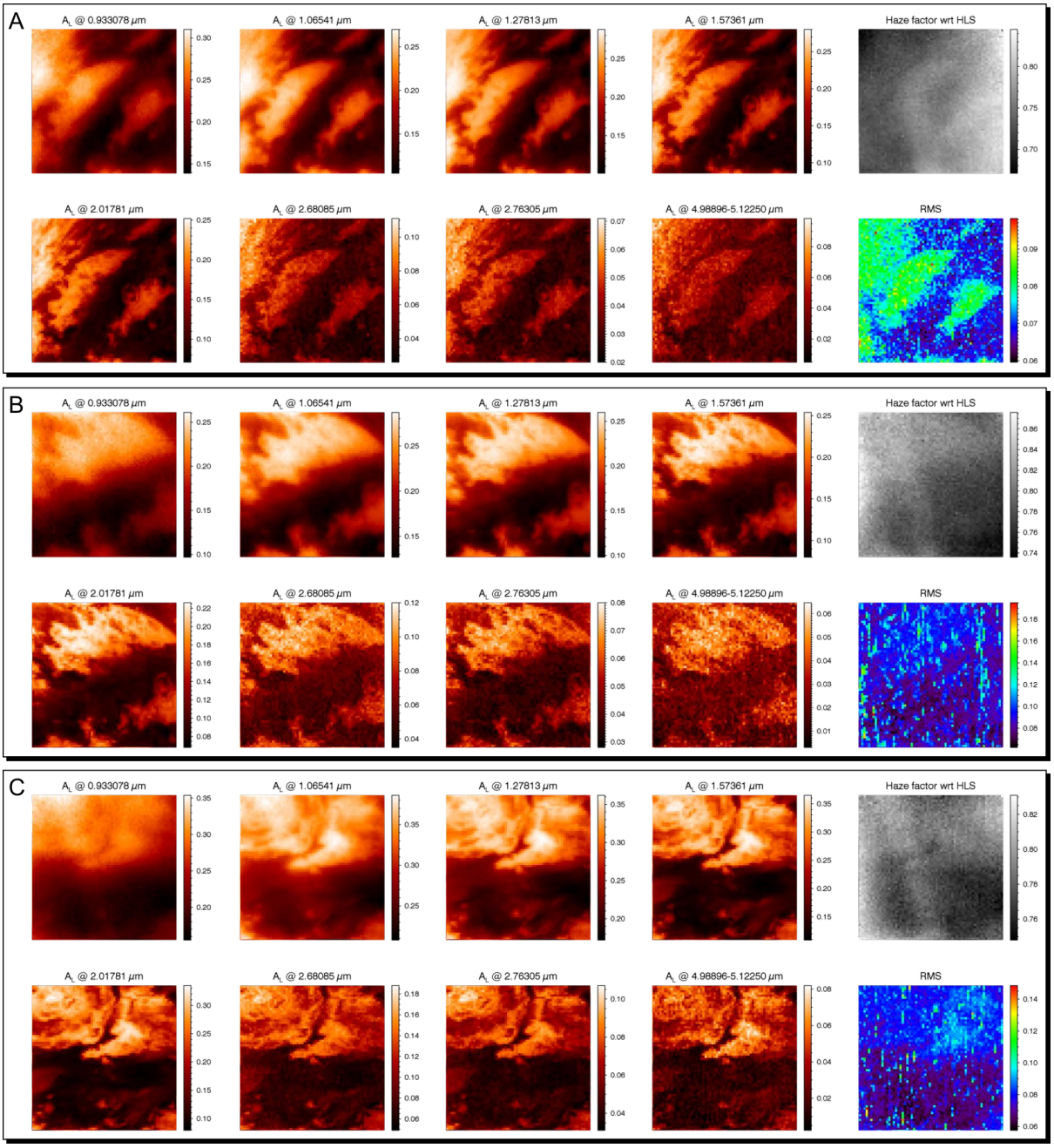

Figure B.2 – Lambert albedo maps produced after applying the radiative transfer model for VIMS data targeting Aaru Regio through (A) CM_1629905033 (T61, August 2009) and (B) CM_1802450543 (T109, February 2015), and Menrva crater and its surroundings through (C) CM_1826086162 (T114, November 2015).

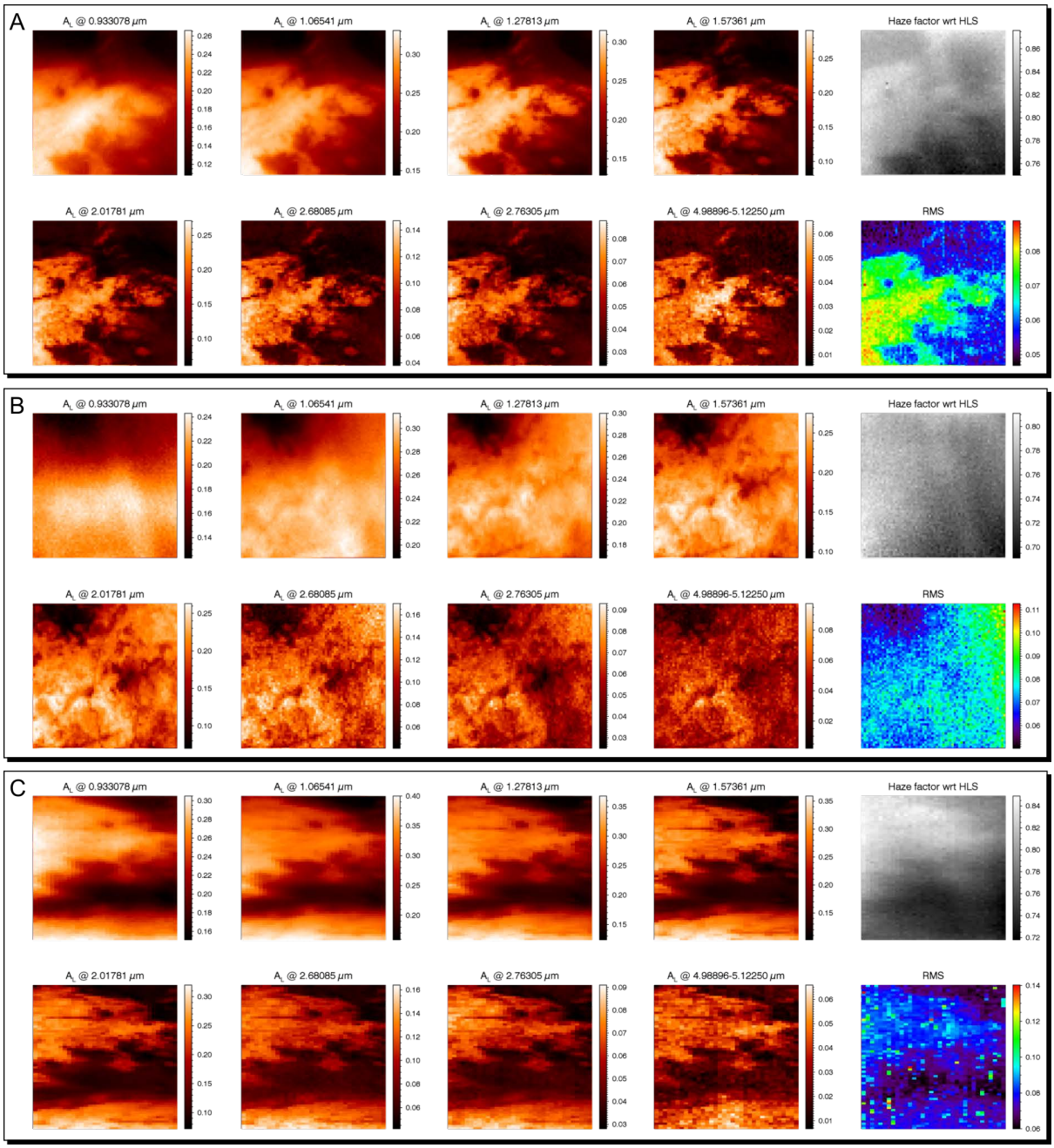

Figure B.3 – Lambert albedo maps produced after applying the radiative transfer model for VIMS data targeting eastern Xanadu through (A) CM_1514313117 and (B) CM_1514315913 (T9, December 2005), and (C) CM_1826082135 (T114, November 2015).

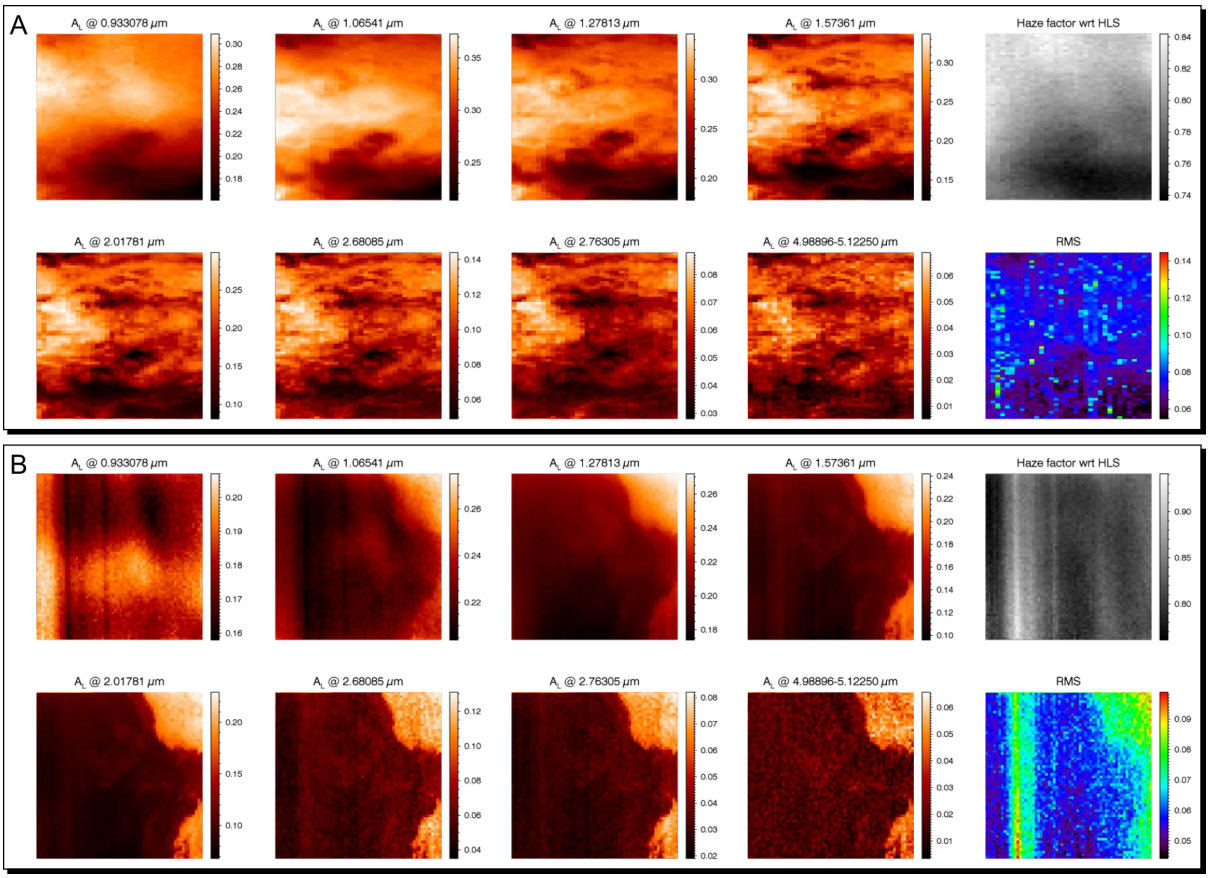

Figure B.4 – Lambert albedo maps produced after applying the radiative transfer model for VIMS data targeting Eastern Xanadu through (A) CM_1826085255 (T114, November 2015), and Chusuk Planitia through (B) CM_1802450543 (T20, October 2006).

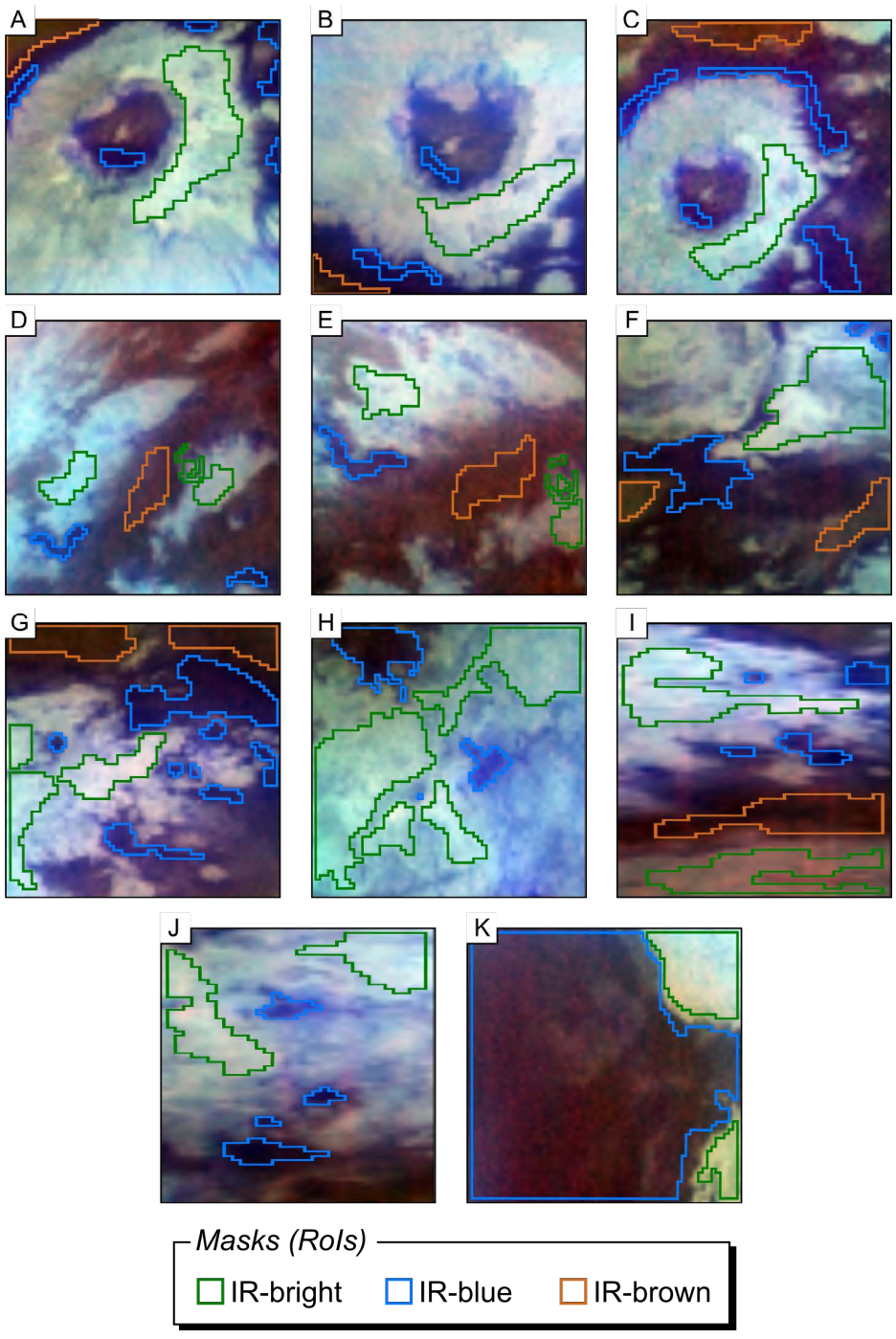

Figure B.5 – VIMS observations used to extract the single-scattering albedo (ω_0), after correction for atmospheric effects, in (A to C) Sinlap crater, (D to E) Aaru Regio, (F) Menrva crater, (G to J) eastern Xanadu and (K) Chusuk Planitia.

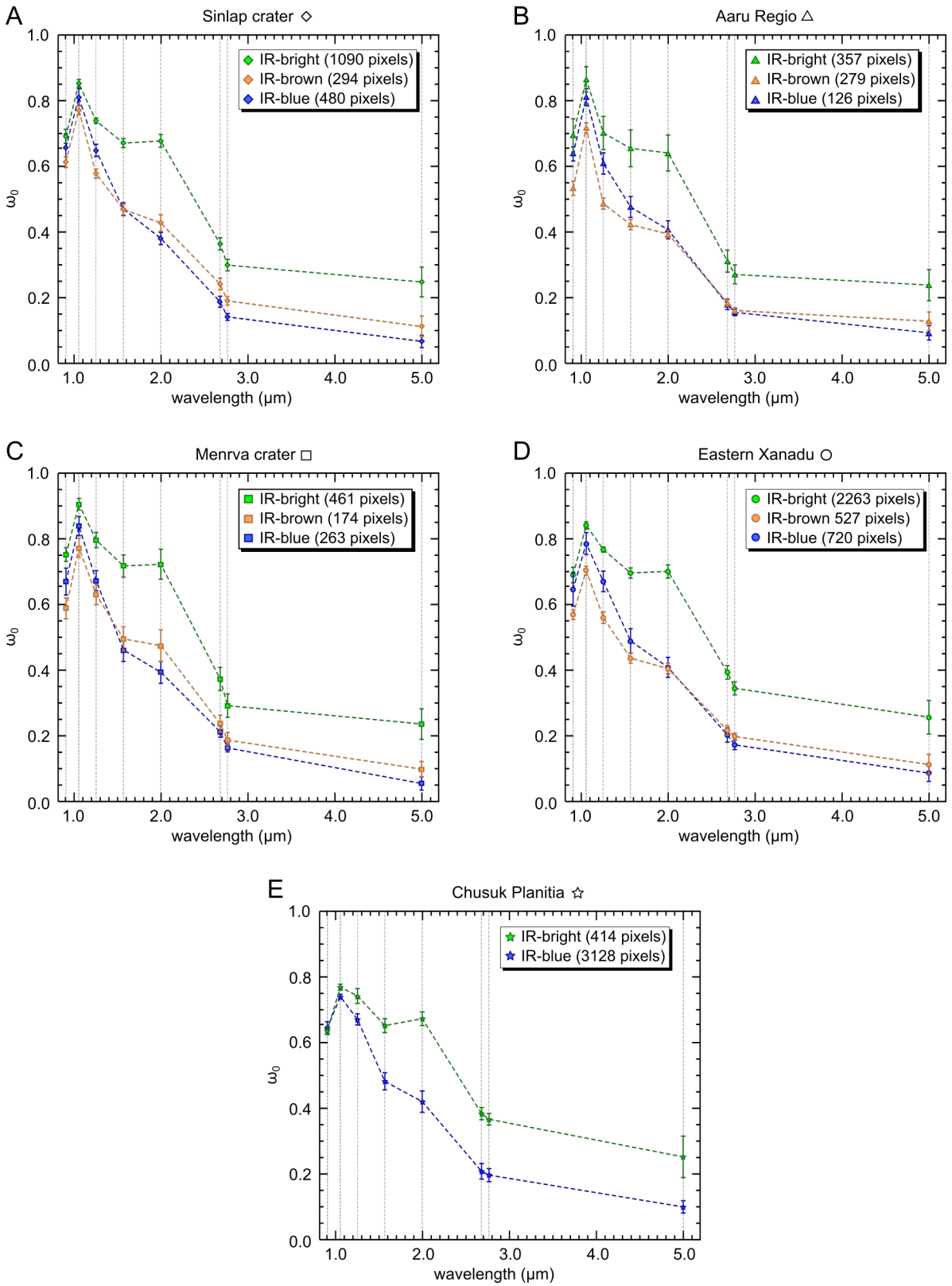

Figure B.6 – Spectra of the single-scattering albedo (ω_0) – for all infrared units present in the RoIs – derived from the radiative transfer model.

CURRICULUM VITAE AND PUBLICATION(S)

For reasons of data protection, the curriculum vitae is not published in the electronic version.

For reasons of data protection, the curriculum vitae is not published in the electronic version.

For reasons of data protection, the curriculum vitae is not published in the electronic version.